Title

Exploiting Electrochemistry in Water Treatment – from Membranes to Coagulation

Author

Khor, Chia Miang

Publication Date

2021

UNIVERSITY OF CALIFORNIA

Los Angeles

Exploiting Electrochemistry in Water Treatment – from Membranes to Coagulation

A dissertation submitted in partial satisfaction of the
requirements for the degree of Doctor of Philosophy
in Civil Engineering

by

Chia Miang Khor

2021

ABSTRACT OF THE DISSERTATION

Exploiting Electrochemistry in Water Treatment – from Membranes to Coagulation

by

Chia Miang Khor

Doctor of Philosophy in Civil Engineering

University of California, Los Angeles, 2021

Professor David Jassby, Chair

In water treatment processes, electrochemistry is a convenient and efficient means of water purification. It finds applications from the formation of coagulants to the fabrication of new membrane materials. Electrochemistry carries great potential for improved processes and applications. However, in view of its complexity compared to other available methods, it is an under-utilized approach.

In this dissertation, we first studied the important pre-treatment step - coagulation and flocculation. Model contaminated water based on wastewater produced by oil & gas refineries, as well as groundwater, were treated using both chemical and electrocoagulation. It was found that although chemical coagulation works well in low doses of an iron coagulant, electrocoagulation was eventually able to achieve higher removal rates than chemical coagulation could. The production of coagulants by means of oxidizing a sacrificial anode is a cheaper way of producing coagulants since the transport and storage of chemical coagulants includes the weight of counterions and hydrated components. In the second study about electrocoagulation, morphological and compositional changes of a sacrificial aluminium electrode was looked at using various modern characterization tools as electrocoagulation proceed. Surprisingly, although fouling occurred at the cathode, the most energy intensive step in electrocoagulation is the dissolution of aluminium owing to thickening of the aluminium oxide film.

The fabrication of new membrane materials was also explored using two electrochemical methods: electropolymerization and electrically-mediated atom transfer radical polymerization. Electropolymerization was successfully employed to form a dense salt-rejecting barrier using aromatic moieties similar to state-of-the-art polyamide membranes. Although its permselectivity is not as high as conventional polyamide RO membranes, electropolymerization offers an alternative fabrication technique that enables the use of environmentally benign solvents (ie. water) as the polymerization medium. Poly(acrylic acid) brushes grafted from an electrically conducting ultrafiltration membrane was shown to respond to the application of positive voltages by expanding and collapsing. Pore gating was achieved as a result, commanding the passage of 11 kDa particles on the flip of a switch. The response time was rather quick (within 10 minutes) and was attributed to the migration of hydrated counter ions as different voltages are applied to the membrane.

The Dissertation of Chia Miang Khor is approved.

Eric M. Hoek

Jennifer Ayla Jay

Sanjay K. Mohanty

David Jassby, Committee Chair

University of California, Los Angeles

2021

TABLE OF CONTENTS

CHAPTER 1: DISSERTATION INTRODUCTION 1

1.0 INTRODUCTION 1

1.1 COAGULATION AND FLOCCULATION 3

1.1.1 Impact of pH, coagulant dosage, stirring speed and ionic strength 5

1.1.2 Non-conventional coagulants 12

1.1.3 Electrocoagulation 13

1.2 MEMBRANE TECHNOLOGY 16

1.2.1 Membrane classification and transport mechanism 16

1.2.2 RO membrane 18

1.2.3 Mixed matrix membranes 19

1.2.4 Stimuli responsive membranes 20

1.3 RESEARCH OBJECTIVES 23

CHAPTER 2: PERFORMANCE, ENERGY AND COST OF OIL-WATER SEPARATION BY CHEMICAL COAGULATION AND ELECTRO-COAGULATION 25

2.1 ABSTRACT 25

2.2 INTRODUCTION 25

2.3 MATERIALS AND METHODS 29

2.3.1 Lab synthesized produced water 29

2.3.2 Chemical coagulation experiments 30

2.3.3 Electro-coagulation experiments 30

2.3.4 Analytical methods 31

2.3.5 Iron concentration calculation 31

2.3.6 Energy demand calculations 32

2.3.7 Operating cost calculations 34

2.4 RESULTS AND DISCUSSION 35

2.4.1 Electro-coagulation 35

2.4.2 Effectiveness of chemical coagulation and electro-coagulation 38

2.4.3 Energy consumption of chemical coagulation and electro-coagulation 40

2.4.4 Comparison of operating costs......42
2.5 CONCLUSIONS......44
CHAPTER 3: EXPLORATION OF 5052 ALUMINIUM ALLOY ELECTRODE DURING ELECTROCOAGULATION IN GROUNDWATER......46
3.1 ABSTRACT......46
3.2 INTRODUCTION......47
3.3 MATERIAL AND METHODS......50
3.3.1 Materials:......50
3.3.2 Methods:......50
3.4 RESULTS AND DISCUSSION......54
3.4.1 Electrocoagulation......54
3.4.2 Electrode characterization......58
3.4.3 Electrochemical characterization during EC......62
3.4.4 EIS at different current densities......67
3.5 CONCLUSION......72
3.6 APPENDIX......73
CHAPTER 4: ELECTROPOLYMERIZATION OF AROMATIC MONOMERS FOR SALT-REJECTING MEMBRANES......79
4.1 ABSTRACT......79
4.2 INTRODUCTION......79
4.3 MATERIALS AND METHODS......82
4.4 Materials......82
4.5 Methods......82
4.4 RESULTS AND DISCUSSION......86
4.4.1 Fabrication......86
4.4.2 Characterization......88
4.5 CONCLUSION......97
4.6 APPENDIX......98

CHAPTER 5: ELECTRICALLY MEDIATED MEMBRANE PORE GATING VIA GRAFTED POLYMER BRUSHES 99

- 5.1 ABSTRACT 99
- 5.2 INTRODUCTION 100
- 5.1 MATERIAL AND METHODS 102
  - *5.1.1 Materials........ 102*
  - *5.1.2 Methods........ 103*
- 5.3 RESULTS AND DISCUSSION 110
- 5.4 CONCLUSION 123
- 5.5 APPENDIX 123
  - *5.5.2 Experimental Results 124*

6.0 CONCLUSION 134

7.0 REFERENCES 136

LIST OF FIGURES

Figure 1: Coagulation / Flocculation treatment process 5

Figure 2: Concentrations of iron and aluminium hydroxides at different pH values at 25 °C ..6

Figure 3: Qualitative representation of changes in zeta potential of a colloidal suspension with changes in pH...7

Figure 4: Coagulation/flocculation zones as coagulant dosage is increased 9

Figure 5: Floc rupture mechanism...11

Figure 6: Graphical representation of electrocoagulation 15

Figure 7: Cut-off pore sizes of different membranes 17

Figure 8. (a) Freshly prepared simulated effluent before EC, (b) effluent after 20 min of EC at 32 mA/cm2. (c) pH changes with time during EC at different current densities. (d) COD removal and (e) O&G removal vs time during EC at different current densities. (f) Theoretical iron concentration as a function of time at different current densities. 36

Figure 9: Influence of iron concentration on effluent concentration and removal of CC and EC (a) Turbidity removal; (b) COD removal; (c) O&G removal. 40

Figure 10:. Influence of transportation distance on energy consumption of EC and CC with (a) turbidity removal; (b) COD removal; (c) O&G removal. (d) Influence of transportation distance on energy consumption of EC and CC at different distances at 90% removal coagulant dosage. 42

Figure 11: Influence of transportation distance on cost of EC and CC with (a) turbidity removal; (b) COD removal; (c) O&G removal. (d) Influence of transportation distance on cost of EC and CC at different distances at 90% removal coagulant dosage. 44

Figure 12: Flow through EC cell design used for the experiments in this study. 51

Figure 13: Hardness removal from synthetic groundwater at (a) 2mA/cm^2, (b) 10mA/cm^2 and (c) 25mA/cm^2. Si removal from synthetic groundwater at (d) 2mA/cm^2, (e) 10mA/cm^2 and (f)

25mA/cm^2. Turbidity changes in synthetic groundwater at (g) 2mA/cm^2, (h) 10mA/cm^2 and (i) 25mA/cm^2. 57

Figure 14: (a) Aluminium concentration in treated synthetic groundwater measured by ICP-OES plotted against charge loading for total dissolved aluminium, supernatant aluminium and theoretical aluminium concentrations. (b) Silicon and (c) hardness removal (%) from synthetic groundwater supernatant measured by ICP-OES plotted against charge loading. (d) treated synthetic groundwater pH changes overtime at a flowrate of 0.5 LPM. 58

Figure 15: XPS (a) anode and (b) cathode surface atomic composition normalized against Al atomic composition. Cross-sectional TEM images of (c) fresh aluminium electrode, (d) Al anode and (e) cathode after EC at 25 mA/cm^2 for 40 min. SEM surface characterization of (f) fresh aluminiuml electrode, (g) aluminium anode and (h) cathode after EC at 25 mA/cm^2 for 40 min. 61

Figure 16: Overpotential changes in the electrodes in (a) synthetic groundwater and (b) 3 mM Na_2SO_4. Tafel plots of the (c) anode-controlled and (d) cathode-controlled experiments in synthetic groundwater over time at 15 mA/cm^2. EIS of the (e) anode-controlled and (f) cathode-controlled experiments in synthetic groundwater over time at 15 mA/cm^2. 66

Figure 17: Nyquist plots of the Al (a) anode and (b) cathode at various current densities. (c) Nyquist plots of the Al anode at OCP using an RDE at different rotation speeds. (d) Equivalent circuit model used to fit the EIS experimental data at both high voltage and at OCP. (e) R1 values of the Al anode and cathode at various current densities. (f) Nyquist plots of the Al anode at 15 mA/cm^2 using an RDE at different rotation speeds. 71

Figure 18: Cyclic voltammetry of (a) resorcinol and (b) phloroglucinol with and without the addition of trimesic acid in the polymerizing solution. 86

Figure 19: FTIR of (a) SWCNT on PS35, electropolymerized (b) resorcinol, (c) TR, (d) TRT, (e) TRTMC, (f) phloroglucinol and (g) TP on SWCNT with PS35 as support. 88

Figure 20: Electropolymerized films of (A) phloroglucinol, (C) phloroglucinol and trimesic acid, (D) resorcinol, and (E) resorcinol and trimesic acid (F) TRT (G) TRTMC 92

Figure 21: (a) 2000 ppm NaCl rejection by the different electropolymerized membranes. (b) Change in flux of the different electropolymerized membranes over time as 17 bar is applied in a cross-flow module. 95

Figure 22: Electrochemical set-up for synthesis of PAA using the eATRP method 105

Figure 23: UF system design. Orange lines represent power and data connection, blue lines represent water flow. 108

Figure 24: Membrane module. Electrical potentials are applied onto the membrane through a wire connected to the inside of the membrane module, and a counter elecctrode fixed above the membrane. 108

Figure 25: Idealized shape of the rounded AFM tip viewed from the side 109

Figure 26: Membrane modification pathway. Step 1: pressure deposition of CNTs. Step 2: polymerization of DOPA. Step 3: CVD of CMPS. Step 4: eATRP of PAA from CNT modified membrane.. 111

Figure 27: (a) XPS spectra of the membrane at different fabrication stages. (b) C 1s high-resolution spectra of CMPS coated membrane. (c) C 1s high-resolution spectra of PAA-grafted membrane following eATRP. (d) Molecular weight evolution of PAA with time is linear with low dispersity. 113

Figure 28: Flux of PAA-grafted membrane at +2 V and 0 V in (a) 50 mM NaCl and (b) DI water. (c) Dextran rejection by PAA-grafted and non-grafted membranes at different applied potentials. 119

Figure 29: (a) AFM force curves at different applied potentials. (b) Advancing AFM force curves and (c) retracting AFM force curves taken at different time intervals over 129 minutes with curve (1) taken at 0 min, and curve (6) taken at 129 min. (d) Proposed mechanism for PAA brush movement as the AFM tip approaches the PAA-grafted membrane surface............ 122

LIST OF TABLES

Table 1: Particle size and classification 4

Table 2. Recipe for Model Produced Water 29

Table 3. Characteristics of Model Produced Water 30

Table 4. Energy Consumption of CC 33

Table 5. Energy Consumption for EC 33

Table 6. Operating Cost Factors 35

Table 7. Additional equations 35

Table 8. Discharge Limit and Target Removal for Offshore Effluent Disposal 39

Table 9: Synthetic Groundwater content 50

Table 10: XPS composition of carbon and oxygen of the different electropolymerized materials. 88

Table 11. Atomic % composition of different elements on the membrane surface after each modification step 113

Acknowledgements

I would like to thank my adviser, Dr. David Jassby, for his mentorship and extensive guidance. David has guided me to explore a wide range of research on electro-conducting membranes and other forms of electrochemistry. His support, optimism and patience have helped me overcome many frustrations in times of hardship and experimental failures. With his encouragement and support, I have grown me as an individual and a researcher. The life lessons I learnt from him will continue to have a lasting influence on my life.

Dr. Eric Hoek's guidance and support while at UCLA were instrumental in completing my degree. I would like to express my gratitude for his time and valuable advice. I deeply appreciate my committee members Dr. Jennifer Jay and Dr. Sanjay Mohanty for their time and help.

In addition, I would like to thank Dr. Xin Chen for providing the training and help. I would also like to acknowledge my friends and lab-mates, Dr. Yiming Su, Dr. Jingbo Wang, Dr. Xiaobo Zhu, Dr. Caroline Kim, Dr. Quynh Tran, Dr. Unnati Rao, Arpita Iddya, Bryan Jung, Shengcun Ma, Fan Yang and Yiming Liu without whose help and support this would have been impossible. Our research lab provides not only a good research platform but also a sense of family, warmth, and encouragement.

I appreciate the undergraduate students; Lew XuanYu and Sidney Poon at UCLA who helped me extensively with experimental work.

Vita

2014 Bachelor of Engineering in Material Science and Engineering
Nanyang Technological University
Singapore

Journal Publications

Khor, C. M.; Wang, J.; Li, M.; Oettel, B. A.; Kaner, R. B.; Jassby, D.; Hoek, E., Performance, Energy and Cost of Produced Water Treatment by Chemical and Electrochemical Coagulation. Water 2020, 12 (12), 3426.

Khor, C. M.; Zhu, X.; Messina, M. S.; Poon, S.; Lew, X. Y.; Maynard, H. D.; Jassby, D., Electrically Mediated Membrane Pore Gating via Grafted Polymer Brushes. ACS Materials Letters 2019, 1, 647-654.

Khor, C. M.; Ng, W. K.; Chan, K. P.; Dong, Y., Preparation and characterization of quercetin/dietary fiber nanoformulations. Carbohydrate Polymers 2017, 161, 109-117.

Khor, C. M.; Ng, W. K.; Kanaujia, P.; Chan, K. P.; Dong, Y., Hot-melt extrusion microencapsulation of quercetin for taste-masking. Journal of Microencapsulation 2017, 34, 29-37.

Ghavanloughajar, M.; Borthakur, A.; Valenca, R.; McAdam, M.; Khor, C. M.; Dittrich, T. M.; Stenstrom, M. K.; Mohanty, S. K., Iron amendments minimize the first-flush release of pathogens from stormwater biofilters. Environmental Pollution 2021, 281, 116989.

Iddya, A.; Hou, D.; Khor, C. M.; Ren, Z.; Tester, J.; Posmanik, R.; Gross, A.; Jassby, D., Efficient ammonia recovery from wastewater using electrically conducting gas stripping membranes. Environmental Science: Nano 2020, 7 (6), 1759-1771.

Rao, U.; Su, Y.; Khor, C. M.; Jung, B.; Ma, S.; Cwiertny, D. M.; Wong, B. M.; Jassby, D., Structural Dependence of Reductive Defluorination of Linear PFAS Compounds in a UV/Electrochemical System. Environmental Science & Technology 2020, 54 (17), 10668-10677.

Rao, U.; Iddya, A.; Jung, B.; Khor, C. M.; Hendren, Z.; Turchi, C.; Cath, T.; Hoek, E. M. V.; Ramon, G. Z.; Jassby, D., Mineral Scale Prevention on Electrically Conducting Membrane Distillation Membranes Using Induced Electrophoretic Mixing. Environmental Science & Technology 2020, 54, 3678-3690.

Su, Y.; Rao, U.; Khor, C. M.; Jensen, M. G.; Teesch, L. M.; Wong, B. M.; Cwiertny, D. M.; Jassby, D., Potential-Driven Electron Transfer Lowers the Dissociation Energy of the C–F Bond and Facilitates Reductive Defluorination of Perfluorooctane Sulfonate (PFOS). ACS Applied Materials & Interfaces 2019, 11, 33913-33922.

Zhu, X.; Dudchenko, A. V.; Khor, C. M.; He, X.; Ramon, G. Z.; Jassby, D., Field-Induced Redistribution of Surfactants at the Oil/Water Interface Reduces Membrane Fouling on Electrically Conducting Carbon Nanotube UF Membranes. Environmental Science & Technology 2018, 52, 11591-11600.

Conference Presentation

Conference: North American Membrane Society 28th Annual Meeting, Pittsburg, Pennsylvania, USA. Oral presenter for “Investigation of a smart electrically responsive ultrafiltration membrane”

Chapter 1: Dissertation introduction

1.0 Introduction

Water treatment has a long history that dates back to ancestral times when the motivation behind water treatment was for better tasting water that smells better. The earliest water treatment plant for domestic application was based on sand filtration and distributed by horses and carts. It was not until later that people discovered taste, smell and turbidity does not guarantee safe drinking water. Eventually, there was the discovery of multiple disinfection methods such as the addition of chlorine, hypo chlorite, ozone, and pre-treatment methods like coagulation and flocculation, active carbon adsorption. Waterborne illnesses such as cholera and E. coli has since become less prevalent. Today, there is a multitude of water treatment options available among which the most promising and widely used is based on membrane filtration. Just like sand filtration extensively used in the past, membrane filtration is built upon sieving out larger particles from contaminated water bodies, but much more efficiently and effectively.

With growing population every year, it is projected water demands will increase by 20% to 30% by 2050 [1]. Additionally steered by rising water pollution and economic growth, billions of people may face clean water scarcity. The main sources of water pollution come from human activities and include agricultural run-offs, oil spills, industrial waste dump and sewage leakages [2]. With the widespread use of manufactured chemicals for daily activities, there are persistent emerging contaminants such as perfluorootanoic acid (PFOA), perfluorooctant sulfonate (PFOS), pharmaceuticals and pesticides appearing in environment, some are known to accumulate in the human body and in wildlife [3]. As such, it is important to treat contaminated waters before discharge and to augment available water resources to meet future needs.

The potential uses of recycled water include crop irrigation, municipal, indoor toilet flushing, drinking and industrial water, with each type treated to a required level for their different purposes. Water reuse is especially important in parts of the world where there is dense population density or drought prone. Compared to seawater, wastewater from urban sources contain lower salt content making them more cost and energy efficient to recycle. Urban wastewater has been reused by applying a 3-step process comprising of ultrafiltration (UF) / microfiltration (MF), reverse osmosis (RO) and finally ultraviolet disinfection [4]. Although urban wastewater reuse may be a promising source, the purification process is costly and not always culturally accepted since it is actually sewage water and could be difficult to adopt.

The world's main fresh water bodies that provide for drinking water are groundwater (10.5 Mkm^3), wells, rivers and lakes (0.1 Mkm^3) [5]. According to the National Groundwater Association (NGWA), groundwater accounts for 29% of the freshwater supply in USA [6]. Of which, 70% goes to irrigation. 41% of the USA population regularly depends on groundwater for their drinking needs. With changing weather patterns and droughts occurring in many parts of the world, some areas have turned to seawater desalination for a reliable and constant supply of freshwater. The global number of desalination plants have grown steadily since the first large-scale plant was built in the 1960s. Now more than 300 million people depend on desalination plants to meet their water demands [7].

The steps in producing drinking water from groundwater in USA involve the following: 1) coagulation and flocculation, 2) sedimentation, 3) sand, gravel and charcoal filtration, and 4) disinfection using disinfectants such as chlorine and chloramine [8]. In drinking water production from seawater, there are 2 filtration steps. The first removes larger suspended solids using MF/UF, and the second removes ions and other impurities using an RO membrane. The final step reintroduces removed minerals for better taste and to prevent pipe corrosion [9].

1.1 Coagulation and Flocculation

Coagulation is the process of changing from a liquid to a solid state. In water bodies, some examples of particles in water include clay, silica and oil. These particles carry like charges and are stable in suspension since like charges repel. Coagulation by the addition of chemicals such as alum and ferric chloride destabilizes electrostatic charges present on suspended particles. Once electrostatic charges are destabilized, the particles are able to flocculate and clump into larger clusters known as floc that settles at a faster rate. There are four mechanisms that lead to particle aggregation removal: 1) double layer compression, where particles overcome repulsive forces and agglomerate; 2) precipitate enmeshment, where small particles are physically trapped by metal precipitates as they form and settle [10]; 3) charge neutralization, where electrostatic repulsive forces are neutralized to cause destabilization; and 4) interparticle bridging, where polyelectrolytes promote aggregation of microflocs [11].

Particles of various sizes require different amounts of time to settle. They can be classified according to their different sizes is shown in Table 1 [12]:

Table 1: Particle size and classification

Particle Size (mm)	Classification	Time required to settle 10 cm if specific gravity is 2.65
10	**Coarse dispersion (visible to the naked eye)**	**0.1 s**
1		**1 s**
10^{-1}		**13 s**
10^{-2}	**Fine particulate dispersion (visible under microscope)**	**11 min**
10^{-3}		**20 h**
10^{-4}		**80 days**
10^{-5}	**Colloidal dispersion**	**2 years**
10^{-6}		**20 years**
$\leq 10^{-7}$	**Solution**	**∞**

Examples of coarse dispersions include gravel, sand, macroplankton and flocculated particles. These particles settle within seconds and are generally easy to remove either by coagulation and flocculation, or sand filtration before proceeding further in the water treatment process. Particles within the range $10^{-2} - 10^{-5}$ mm can removed by membranes [12]. Smaller particles require more extensive removal methods and can quickly become expensive. To achieve expected water quality targets, coagulation is a necessary pre-treatment step in water purification. It has been reported coagulation of a model water before UF impacted the permeate quality positively by effectively removing dissolved organic matter in the size range of <1 nm to 0.45 µm [13, 14]. In the same study, membrane fouling was also reduced. Coagulation as a pre-treatment step has been used in diverse applications, such as in landfill leachates [15], pharmaceutical industrial wastewater [16], hospital wastewater [17] and high-strength saline wastewaters [18].

The coagulation and flocculation treatment process normally starts with the addition of a coagulant, followed by fast mixing for ensure complete dispersion and coagulation, subsequent slow mixing for a longer period of time to enable floc formation. The slow mixing would enhance orthokinetic collisions of particles that promotes floc growth. Finally, mixing is stopped for sedimentation or filtration [19-21]. A graphical representation of the treatment process is shown in Figure 1.

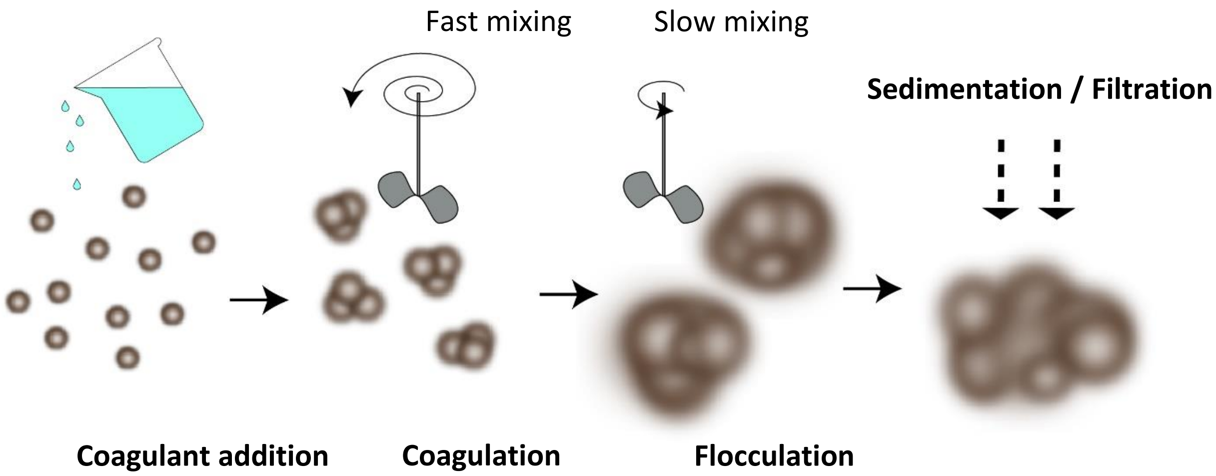

Figure 1: Coagulation / Flocculation treatment process

1.1.1 Impact of pH, coagulant dosage, stirring speed and ionic strength

Practically all colloidal particles are overall negatively charged and hence are stable in water. Electrostatic repulsion drives particles apart, while van der Waals forces bring the particles together [22]. According to the DLVO theory, destabilization of these suspended particles is possible through either the addition of large amounts of salt, or through the addition of cations for charge neutralization. Traditionally, hydrolysed iron or aluminium salts have been used as coagulants for water treatment. Factors such as pH, ionic strength and coagulant dosage play a role in the effectiveness of particle removal.

1.1.1.1 pH

When iron or aluminium cations are dissolved in water, they are quickly hydrolysed and form an octahedral coordination with 6 water molecules in the case of mononuclear hydrolysis products [23]. Depending on pH, metals ions can be continually hydrolysed. Protons on the metal cation is progressively replaced by hydroxyl ions as the pH is increased, leading to lower positive charges according to the following sequence [24]:

$$Al^{3+} \rightarrow Al(OH)^{2+} \rightarrow Al(OH)_2^{+} \rightarrow Al(OH)_3 \rightarrow Al(OH)_4^{-}$$

Figure 2 shows the solubility of the different metal hydroxide species at different pH values [24]. At around neutral pH, these salts have the lowest solubility, allowing the largest amount of them to precipitate into amorphous hydroxides, also known as floc.

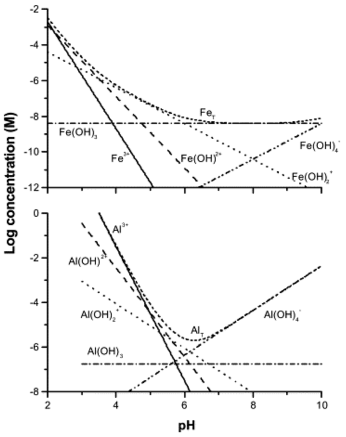

Figure 2: Concentrations of iron and aluminium hydroxides at different pH values at 25 ^{o}C

Other than changes in speciation and solubility of the hydrolysed metal coagulant, charges on a particle surface could change with solution pH. Typically, zeta potential is used as a measurement for the effective 'charge' on a particle surface since it is difficult to measure charges on a particle surface because of charge concentrations in the Stern and diffuse layers [25]. Consequently, the zeta potential tells us particle stability in a suspension [26]. Zeta potential can be a strong function of pH. Figure 3 shows a qualitative representation of the changes in zeta potential of a particle dispersion with changes in pH [27]. At the isoelectric point (where zeta potential = 0), the particle surfaces are uncharged. This is the point where the particle suspension is the most unstable due to lack of electrostatic repulsion between the particles. Above zeta potential = |30|, the particle suspension is considered stable.

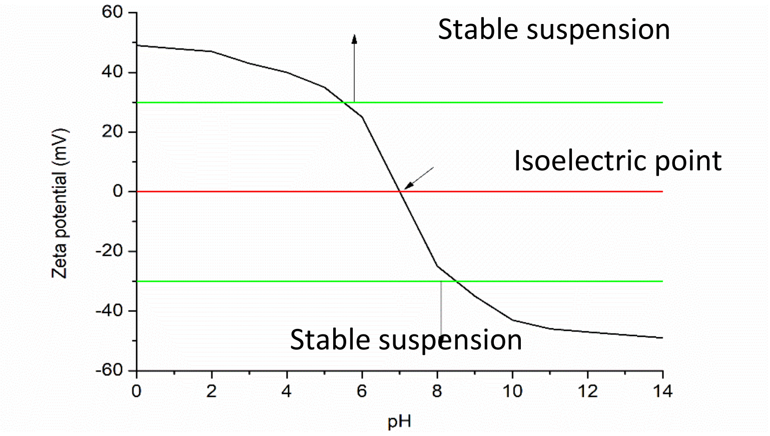

Figure 3: Qualitative representation of changes in zeta potential of a colloidal suspension with changes in pH

1.1.1.2 Coagulant dosage

Insufficient coagulant dosing or over-dosing would result in poor coagulation/flocculation performance [28]. As coagulant dosage is increased from insufficient to an overdose, particles go through 4 stages, namely stabilization, charge neutralization, restabilization and sweep coagulation [29, 30]. Figure 4 illustrates the zones particles go through as coagulant dosage is increased.

Zone 1: Stabilization

In stabilization zone, there is insufficient coagulant and so particles are still negatively charged and stable in suspension. Also, at low concentrations of coagulant dosage, only soluble species are present.

Zone 2: Charge neutralization

In the charge neutralization zone, there is enough coagulant dosed so that particle charges are neutralized and able to coagulate. There is a stoichiometric relationship between the particle surface charges and the most favourable coagulant dosage [31]. When there are low concentrations of particle, low coagulant dosages should be required. However, with low coagulant doses, coagulation rates can be very low, creating difficulties in water treatment. Another problem with trying to get the optimum coagulant dosage is that the range can be quite small. A very precise dosing control is necessary [30]. With the use of high coagulant dosage, these difficulties can be overcome since at high coagulant concentrations hydroxide precipitation occurs, providing sweep flocculation.

Zone 3: Restabilization

In restabilization zone, there is an excessive amount of coagulant, causing the particles to be stable in suspension again due to ion shielding effect or positive charges on the particles.

Zone 4: Sweep flocculation

In sweep flocculation zone, a large amount of metal hydroxide forms due to low solubility. Particles are enmeshed in the growing hydroxide precipitate, effectively removing them from the suspension. A difference between particle removal in charge neutralization and sweep flocculation zone is that flocs are formed more quickly and can become bigger in the case of sweep flocculation [32].

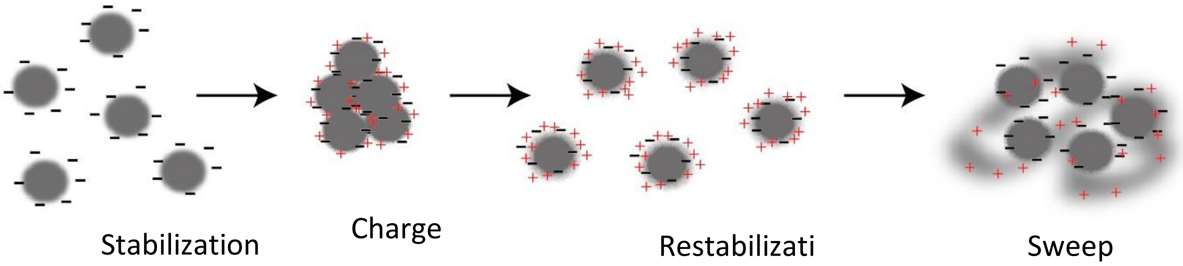

Figure 4*: Coagulation/flocculation zones as coagulant dosage is increased*

1.1.1.3 Ionic strength

An increase in ionic strength reduces zeta potential of charged particles through a charge shielding effect. Thickness of the diffuse part of the particle double layer is also decreased. However, ionic strength increases could also shield charges present on the coagulant and reduce their effect in particle removal.

It was shown in a study, with an increase in ionic strength from 0.05 mol/L to 0.25 mol/L, the removal efficiency of humic acid from a solution containing hardness and natural organic matter dropped from 92% to 88% [33]. This was attributed to a decrease in the activities of aluminium hydrolysis products. Li et al. added sodium ions (up to 0.1 mol/L) to a dye contaminated solution after flocs were formed, resulting in the formation of larger flocs due to weakened electrostatic repulsion within the floc [34]. However, when the ionic strength was further increased, loose flocs were formed.

1.1.1.4 Floc breakage and stirring speed

The size, density and structure of flocs are very important as they affect separation efficiency after coagulation. Floc breakage is common around the impeller zone during mixing, transfer of solution from one tank to another, or where stresses are exerted on the formed flocs. If flocs are broken into smaller sizes, their settling time change accordingly like those shown in Table 1. The eventual floc size is a dynamic balance between floc growth and floc-breakage. It was shown the steady-state floc size was dependant on stirring rate during flocculation [35].

There are two ways in which floc can rupture when stresses exerted on the floc is larger than the floc bonding strength: 1) surface erosion, where small particles are removed from the surface or formed flocs; and 2) large-scale fragmentation, where flocs break into pieces of comparable sizes without causing an increase in particle concentration [36]. It is generally thought that surface erosion is caused by shear stresses exerted on the surface of the floc, while large-scale fragmentation is induced by tensile stress in opposite directions. A graphical presentation is shown in Figure 5:

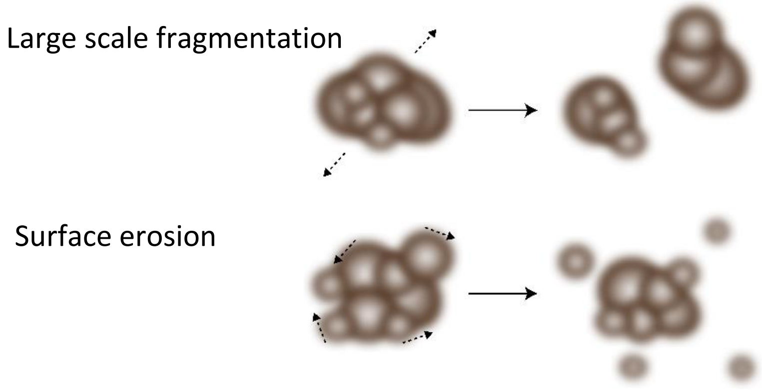

Figure 5: Floc rupture mechanism

PACl, alum and 2 cationic polyelectrolyte (poly(diallyldimethylammonium) chloride (PolyDADMAC) and Zetag 64 (a copolymer of acrylamide)) has been studied for its floc breakage and regrowth after breakage [37]. After formation, the formed flocs were broken at high stirring speeds and allowed to regrow. For PACl and alum, there was only limited regrowth suggesting irreversibility of the broken floc. For the 2 cationic polyelectrolytes on the other hand, broken flocs regrowth was almost fully reversible. In a separate study, the further addition of monomeric PACl after floc breakage enabled regrowth to sizes larger than before, while polymeric PACl did not significantly help with floc regrowth [38]. It was speculated that freshly formed hydroxide (formed by monomeric PACl) was able to coat the broken floc surface and help with regrowth. Precipitates formed from polymeric PACl was very different from amorphous hydroxides generally formed from the precipitation of aluminium salts.

1.1.2 Non-conventional coagulants

1.1.2.1 Pre-hydrolysed

It is broadly thought that the hydrolysed species of the metal cation adsorbs more strongly on negatively charged particles than the free hydrated form [39]. Pre-hydrolysed forms of metal coagulants are now commercially available, commonly in the form of polynuclear species. Being pre-hydrolysed, these forms of metal coagulant have less impact on the solution pH which minimizes the need for extra pH adjustments [40, 41].

Some examples are polyaluminium chloride (PACl) and polyferric sulphate (PFS) [29, 42]. PACl was reported to be an effective coagulant at a wider range of pH when compared to the traditional coagulant, alum [29]. In another study, PACl was purified to sieve out PACl with polynuclear Al_{13} (PAC-13). Compared to $AlCl_3$, PAC-13 achieved higher turbidity, humic acid and colour removal [42]. In an arsenic removal study, ferric (III) sulphate was compared with PFS [43]. They were found to have similar removal efficiencies, but a lower dose of PFS was required compared to ferric (III) sulphate.

1.1.2.2 Biopolymer

Biopolymers are a class of polymers that occur naturally and can be positively or negatively charged. Compared to chemical coagulants, biopolymers are able to biodegrade floc that cause less harm to the environment. Biopolymers such as tannin, starch and chitosan has been studied for their efficiency as a coagulant. Tannin was shown to be effective for the removal of total phosphorus, turbidity, at 72% and 80% respectively in agricultural wastewater [44]. In another study, sago starch was modified with polyacrylamide and found to achieve 96.9% turbidity removal of a kaolin suspension [45]. Moringa oleifera seeds have also been studied for its effectiveness as a coagulant for Mumbai wastewater [46]. It was shown to remove 50% COD on its own, and up to 64% COD when used in conjunction with alum.

1.1.2.3 Coagulant aids

Coagulant aids act to improve the settling characteristics of floc produced by coagulants. Synthetic polyelectrolytes are frequently used as coagulant aid due to its effectiveness [47]. Other coagulant aids include activated silica, sodium alginates and other soluble starch [48]. They are known to be able to flocculate microflocs thereby reducing settling times and improve water quality.

PolyDADMAC used as a coagulant aid with PACl, aluminium sulphate, and a composite of aluminium sulphate and ferric chloride to remove and kill algae in settled sludge [49]. Algae removal rates reached as high as 90.6% for PACl/PolyDADMAC, and algicidal rates reached as high as 19.1% for aluminium sulphate/PolyDADMAC.

UF membrane fouling was investigated with and without the addition of polyacrylamide as a coagulant aid with alum before passing through the membrane [50]. It was found that an appropriate polyacrylamide dosage was necessary, with lower dosages reducing membrane fouling, and a high dosage increasing membrane fouling.

1.1.3 Electrocoagulation

Electrocoagulation (EC) is an alternative process to chemical coagulation where instead of dosing chemical coagulants, sacrificial aluminium or iron electrodes are dissolved /

corroded into untreated water through electrochemical oxidation to produce the coagulating species. While water splitting at the cathode produces hydroxide ions, aluminium dissolved at the anode combines with hydroxides to form metal hydroxides as the coagulating species.

Using aluminium as a model, formation of the coagulating species ($Al(OH)_3$) can be described by the following reactions [51-53]:

At the anode:

$$Al \rightarrow Al^{3+} + 3e^- \tag{1}$$

$$2H_2O \rightarrow 4H^+ + O_2 + 4e^- \tag{2}$$

At the cathode:

$$2H_2O + 2e^- \rightarrow H_2 + 2\,OH^- \tag{3}$$

In the bulk solution:

$$Al^{3+} + 3H_2O \rightarrow Al(OH)_3 + 3H^+ \tag{4}$$

The formation of poly-hydroxides such as $Al(H_2O)^{3+}$ and $Al_6(OH)_{15}^{3+}$ are also possible [54-56]. The dynamic process of hydroxide formation and combination of hydroxides with metal ions help to maintain a stable pH during electrocoagulation. Evolution of H_2 gasses during EC promotes floating floc formation.

Figure 6 presents a graphical representation of an EC process.

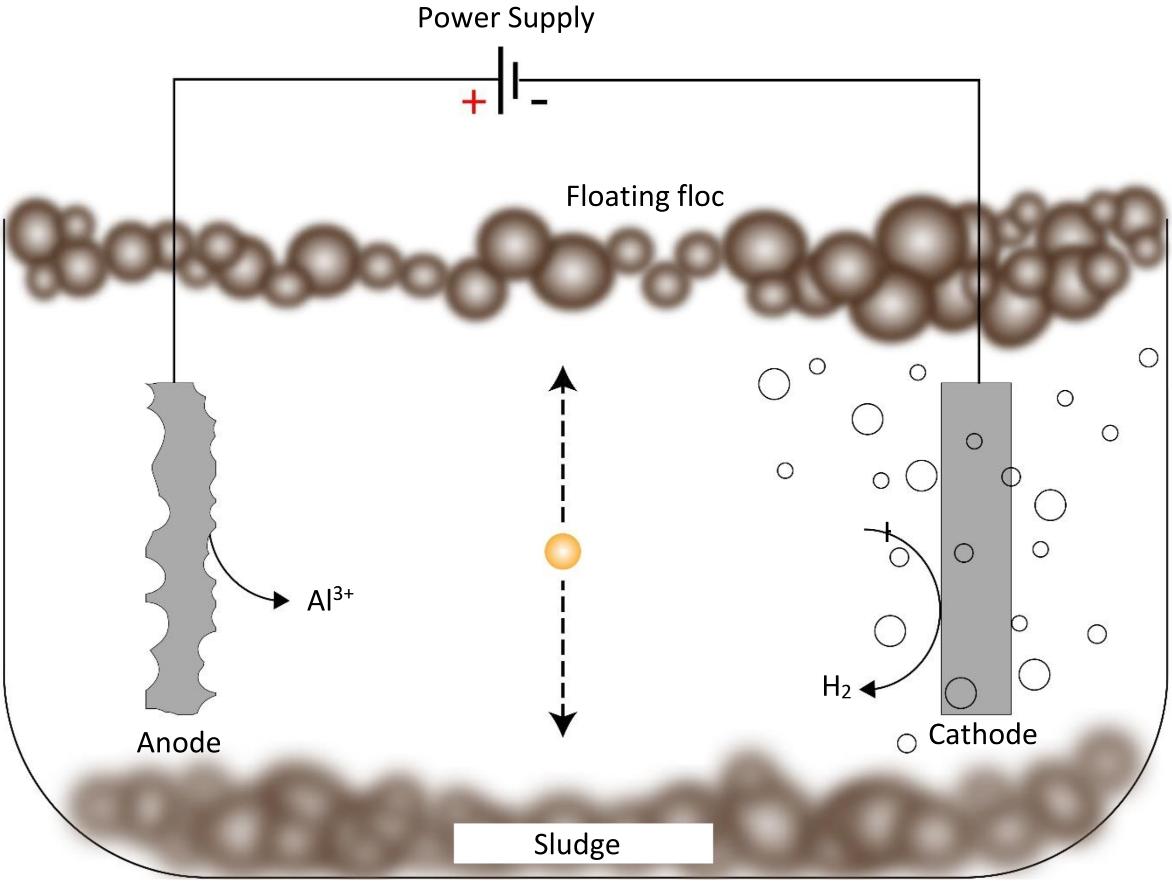

Figure 6: Graphical representation of electrocoagulation

Dissolution of the metal anode during EC is crucial for success in removing particles. Passivation of the electrodes (especially aluminium) as well as high solution resistance may result in excessive energy requirements [57-59]. The presence of pitting promoters is also important to allow de-passivation of aluminium. Noorzalila et al. reported an improvement in electrocoagulation performance in landfill leachate using of Al 5052 vibration-induced plates due to improved ionic transfer and bubble detachment in a batch process [60]. Martin et al. compared passivation of pure aluminium and Al 1050 with a rough or smooth surface in neutral electrolyte solutions [61]. In the findings, a rough surface having “spontaneous de-passivation” even without the addition of pitting promoters such as chloride ions.

Flocs formed by chemical coagulation (CC) has been compared with that of EC [62]. It was found that EC produced loose flocs because the repulsive barrier between particles is low, while CC produced more compact and stronger floc due to a high repulsive barrier between the particles.

1.2 Membrane Technology

Membranes are semi-permeable physical barriers that have the ability to separate large or charged species from smaller or neutral particles and molecules by creating a barrier for the former. For the case of water treatment, there are a number of ways in which clean water can be produced from membrane purification processes.

1.2.1 Membrane classification and transport mechanism

Electrodialysis (ED) separates ionic species from an aqueous solution by moving ions through membranes, under an applied electric potential. Forward osmosis (FO) relies on the natural osmotic pressure between 2 water bodies to pull polluted water from one side of the membrane to the other side of high concentration. Membrane distillation (MD) and pervaporation (PV) are two methods that uses the process of evaporation and condensation to separate clean water from the permeate. Reverse osmosis (RO), nanofiltration (NF), ultrafiltration (UF) and microfiltration (MF) are pressure-driven processes that have a range of pore sizes for different separation requirements. Figure 7 shows the cut-off pore sizes for the different membranes and their separation capabilities differentiated by the sizes of the different contaminants [63].

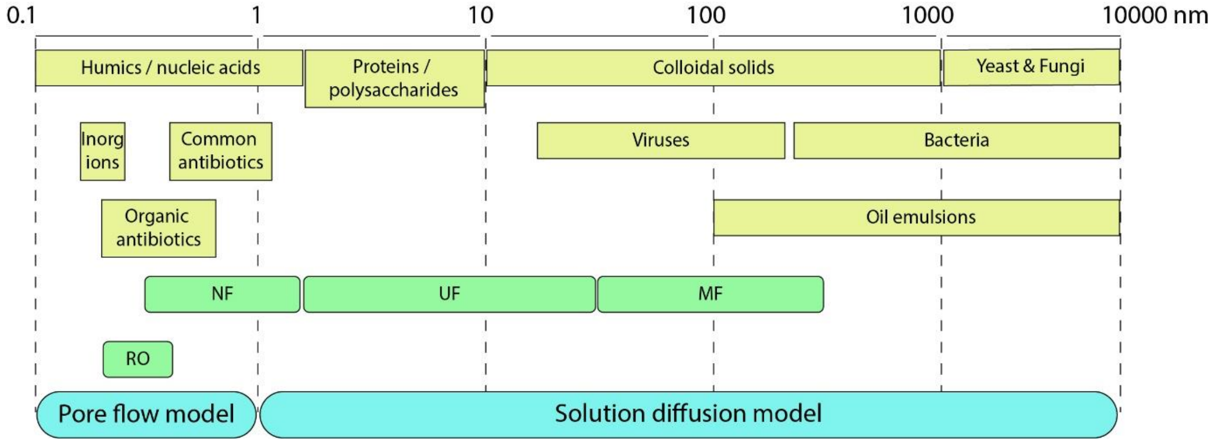

Figure 7: Cut-off pore sizes of different membranes

MF have pore sizes ranging from 50 – 500 nm and are suitable for separating contaminants like yeast and fungi, bacteria, and oil emulsions. UF have smaller pore sizes ranging from 2-50 nm making them applicable to isolating colloidal solids, viruses, proteins and humic acids on top of what MF could separate. Often, UF and MF are used as pre-treatment methods for contaminated waters before passing on to NF and RO. NF have pore sizes less than 2 nm and are capable of separating antibiotics and multivalent ions. RO do not have pores, and are effective at removing monovalent ions.

Because MF and UF have larger pore sizes, transport of molecules across the membranes are best described by the pore flow model where contaminants are separated by pressure-driven convective flow through tiny pores [64]. Unlike MF and UF, RO and NF have a non-porous dense structure. Molecule transport through the membrane can be described by the solution diffusion model where molecules adsorb onto the voids (free-volume elements) of nonporous membranes and then diffuse through the membrane down a concentration gradient. Separation is achieved due to a difference in dissolution and diffusion rate of the different molecules through the RO and NF membranes. Transport of permeate in the pore flow model can be described by a modified Darcy's law shown in equation 5 [65], and the solution diffusion model is described by Fick's law shown in equation 6 [64].

$$J_i = \frac{dP}{\mu \times R_m} \tag{5}$$

$$J_i = -D_i \frac{dc_i}{dx} \tag{6}$$

Where J_i is the membrane permeate flux of species i, dP is the transmembrane pressure, μ is the absolute viscosity Rm is the hydraulic resistance of the membrane to water permeation. It incorporates resistances attributed to the intrinsic property of the membrane as well as fouling. D_i is the diffusion coefficient of species i through the nonporous membrane, and $\frac{dc_i}{dx}$ is the concentration gradient.

Generally, when constructing membranes, researchers must take into consideration a trade-off between membrane permeability and selectivity. A membrane with a smaller pore size would achieve higher selectivity but however with diminished permeability. Thus, to achieve the desired goals, it is crucial to select a membrane with the applicable pore sizes.

1.2.2 RO membrane

The two most common configurations for RO membranes are flat sheet thin film composite (TFC) membrane in spiral wound configuration, and cellulose acetate hollow fibre membranes [66]. In the flat sheet TFC configuration, membranes are made of 3 layers: a non-woven fabric for mechanical strength, followed by a microporous support layer, and finally the polyamide active layer where separation takes place.

It was discovered RO membranes produced from monomeric aromatic amines and aromatic acyl halides that contain at least 3 halide groups produced membranes with exceptional permselectivity [67, 68]. Polyamide is currently the most utilized RO material owing to its high water permeability and high salt rejection [69].

The use of polysulfone as a microporous support layer has enabled interfacial polymerization (IP) to prepare RO membranes since it can resist alkaline conditions created by the use of an alkaline catalyst / acid acceptor in condensation reactions. This paved the way for a highly crosslinked and ultrathin polyamide skin structure. The IP process starts with saturation of the microporous support layer with an aqueous solution of m-phenylenediamine (MPD). Acid acceptors such as triethylamine are sometimes added to the aqueous solution [70, 71]. Next, trimesoyl chloride (TMC) in an organic solution is added to saturated membrane to form the polyamide layer.

1.2.3 Mixed matrix membranes

Although possessing excellent permselectivity, polyamide RO membranes have their shortcomings. Due to their low resistance towards oxidizing agents such as chlorine, often the permeate cannot contain high concentrations of disinfecting agents. This causes the RO membrane to be vulnerable to the growth of biofoulants that will eventually lead to lowered salt rejection and high transmembrane pressure.

Ceramic membranes are another class of materials mechanically supported by materials such as alumina, silica and zirconia. They have been fabricated for use as MF and UF membranes for use in industrial settings [72]. Owing to their mechanical strength as well as thermal and chemical stability, these membranes are well-suited for challenging water purification processes. Flux after fouling is also easily restored since they can be cleaned by harsh chemicals and even thermal cleaning processes. Despite the convenience of ceramic membranes over polyamide membranes, their cost, difficulties in handling and preparation, and relative thickness have hindered their use in commercial settings.

Mixed matrix membranes (MMM), also known as hybrid membranes, blends the superiority of the polymeric matrix and inorganic fillers to create high-performance materials. Karimi et al. embedded zeolitic nanoparticles into polyvinylidene fluoride (PVDF) using the phase inversion technique to create membranes with high water flux and increased anti-fouling performance in BSA solution [73]. In another study by Maryam et al., graphene oxide-silica nanoparticles were embedded in polyethersulfone (PES) through the phase inversion technique to create a MMM for oil refinery wastewater treatment. The membrane exhibited higher water flux and at the same time higher oil removal efficiency than the original PES membrane [74]. Nonetheless, the development of MMM is still immature and face a number of problems, such as complexity in fabrication, high cost and phase segregation [75].

1.2.4 Stimuli responsive membranes

Stimuli responsive membranes are membranes that change their physicochemical properties when changes are made in their environment. These membranes respond in controlled and predictable ways when external stimuli such as pH, ionic strength, electric fields, and temperature are changed. Reversible changes occur fast and locally in these membranes, allowing novel applications.

The responsiveness of stimuli responsive membranes is generally brought about by changes in the polymer chain conformations. All polymers are sensitive to changes in their immediate environments and their responsiveness could be based on adjustments in surface energy, entropy, or segmental interactions. Primarily the interfacial energy between the polymer chains and their immediate environment are minimized.

Some intrinsic properties of polymers that enable them to respond to different environmental triggers are based on their solubility, extent of dissociation, charge screening effect, and incorporation of hydrated counter ions in a given condition. Surface confinement of polymer chains tend to impart more responsiveness to the material. The extent of their responsiveness could be greatly affected by their grafting density.

Grafting of poly(N-isopropylacrylamide) (PNIPAAm) brushes onto poly(ethylene terephthalate) (PET) track-etched membranes allowed the formation of a membrane that can act like a thermal valve. The extension and collapse of PNIPAAm brushes was controlled by lowering and increasing the feed temperature around its lower critical solution temperature [76]. At temperatures below the lower critical solution temperature (LCST) of PNIPAAm, water is a good solvent, thus causing expansion. When the temperature is increased to above the LCST, water becomes a poor solvent, and PNIPAAm collapses.

pH responsive poly(methacrylic) acid brushes grafted from polycarbonate membranes have also been shown to act as a gate, allowing and stopping flow through the membrane with pH changes [77]. As a weakly acidic polyelectrolyte, poly(methacrylic) acid brushes respond by expanding upon an increase in pH and collapsing vice versa. These conformational changes are in response to the degree of dissociation of its ionizable groups.

As for strong polyelectrolytes that generally already have a high degree of dissociation, they do not respond strongly to pH stimuli. However, at high salt concentration, electrostatic screening of the ionized group on the polymer chain leads to conformational changes. Zwitterionic polysulfobetaine methacrylate (PSBMA) hydrogel was shown to increase in swelling ratio as ionic strength was increased [78]. This behaviour was attributed to weakened self-association among the zwitterionic moieties resulting in chain extension.

In another study, electrically responsive nanoporous membranes based on polypyrrole doped with dodecylbenzenesulfonate anion (PPy/DBS) was electropolymerized on an anodized aluminium oxide membrane. Large volume changes depending on the applied potential allowed for a pulsatile drug release of a model drug [79]. The expansion and collapse of its polymer brushes was attributed to the incorporation of large hydrated positive counterions to achieve electrical neutrality when the polymer was changed from an oxidized state to a reduced state.

Grafting density is another factor that could affect the conformational responsiveness of polymer chains. Both high and low grafting densities could result in diminished response to external stimuli. At low grafting densities, interaction between the grafted polymer chains and the support is limited. Thus, the polymer chain responses to external stimuli are equivalent to that of the free polymer in solution. At high grafting densities on the other hand, response to external stimuli is weakened since the polymers are already highly stretched in a crowded layer. It is only at moderate grafting densities that polymers respond well to external stimuli.

1.3 Research Objectives

The overall research objective of this dissertation is to utilize electrochemistry to tap the unexplored potentials of water treatment. Chapters 2 and 3 discusses an important water pre-treatment method that has been around since 1500 BC – coagulation. In chapters 4 and 5, electrochemistry is used to fabricate new membrane materials in an attempt to uncover the hidden possibilities of non-conventional membrane materials.

Chapter 2 compares the separation performance, energy demands and operating costs of chemical coagulation (CC) versus electrical coagulation (EC) in and oil & gas produced water matrix using iron based coagulants. The overall cost of EC was found to be around half that of CC, and at the same time, EC was more effective at oil and gas removal.

Chapter 3 explores the compositional and morphological changes of a sacrificial aluminium anode during EC at different current densities in a model groundwater. The reactor cell was equivalent to a plug-flow reactor that had short retention time of up to of up to 2.1 s. The treated water achieved silicate removal of up to 50 ± 4%, and hardness removal of 11 ± 1 %. It was found that the most energy intensive step in EC is aluminium dissolution at the anode, which is worsened by a thickening of an aluminium oxide film at the anode. It was further demonstrated by EIS that under these conditions the charge transfer resistance was constant throughout the duration of the experiment.

Chapter 4 discusses alternative RO materials fabricated from the electropolymerization of aromatic moieties similar to the structure of state-of-the-art polyamide RO membranes. Although salt rejection and water flux are unable to challenge conventional seawater RO membranes, the highest NaCl salt rejection achievable by the electropolymerized membranes was as high as 83 %. This demonstrates the capability of this fabrication method in producing RO membranes.

Chapter 5 presents a stimuli-responsive membrane grafted from poly(acrylic acid) monomers on top of a percolating network of carbon nanotubes coating an ultrafiltration membrane. The use of surface initiated electrochemically-mediated atom transfer radical polymerization (SI-eATRP) enabled the growth of polymer brushes with molecular weights as high as 930 kDa, and very low dispersivity. Membrane rejection and flux were readily changed upon the application of electrical potentials, with positive potentials increasing flux by 85% and reducing rejection of a 12 kDa dextran by 56%, while negative potentials reduced flux by 30% and increased rejection by 5%. We show evidence that counter-ion migration, moving in response to the applied electric field, is responsible for the expansion or collapse of the grafted charged polymer brushes, which induced or eliminated pore gating. The materials can find applications in industrial separations where gating is needed and may possess interesting anti-fouling properties.

Chapter 2: Performance, Energy and Cost of Oil-Water Separation by Chemical Coagulation and Electro-Coagulation

2.1 Abstract

The separation performance, energy demand, and operating costs of electro-coagulation (EC) were compared to conventional chemical coagulation for oil-water separation using a simulated oil & gas produced water matrix. An iron based chemical coagulant and sacrificial iron electrodes were compared. Effluent turbidity, chemical oxygen demand (COD), total organic carbon (TOC), and oil and grease (O&G) removals were determined for various coagulant concentrations and reaction times and current densities. Chemical coagulation produced superior turbidity removal when scaled by the total iron dose. At lower iron doses (< 500 mg/L), chemical coagulation yielded better COD, turbidity, and O&G removal. However, chemical coagulation was unable to effectively remove contaminants to meet the offshore discharge limit of 29 ppm O&G. At higher iron doses, EC was more effective at removing COD and O&G. The energy consumption of EC was found to be much higher even when factoring in the energy of production, transporting, and mixing of chemical coagulants, but the overall cost of EC was approximately half the cost of chemical coagulation, and more effective at O&G removal.

2.2 Introduction

Produced water can come from naturally occurring water sources associated with underground oil and gas formations (connate water), or from production fluids injected into underground formations to enhance hydrocarbon recovery [80]. Produced water volumes tend to be much larger than the volumes of produced hydrocarbons; in the U.S. the average is about 7 to 8 barrels of water for every barrel of oil produced [81]. Produced waters can contain high concentrations of sand and sediment, free and emulsified hydrocarbons, suspended and colloidal solids, dissolved salts, minerals and metals, soluble hydrocarbons [e.g., toxic compounds like benzene, toluene, ethylbenzene and xylenes (BTEX) , polycyclic aromatic hydrocarbons and naphthenic acids], and naturally occurring radioactive materials (NORM) [82]. Historically, produced water is managed differently depending on the production method. Typical approaches include: (1) direct onsite deep well injection after oil and suspended solids removal (e.g., most conventional U.S. onshore fields), (2) hauling offsite for deep well injection (e.g., most U.S. shale oil/gas fields), (3) treatment to achieve 29 ppm marine discharge standard (e.g., offshore Gulf of Mexico), and (4) treatment to enable direct reuse in enhanced oil production (e.g., steam flooding in California and Alberta heavy oil fields) [83]. With the more recent ramp up of hydraulic fracturing in the U.S., the cost of hauling for offsite deep well injection has risen dramatically. This, combined with the lack of available fresh water in many oil and gas producing areas (e.g., the Permian basin [84]), have led industries to consider on-site treatment for permitted discharge, direct reuse, or other beneficial reuse [81]. A typical produced water treatment train is composed of the following steps: (1) primary treatment to remove suspended solids and free oil, (2) secondary treatment to remove free oil and macroemulsion (i.e., emulsified oil droplets >1 μm), (3) tertiary treatment to remove microemulsion (i.e., emulsified oil droplets <1 μm) and some soluble hydrocarbons (HC's), and (4) advanced treatment, which could involve softening, desilication and/or desalination to reduce hardness, silica and dissolved substances (salts, metals, soluble HCs, NORM, etc.) [83].

A critical step in any produced water treatment approach is the removal of free and emulsified hydrocarbons, which typically requires chemical destabilization of emulsified oil droplets stabilized by surface charges and/or steric forces imparted by the sorption of surfactants at the oil/water interface. Mechanisms of particle destabilization include: (1) electrical double layer compression, (2) counter-ion adsorption and charge neutralization, (3) polymer adsorption and inter-particle bridging, and (4) precipitate entrapment and "sweep flocculation" [85]. As such, both chemical coagulation (CC) and electro-chemical coagulation or "electro-coagulation" (EC) processes have been widely studied to treat wastewaters with high Oil and Gas (O&G) content, turbidity (or suspended solids), chemical oxygen demand (COD), and total organic carbon (TOC) such as oil-in-water emulsions [86-88], olive oil mill wastewater [89, 90], textile wastewater [90-92], green table olive packaging industry wastewater [93], restaurant wastewater [94], antibiotic removal [95], heavy metals[96], perfluorooctanoic acid (PFOA) removal [97], and refractory wastewater [98].

Conventional CC involves rapid mixing of metal salts and/or polymeric coagulants into the water to destabilize charged colloidal materials, slow mixing to enhance aggregation of destabilized particles and/or coalescence of emulsified oil droplets, and separation of particles by sedimentation, flotation, or filtration [99, 100]. Similarly, EC uses sacrificial metal electrodes (*typ*., iron or aluminum) to supply coagulants *in situ* as water passes through a direct current (DC) electrochemical reactor. In EC, metal ions generated from the anode rapidly hydrolyze to form metal hydroxide precipitates, which ultimately destabilize particles through a combination of charge neutralization and sweep flocculation [101, 102]. The DC electric field also migrates negatively charged species towards the positively charged sacrificial anode, enhancing interactions with metal ions and metal hydroxides [103-105]. Finally, $H_{2(g)}$ gas bubbles generated at the cathode induce some flocculation and flotation [102, 106]. An additional benefit of EC is that it does not increase the chloride or sulfate content of the treated water because in EC the counter anion for iron or aluminum cations sacrificed by the anode is the hydroxide produced at the cathode.

The effectiveness, efficiency and economics of CC and EC have also been reported for various wastewaters. EC is reportedly more economical than CC for palm oil mill effluent treatment [107, 108], textile wastewater and [109], in general, when coagulant demand is small [106, 110]. These cost analyses mainly focused on the cost of purchasing electricity versus chemicals. However, energy demand and the cost of coagulant chemical production and transportation should also be considered. In addition, the direct comparison of EC and CC is not straight forward. Coagulants are dosed in one discrete event for CC with a fixed settling time, while there is continuous dosing for EC throughout the reactor. As such, other than electricity and chemical costs, retention time plays an important role in the capital cost of the two coagulation methods in terms of storage area and treatment tank size. Moreover, the lack of counter ions in EC could minimize undesirable environmental impacts by reducing the amount of chemicals released into the treated water.

In this study, we evaluate the effectiveness, efficiency, and economics of CC and EC to treat produced water, comprising surfactant-stabilized oil emulsions dispersed in a mineral rich simulated produced water matrix. Influent and effluent turbidity, COD, O&G, and TOC were determined from bench tests. Removals were scaled against the total amount of iron introduced by varying both the chemical coagulant dose or the applied current density and reaction time. Energy consumption and operating costs were calculated based on North American market data and experimentally determined operating conditions.

2.3 Materials and Methods

2.3.1 Lab synthesized produced water

Synthetic produced water samples were generated in the laboratory based on previously reported produced water quality data [111]. Hexadecane and sodium dodecyl sulfate (SDS) were combined in a ratio of 9:1 oil-to-surfactant (w/w) [112] in the aqueous electrolyte recipe in Table 2. Recipe for Model Produced Waterbased on the water quality analysis in Table 3. Characteristics of Model Produced Water. The SDS concentration was below its critical micelle concentration[113]. This could have led to less stable oil/water emulsions. However, such oil to surfactant ratio was enough to cause fouling on PSF membranes[112]. The mixture was stirred using an industrial blender (7011G, Waring, Torrington, CT, USA) at 22,000 rpm for 5 min. The produced water samples were prepared immediately before coagulation experiments.

Table 2. Recipe for Model Produced Water

Components	Concentration, mg/L
Hexadecane ($C_{16}H_{34}$)	**1,104**
SDS ($C_{12}H_{25}OSO_3Na$)	**123**
NaCl	**5,850**
$CaCl_2$	**1,110**
$NaHCO_3$	**84**
Silica (as Na_2SiO_3)	**122**
Tannic acid ($C_{76}H_{52}O_{46}$)	**5**

Table 3. Characteristics of Model Produced Water

Characteristics	Unit	Value
pH		8.24
Conductivity,	mS/cm	15.9
Ionic strength	mol/L	0.1617
Hardness	as $CaCO_3$	1,000
Alkalinity	(as $CaCO_3$)	50
TDS	mg/L	7,166
Zeta potential	mV	-65.1
Oil droplet size	nm	1,058
Turbidity	NTU	3,445
Total Solid	mg/L	8,427
TOC	mg/L	1,000
O&G	mg/L	749
COD	mg/L	2,800
UV_{254}	AU	8.495
Color	CU	112

2.3.2 Chemical coagulation experiments

CC experiments were carried out at room temperature (20 ± 2 °C) using a bench-scale jar testing apparatus (PB-700^{TM} Jar Tester, Phipps and Bird, Richmond, VA, USA). The CC process includes three consecutive stages: 1) rapid mixing (200 rpm, 2 min) of coagulant ($FeCl_3$) and produced water, 2) slow mixing (25 rpm, 30 min) to promote flocculation, and 3) quiescent gravity separation (60 min). Effluent samples were withdrawn and measured immediately after gravity separation from the center of the reactor.

2.3.3 Electro-coagulation experiments

EC experiments were performed in a 1,500 mL batch electrolytic cell under galvanostatic conditions at current densities of 5, 10 and 25 mA/cm^2. Iron (Fe) plates were used as both the cathode and the sacrificial anode. The total effective electrode area for 4 electrodes was 168 cm^2. Four electrodes were connected vertically with a gap of 2 cm and connected to the direct current power supply in monopolar parallel mode. Before each test, the iron electrodes were dipped in 10% HCl solution for 10 min and rinsed by deionized water to remove any residual oxides from prior experiments. Water quality indicators were characterized from samples pipetted at different time intervals from the middle layer of the reactor to account for oil removed by flotation as well as sedimentation. The reactor was stirred before samples were taken to determine iron concentration.

2.3.4 Analytical methods

Turbidity was measured using a turbidimeter (2100AN, Hach Instruments, Loveland, Colorado, USA). TOC was determined by a TOC analyzer (Apollo 9000, Tekmar Dohrmann, Mason, Ohio, USA). A calibration curve between O&G (per EPA Method 1664) and TOC was obtained from hexadecane emulsions prepared at different concentrations. O&G reported for experiments were converted from measured TOC values using the calibration curve. COD analyses were conducted by adding the appropriate volume of sample in COD reagent vial and digesting for 2 h at 150 °C in a COD digestor (DRB200, Hach Instruments, Loveland, Colorado, USA). The COD was measured by a UV-vis spectrophotometer (LAMBDA 45, PerkinElmer, MA, USA) at 620 nm.

2.3.5 Iron concentration calculation

Theoretical iron concentration values were calculated using Faraday's law that relates current and time to the total amount of iron ions generated. It was assumed there was no loss of efficiency due to water splitting, heating, or other side reactions, and all dissolved Fe were Fe^{2+} ions.

$$[\mathrm{Fe}] = \mathrm{ItM_w} / \mathrm{FZQ} \qquad (7)$$

where [Fe] is the molar iron concentration, I is the current (A), t is time (s), M_W is the molecular weight of iron (55.845 g/mol), F is Faraday's constant (96,486 C/mol), Q is the effluent volume (L), and Z is the charge on Fe^{2+}.

2.3.6 Energy demand calculations

The power needed for rapid mixing and flocculation in conventional CC, the power of mixing P (W) is determined using the following equation [85]:

$$P = N_p \, \rho N^3 D^5 \qquad (8)$$

where N_p is dimensionless power number ($N_p = 4$, when Reynolds number is larger than 10,000), ρ is the fluid density (kg/m^3); N is the rotation speed (rpm), and D is the diameter of the impeller (m). For the energy consumption associated with transportation (e.g., moving chemicals), several assumptions were made in this study: (1) the chemical coagulant during transportation was $FeCl_3$ in solid form; and, (2) the transportation distance varied from 0 to 1,000 miles. Values of the energy consumption in each process of CC were calculated based on experimental and literature data and are shown in Table 4. Energy Consumption of CC. Energy demand by CC was calculated as follows:

$$E(CC) = CC_p^{Energy} + CC_T^{Energy} + CC_M^{Energy} \qquad (9)$$

Here, CC_p^{Energy} represents energy demand by $FeCl_3$ production, CC_T^{Energy} represents energy demand by $FeCl_3$ transportation, and CC_M^{Energy} represents energy demand by mixing $FeCl_3$. Additional equations for each component are given in Table 7.

The energy consumption per unit volume of water treated by EC includes direct electrical energy input plus the energy cost associated with the production and transportation of sacrificial iron electrode plates. The electric energy input in the EC process is calculated by the following equation:

$$E = UIt / Q \tag{10}$$

where U is applied voltage (V), I is the current (A), t is reaction time (h), and Q is the volume of produced water (m^3). To calculate the energy consumption associated with the transportation of iron plates, the transportation distance was varied from 0 to 1,000 miles, and values of the energy consumption were calculated based on experimental and literature data (Table 5). The energy demand of EC was calculated using the following equation:

$$E(EC) = EC_P^{Energy} + EC_T^{Energy} + EC_D^{Energy} \tag{11}$$

where EC_P^{Energy} represents energy demand by iron sheet production, EC_T^{Energy} represents energy demand by iron sheet transportation and EC_D^{Energy} represents energy demand by iron dissolution. Additional equations for each component is given in Table 7.

Table 4. Energy Consumption of CC

Process	Energy	Units	Reference
Production	**0.97**	**kWh/kg $FeCl_3$**	**[114]**
Transportation	**8.9×10^{-4}**	**kWh/kg Fe/mile**	**[115]**
Fast Mixing	**4.2×10^{-1}**	**kWh/m^3**	**Eq (2)**
Slow Mixing	**8.4×10^{-4}**	**kWh/m^3**	**Eq (2)**

Table 5. Energy Consumption for EC

Process	Energy	Unit	Reference
Production	**3.75**	**kWh/kg Fe**	**[116]**
Transportation	**8.9×10^{-4}**	**kWh/kg Fe/mile**	**[115]**
Electric Power	**2.6, 5.2, 13**	**W**	**5, 10, 25 mA/cm^2**

2.3.7 Operating cost calculations

The operating cost per unit volume of produced water treated by CC includes the cost of electricity used for mixing (rapid and slow mixing), and the cost of purchasing and moving the chemical coagulant. The cost of electricity in mixing is calculated based on the mixing energy consumption and the electricity cost. The price of purchasing and moving of chemical coagulant is estimated based on market prices (Table 6). The operating cost per unit volume of produced water sample treated by EC includes the cost of electricity used to power (i.e., dissolve the iron) the process, and the cost of purchasing and transporting the iron electrodes. The cost of electricity was calculated based on the electric energy consumption and the electricity cost. The price of purchasing and transporting the iron electrodes was estimated based on market prices (Table 6). The cost of chemical and EC were calculated using equations (12) and (13), respectively:

$$\mathrm{C(CC)} = \mathrm{CC_T}^{\mathrm{Cost}} + \mathrm{CC_P}^{\mathrm{Cost}} + \mathrm{CC_E}^{\mathrm{Cost}} \qquad (12)$$

where $\mathrm{CC_T}^{\mathrm{Cost}}$ represents the cost for $FeCl_3$ transportation, $\mathrm{CC_P}^{\mathrm{Cost}}$ represents the price of $FeCl_3$, and $\mathrm{CC_E}^{\mathrm{Cost}}$ represents the electricity cost for $FeCl_3$ mixing. Additional equations of each component is given in Table 7.

$$\mathrm{C(EC)} = \mathrm{EC_T}^{\mathrm{Cost}} + \mathrm{EC_{PP}}^{\mathrm{Cost}} + \mathrm{EC_{SP}}^{\mathrm{Cost}} + \mathrm{EC_E}^{\mathrm{Cost}} \qquad (13)$$

where $\mathrm{EC_T}^{\mathrm{Cost}}$ represents the cost for sheet iron transportation, $\mathrm{EC_{PP}}^{\mathrm{Cost}}$ represents the cost for pig iron, $\mathrm{EC_{SP}}^{\mathrm{Cost}}$ represents the price of electricity for sheet iron production, and $\mathrm{EC_E}^{\mathrm{Cost}}$ represents the electricity price for iron dissolution. Additional equations of each component is given in Table 7.

Table 6. Operating Cost Factors

Item	Cost	Unit	Reference
$FeCl_3$	**2.29**	**$/kg Fe**	**[117]**
Fe_2SO_4	**0.79**	**$/kg Fe**	**[118]**
Iron	**0.2**	**$/kg Fe**	**[119]**
Electricity	**0.1136**	**$/kWh**	**[120]**
Transportation	**1.7×10^{-4}**	**$/kg/mile**	**[121]**

Table 7. Additional equations

Component	Equation
CC_P^{Energy}	0.97 * Weight
CC_T^{Energy}	$8.9 * 10^{-4}$ * Distance * Weight of CC
CC_M^{Energy}	$N_p \varrho N^3 D^5$ * t
EC_P^{Energy}	(9.75 + 0.333) * Weight of iron
EC_T^{Energy}	$8.9 * 10^{-4}$ * Distance * Weight of iron
EC_E^{Energy}	UIt / Q
CC_T^{Cost}	$1.7 * 10^{-4}$ * Distance
CC_P^{Cost}	2.29 * Weight of CC
CC_E^{Cost}	$N_p \varrho N^3 D^5$ * t * 0.1136
EC_T^{Cost}	$1.7 * 10^{-4}$ * Distance
EC_{PP}^{Cost}t	0.2 * Weight of pig iron
EC_{SP}^{Cost}	3.75 * Weight of iron * 0.1136
EC_E^{Cost}	UIt / Q * t * 0.1136

2.4 Results and Discussion

2.4.1 Electro-coagulation

Figure 8(a) and (b) shows the physical appearance of the effluent before treatment and after EC for 20 min. Before treatment, the effluent is a homogeneous white milky solution. After 20 min of EC at 32 mA/cm^2 (data not reported), 3 distinct layers can be distinguished as the floating floc, middle "clean" layer and sedimented precipitate layer. The floating floc was mostly formed from precipitate adsorption onto $H_{2(g)}$ gas bubbles produced by reduction of $H^+_{(aq)}$ ions at the cathode. Green and brown colors characteristic of Fe^{2+} and Fe^{3+} ions, respectively, indicate the presence of both oxidation states of iron in the floating floc and the sedimented precipitates.

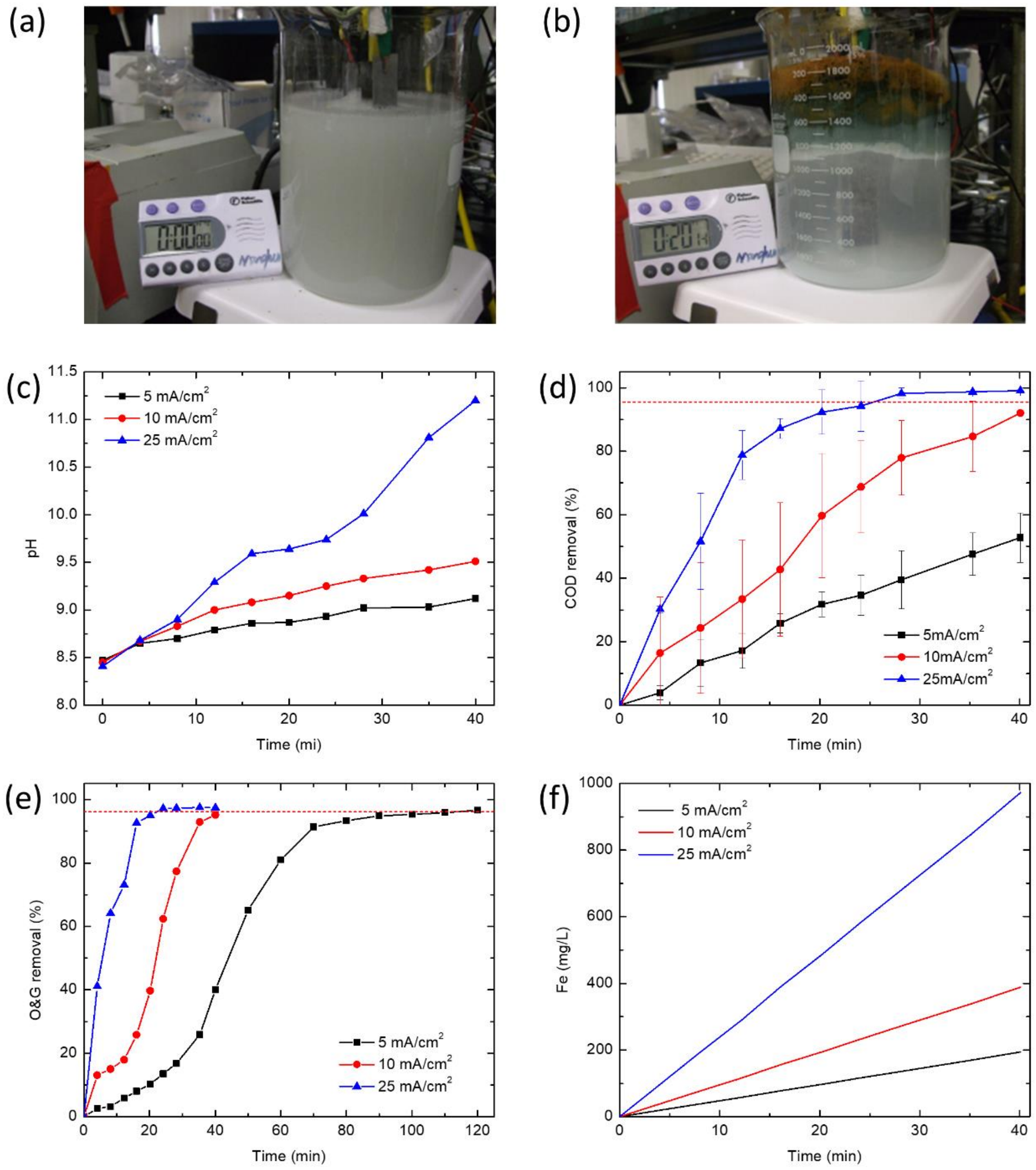

Figure 8. (a) Freshly prepared simulated effluent before EC, (b) effluent after 20 min of EC at 32 mA/cm2. (c) pH changes with time during EC at different current densities. (d) COD removal and (e) O&G removal vs time during EC at different current densities. (f) Theoretical iron concentration as a function of time at different current *densities.*

The solution pH increased with time, particularly when high (25 mA/cm^2) current densities were applied, with the pH increasing from 8.4 to 11.2 over the experiment (Figure

8c). For the lower current densities (5 and 10 mA/cm^2), pH only increased slightly from pH 8.5 to pH 9.5, and from pH 8.5 to pH 9.1, respectively. The pH increase results from reduction of H_3O^+ ions into $H_{2(g)}$ and OH^- ions at the cathode, which is not stoichiometrically balanced by $Fe^{2+/3+}$ ions produced at the anode; the charge is balanced, but some iron reacts with oil emulsions and other anionic species, so there is continuous production of excess of OH^- that drives up the pH. Empirically, the evolution of $H_{2(g)}$ gas bubbles at the cathode was visibly much higher at 25 than 10 and 5 mA/cm^2. This could explain the exceptional O&G removal performance at 25 mA/cm^2 compared to 5 and 10 mA/cm^2, due to $H_{2(g)}$ gas bubbles-derived flotation.

Figure 8 (d) and (e) shows COD and O&G removal respectively, as a function of time. The red dashed line represents the removal needed to meet the offshore discharge limit of 29 ppm O&G and 125 ppm COD (in the U.S. Gulf of Mexico). EC achieves these discharge limits within 28 min at 25 mA/cm^2 but took longer to reach the O&G discharge limit at 5 and 10 mA/cm^2. Figure 8 (f) presents the theoretical dissolved iron concentration as a function of time, estimated using Faraday’s law. Comparing Figure 8 (d) and (e) with Figure 8 (f), the rate of iron dissolution at different current densities correlates with the removal rates of COD and O&G. Operating EC at 25 mA/cm^2 allowed the fastest iron dissolution rate, which in turn led to the fastest COD and O&G removal, followed by 10 mA/cm^2 and then 5 mA/cm^2. Longer reaction times are required for lower current densities to release the same amount of iron coagulant into the water. For example, at 40 min, O&G removal achieved using a current density of 25 mA/cm^2 was the same as that achieved at 120 min using a current density of 5 mA/cm^2.

2.4.2 Effectiveness of chemical coagulation and electro-coagulation

Figure 9 illustrates the removal and concentrations of turbidity, COD and O&G as a function of iron concentration, for CC and EC at different current densities. Table 8 presents the discharge limit that needs to be reached in order to meet offshore discharge regulations. CC performs better than EC in terms of turbidity removal; while 345 mg/L of iron is required to reach the discharge limit (25 NTU turbidity) using CC [122]. For EC, a slightly higher concentration of 389 mg/L of iron is required at a current density of 10 mA/cm^2. Turbidity removal by EC was not able to meet the discharge limit (highest 98.1%). However, CC was unable to remove sufficient O&G to reach the discharge limit (29 mg/L O&G) [123], achieving, at the maximum, only 85.5% removal. In contrast, EC achieved 97.4% O&G removal. Importantly, overdosing the chemical coagulant did not improve O&G removal, but instead restabilized the flocs resulting in lower O&G removal rates (Figure 9c). The highest removals achieved by CC were 99.9% (turbidity), 96.6% (COD) and 85.5% (O&G). The highest removals achieved by EC were 98.1% (turbidity), 99.1% (COD) and 97.4% (O&G). Overall, EC could adequately remove COD, and O&G to meet the discharge limit, while CC was unable to reach the discharge limit for O&G, it was able to reach sufficient turbidity removal to meet discharge limits. COD and O&G removal by both coagulation methods were above 90%, which is consistent with previous research [86, 106].

It is known that CC lowers effluent pH while EC does the opposite [124, 125]. Low removal rates at lower iron concentrations for EC compared to CC could be due to the anionic surfactant stabilizing effects at higher pH. These changes in pH affect the zeta potential of suspended particles causing them to either destabilize or stabilize [126]. In previous studies, hexadecane and silica have been shown to have increasingly negative zeta potentials beyond the isoelectric point (at around pH 2) as pH increases from 2 to 9 [127, 128]. While changes in the zeta potential of silica and hexadecane do not work in favor of EC at high pH, the dissolution of sufficient iron coagulant is able to destabilize the suspension, resulting in continuous removal of COD, turbidity and O&G with increased iron concentration (Figure 9). This may explain the high concentration of iron needed during EC before COD and O&G removal reached the discharge limit. The exceptional removal of O&G by EC compared to CC could be caused by floc flotation. Production of $H_{2(g)}$ gas bubbles that evolve from the cathode during EC serve as a surface for coalescence of oil droplets before floating towards the water surface. This is consistent with a study that has shown improvement in O&G removal when microbubbles were coupled with a chemical coagulant [129].

Table 8. Discharge Limit and Target Removal for Offshore Effluent Disposal

Process	Raw	Discharge limit	Target removal, %
Turbidity, NTU	**3,445**	**25**	**99.3**
COD, mg/L	**2,800**	**125**	**95.5**
O&G, mg/L	**749**	**29**	**96.1**

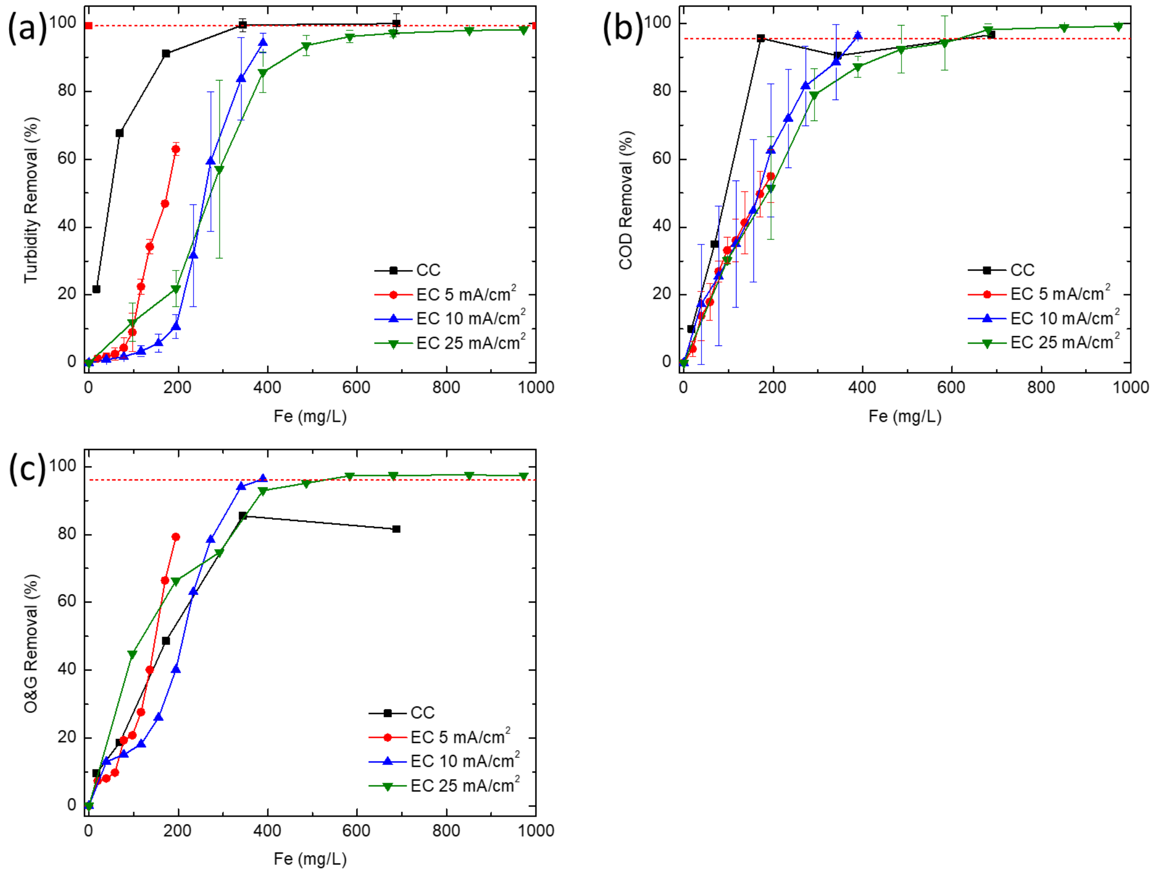

Figure 9: Influence of iron concentration on effluent concentration and removal of CC and EC (a) Turbidity removal; (b) COD removal; (c) O&G removal.

2.4.3 Energy consumption of chemical coagulation and electro-coagulation

The energy demand by CC includes direct energy input for mixing (rapid mixing and flocculation), as well as energy associated with the production and transportation of the chemical coagulant. For EC, the energy demand is associated with the production and transportation of iron electrodes, along with the electric energy consumed onsite. Input values for energy demand calculations are provided in Table 4 and 5. For EC, 10 mA/cm^2 was chosen for energy demand analysis because of its fast Fe dissolution and at the same time minimal side reactions.

The energy demand of CC and EC are shown in *Figure* 10 as functions of transportation distances (for coagulant chemicals and iron electrodes) and removal of turbidity in *Figure* 10 (a), COD in *Figure* 10 (b) and O&G in *Figure* 10 (c). The red dashed lines represent the removal required to meet offshore discharge limits. EC is a highly energy intensive process. The energy demands of EC is consistently higher than CC at all removal rates and transport distances. In *Figure* 10(d), the energy demand per order of removal (90% removal) of turbidity and COD for EC was around 4.3 times that of CC when no transportation was required (at 0 miles). Energy per order removal of O&G using CC could not be calculated since the highest removal achieved was only 85.5%. At 1,000 miles of transportation distance, the total energy consumption (compared to 0 miles transportation distance) using EC increased by 8.6%, while the total energy consumption using CC increased by 32%. Transporting $FeCl_3$ is much more energy intense than transporting Fe plates. In iron salts, iron is a much smaller mass fraction (e.g., 21% w/w for $Fe/FeCl_3 \bullet 6H2O$) of the chemical than for solid iron plates. Thus, the energy demand of $FeCl_3$ transportation is largely governed by the inactive fraction of metal salt coagulants. For EC on the other hand, with efficient usage, the mass of raw materials used in EC could account for almost all coagulant produced. As distances increased, energy consumption increased proportionally. Transportation of electrode iron was a significant, but small fraction of EC energy demand. As iron is a commonly used material, there is a good possibility that the local availability of iron is higher than $FeCl_3$. In other words, it is likely that produced water treatment facility need to purchase chemical coagulant from vendors in other places which introduces more transportation energy consumption.

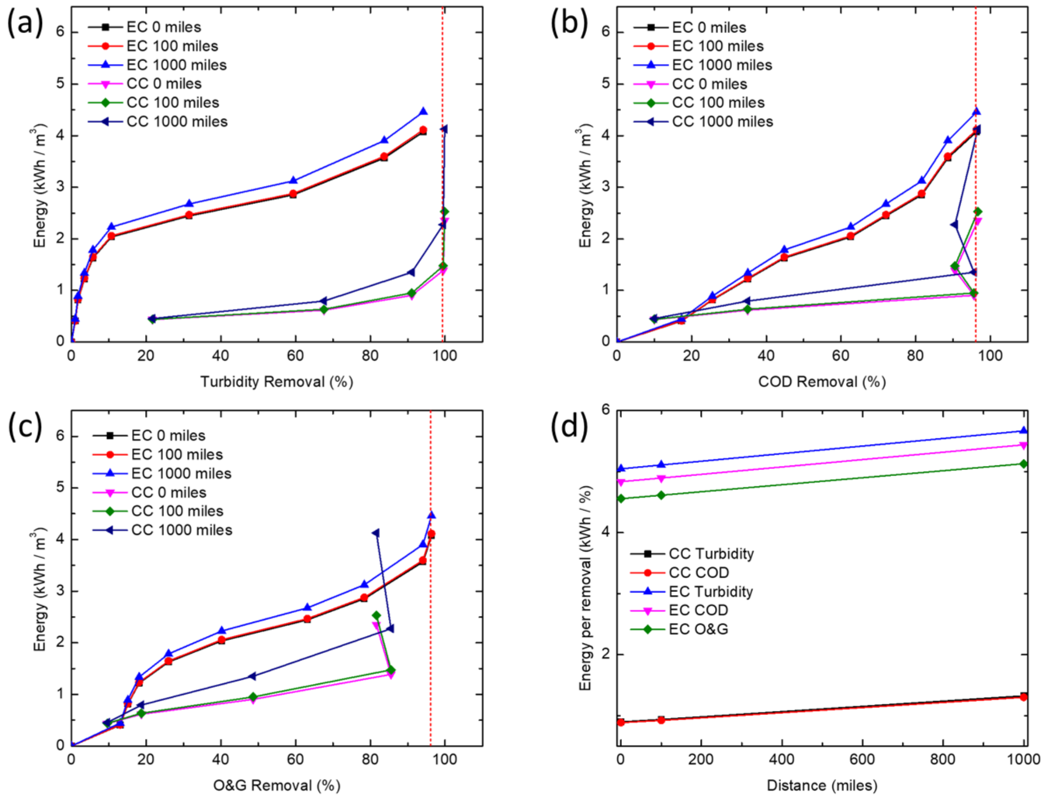

Figure 10:. *Influence of transportation distance on energy consumption of EC and CC with (a) turbidity removal; (b) COD removal; (c) O&G removal. (d) Influence of transportation distance on energy consumption of EC and CC at different distances at 90% removal coagulant dosage.*

2.4.4 Comparison of operating costs

Input values used to determine operating costs of CC and EC are shown in Table 6. In *Figure* 10, operating costs for CC and EC (10 mA/cm^2) are compared for a range of removals and transportation distances for turbidity in *Figure* 10 (a), COD in *Figure* 10 (b) and O&G in *Figure* 10 (c). Although the energy demand of EC is much higher than that required for CC, operating costs are higher for CC than EC, particularly for removal above 90%. Comparing the cost of iron coagulant at which both methods achieve an order of removal (*Figure* 10(d)), the cost of using CC is around 1.8 to 2 times the cost of using EC within 0 to 1,000 miles transportation distance for turbidity and COD removal. CC did not meet the discharge limit for O&G at any concentration tested. The unit price of chemical coagulant was 4 times higher than iron metal, and price per unit of Fe from the chemical coagulant is 11.5 times higher than pure iron. Since transportation costs are governed by the weight of inactive components of the chemical coagulant, if a cheaper coagulant, $FeSO_4$, is used and assuming the same amount of iron is required to reach equivalent rejection, the cost of using CC would still be higher because the unit price of iron from $FeSO_4$ is 4 times higher than iron metal (because of the high water content). On the other hand, both the costs of iron electrodes and electricity used for *in situ* production of the iron-based coagulant were smaller for EC. However, electricity price may vary at different locations and the price of electricity used in this cost analysis is based on industrial pricing in Texas.

Another advantage of using EC found in this study is that the time required to achieve equivalent removals were much longer for CC (92 min) than for EC (up to 40 min). Therefore, the size of equipment needed for CC would be proportionately larger; hence, the capital cost and footprint of CC reactors and clarifiers may be higher. Further, as $FeCl_3$ is corrosive and attacks metals rapidly, it should be stored in either fiberglass-reinforced polyester or rubber-lined steel tanks and not in containers made by aluminum, brass and stainless steel; hence, chemical coagulants ($FeCl_3$) may require special onsite storage and handling, which further increase capital and EH&S costs [130].

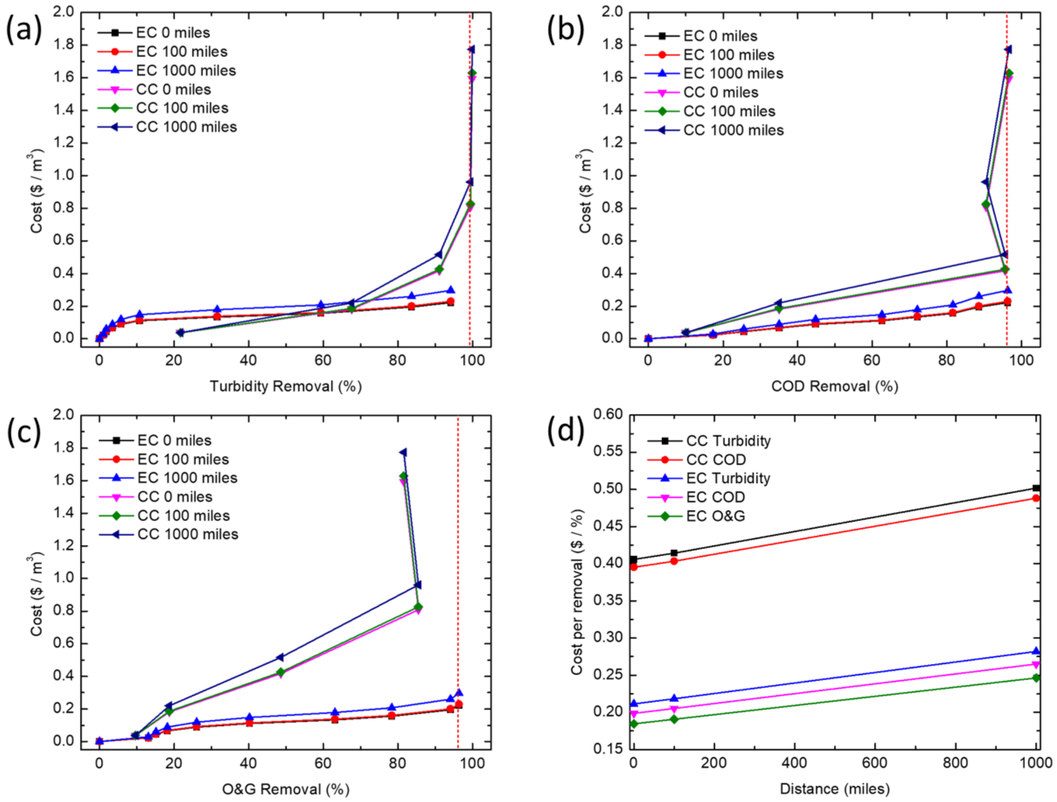

Figure 11: Influence of transportation distance on cost of EC and CC with (a) turbidity removal; (b) COD removal; (c) O&G removal. (d) Influence of transportation distance on cost of EC and CC at different distances at 90% removal coagulant dosage.

2.5 Conclusions

In this study, CC and EC were compared for removal of turbidity, COD and O&G from a simulated synthetic produced water. CC was able to achieve high COD and turbidity removals at much lower concentrations of iron than EC but is unable to effectively remove enough O&G to meet offshore discharge limits, even at very high coagulant doses (>345 mg/L). At higher iron concentrations, EC removed COD and O&G adequately to meet typical discharge standards, whereas CC would require additional treatment (e.g., flotation or filtration) to meet most O&G discharge limits. Coagulant overdose leading to poorer coagulation performances seem to only affect CC. This points to the need for extensive testing before an optimum dosage of chemical coagulant could be established, thus further increasing operational costs. While CC is a more established and proven technology, EC offers certain advantages for resource extraction industries like oil and gas. In particular, oil production is increasingly explored in remote locations (e.g., offshore, Gulf of Mexico, Athabasca oil sands, Alaskan North Slope, Central Australia, etc.) far from major chemical production centers, so supplying water treatment chemicals could pose significant logistics challenges, energy demand, and high cost for produced water treatment. Additionally, EC offers the opportunity for more compact systems while minimizing onsite chemical storage. Processes like EC, where water treatment chemistry is generated *in situ* and onsite, may reduce energy demand and operating costs associated with meeting existing and future produced water treatment requirements.

Chapter 3: Exploration of 5052 aluminium alloy electrode during electrocoagulation in groundwater

3.1 Abstract

Electrocoagulation (EC) of synthetic groundwater was conducted using sacrificial 5052 aluminium alloy in a flow-through EC reactor with short retention times under varying hydrodynamic and current density conditions. The treated water was allowed to settle for 24 h and achieved silicate removal of up to 50 ± 4%, and hardness removal of 11 ± 1 %. Physical, chemical, and electrochemical characterization was performed to explore changes in electrode surface morphology and composition. Electrochemical impedance spectroscopy (EIS) showed that chemical reactions at the electrode/water interface are sensitive to changes in the immediate chemical environment. We demonstrate that the most energy intensive step in EC is aluminium dissolution at the anode, which is worsened by a thickening of an aluminium oxide film at the anode. The high flow rate in the system prevented the accumulation of aluminium hydroxide solids or aluminium ions at the electrode/water interface, thereby preventing the formation of thick scalants and amorphous $Al(OH)_3$ on the cathode and anode respectively. This prevented an increase in the energy requirement of the system after up to 60 minutes of operation. It was further demonstrated by EIS that under these conditions the charge transfer resistance was constant throughout the duration of the experiment.

3.2 Introduction

According to the National Groundwater Association (NGWA), groundwater accounts for 29% of the freshwater supply in USA [6], with 41% of the USA population regularly depending on groundwater for their drinking needs. A multitude of water purification methods exist for the treatment of groundwater for potable applications. While membrane separation techniques such as reverse osmosis and nanofiltration are effective for the removal of salinity and ppm levels of unwanted substances [131-133], they foul easily [134-137]. To minimize fouling, a pre-treatment step that involves coagulation/flocculation is often necessary [138, 139]. The coagulation/flocculation process removes unwanted species such as dissolved organic carbon, hardness, and silica [140, 141]. The coagulation/flocculation process works by promoting the aggregation of fine particles and dissolved species into larger flocs, which can be readily removed through sedimentation, owing to their higher settling rates. After allowing sufficient time for floc formation and settling, the clarified water is moved to a secondary treatment process (e.g., filtration).

Coagulation can be achieved through either chemical addition or electrocoagulation (EC). In chemical coagulation, metal salts (such as $Al_2(SO_4)_3$ and $FeCl_3$) are added to the groundwater where they rapidly form metal hydroxide species that neutralize charges, form flocs, and promote the removal of contaminants [55, 142, 143]. Often, it is difficult to estimate a suitable dosage of chemicals to effectively treat the water, resulting in extensive trail-and-error testing to find an appropriate dosage [144, 145]. In addition, since the metal salts induce water hydrolysis that results in the acidification of the water, pH adjustment is often necessary before the water can be used [145, 146]. Furthermore, the addition of coagulant salts and alkalizing agents (e.g., NaOH) to the water can lead to a significant increase in the salinity of the water, although this is only an issue when large quantities of coagulants are used.

EC is an alternative process to chemical coagulation where instead of dosing chemical coagulants, sacrificial aluminium or iron electrodes are dissolved/corroded into untreated water through electrochemical oxidation to produce the coagulating species. Water electrolysis at the cathode produces hydroxide ions, aluminium dissolved at the anode combines with these hydroxides to form metal hydroxides as the coagulating species. Because of this, the pH of the water does not experience the dramatic pH swings typical of chemical coagulation, no pH adjustment are needed, and the subsequent increases in the water's salinity are avoided.

The formation of the coagulating species ($Al(OH)_3$) from the dissolution of aluminium plates can be described by the following reactions [51-53]:

At the anode:

$$Al \rightarrow Al^{3+} + 3e^- \tag{14}$$

$$2H_2O \rightarrow 4H^+ + O_2 + 4e^- \tag{15}$$

At the cathode:

$$2H_2O + 2e^- \rightarrow H_2 + 2\,OH^- \tag{16}$$

In the bulk solution:

$$Al^{3+} + 3H_2O \rightarrow Al(OH)_3 + 3H^+ \tag{17}$$

The formation of poly-hydroxides such as $Al(H_2O)^{3+}$ and $Al_6(OH)_{15}^{3+}$ are also possible [54-56].

EC has been studied for the purification of groundwater in processes that involve inorganic chemicals such as arsenic [147], nitrates [146, 148], chromium [149], and organic substrates like petroleum [150], humic acids [151], and perfluoroalkyl substances [152]. Most studies on electrocoagulation have focused on water quality [153-157]. However, there is limited knowledge on how changes on the electrode surface may impact EC. EC is not always efficient in purifying water in terms of energy costs [158]. Several factors such as current density, flow rate, plate spacing, and electrode and solution composition may affect the effectiveness of contaminant removal [159, 160]. Passivation of aluminium electrodes, as well as high solution resistance may result in excessive energy requirements [57-59]. The presence of pitting promoters is also important to allow de-passivation of aluminium. Noorzalila et al. reported an improvement in electrocoagulation performance in landfill leachate using Al 5052 vibration-induced plates due to improved ionic transfer and bubble detachment in a batch process [60]. Martin et al. compared passivation of pure aluminium and Al 1050 with a rough or smooth surface in neutral electrolyte solutions [61]. In the study, a rough surface experienced “spontaneous de-passivation” even without the addition of pitting promoters such as chloride ions.

In this study, Al 5052 plates were used as the sacrificial electrode (anode) and cathode in an EC process for the treatment of synthetic groundwater. The EC cell had a flow-through design, equivalent to a plug flow reactor (PFR), with a short hydraulic retention time (HRT). Changes on the aluminium electrode surface were characterized over time using a suite of physical and chemical tools, and the resulting changes in water quality are discussed.

3.3 Material and Methods

3.3.1 Materials:

EC experiments were performed with 0.081 cm thick 5052 Aluminium (96.8% Al, 2.47% Mg, 0.25% Fe, 0.13% Si, 0.2% Cr, 0.056% Mn, 0.023% Ti, 0.019% Cu, 0.018% V, 0.013% Zn, 0.01% Ga, 0.007% Ni) purchased from McMaster-Carr. Electrochemical measurements were performed with 0.254 cm thick 5052 Aluminium provided by WaterTectonics. $MgCl_2 \cdot 6H_2O$, $CaCl_2 \cdot 2H_2O$, $NaSiO_4 \cdot 5H_2O$ and 37% HCl were used as purchased from Acros Organics, $NaHCO_3$ and 200 proof ethanol were used as purchased from Fisher Chemical, DI water was provided in-house.

3.3.2 Methods:

3.3.2.1 Synthetic Groundwater

Synthetic groundwater was formulated based on the water quality characteristics of groundwater from the City of Longville, Washington, kindly provided by WaterTectonics. The composition of the synthetic groundwater is listed in Table 1.

Table 9: Synthetic Groundwater content

Chemical	Concentration (mM)
Na_2SiO_3	**0.85**
$NaHCO_3$	**2.2**
HCl	**1.4**
$CaCl_2$	**0.676**
$MgCl_2$	**0.272**

3.3.2.2 Electrocoagulation method

A flow-through EC cell with the working and counter electrodes spaced 0.32 cm apart (Figure 12) was used in all experiments. Synthetic groundwater was pumped at 3 different flow rates (0.5, 1 and 1.46 litres per minute (LPM)), corresponding to an HRT of 0.73, 1.06, and 2.1 seconds, respectively, and a velocity of 21, 14 and 7.2 cm/s, respectively. The groundwater was pumped using a peristaltic pump (Cole Parmer, IL, USA). Prior to the EC experiments, 5052 aluminium was polished with 150 grit sandpaper, degreased with ethanol and flushed with DI water. The total exposed area of the anode and cathode was 55.6 cm^2 each. A DC power supply (Siglent Technologies SPD3303X, MN, USA) capable of supplying up to 3.2 A and 60 V of power was connected to the electrodes. The output current and voltage were logged into a computer using Python 3.0. 3 different current densities (2, 10 and 25 mA/cm^2) were tested. Water samples were collected every 5 min until 20 L of synthetic groundwater passed through the system. pH, conductivity, turbidity as well as silica and hardness removal were measured after a settling time of 24 h.

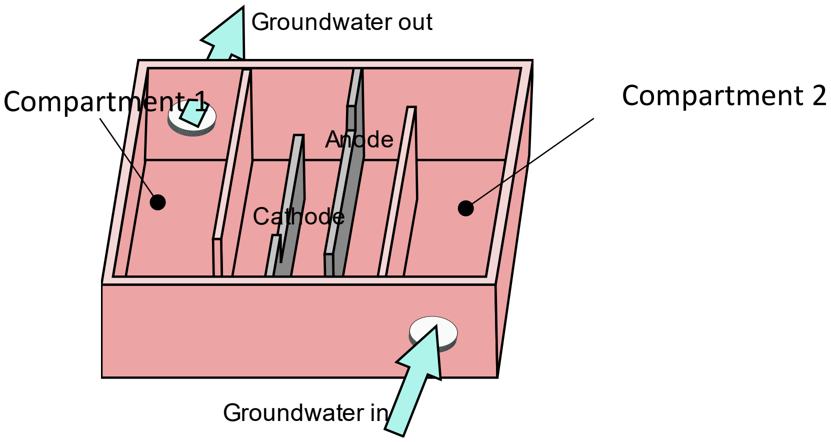

Figure 12: Flow through EC cell design used for the experiments in this study.

3.3.2.3 Electrochemical measurements

Electrochemical measurements were conducted using a potentiostat (CHInstruments, CHI6005E) with a 3-electrode setup potentiostat (which can provide a maximum of 10 V and 1.0 A). Both working and counter electrodes were 5052 Aluminium plates, and the reference electrode was Ag/AgCl in 3 M KCl with saturated AgCl. Prior to use, the aluminium electrodes were polished with 150 grit sandpaper, degreased with ethanol and flushed with DI water. To achieve the high current densities needed to drive the EC process using the potentiostat, the working electrode was masked so that only 2 cm^2 were exposed to the solution – this allowed us to maintain identical flow conditions during EC experiments and electrochemical characterization steps; during these electrochemical characterization experiments, the counter electrode surface area was kept at 55.6 cm^2. Electrochemical measurements were performed in the flow-through EC reactor (Figure 12), with the reference electrode placed in compartment 1 when electrochemical measurements were made to the anode, and in compartment 2 when electrochemical measurements were made to the cathode. Electrochemical measurements were performed at both open circuit potential (OCP) and during the application of higher voltages needed to drive the EC process.

Electrochemical Impedance Spectroscopy (EIS) was conducted using an AC amplitude of 5 mV in the frequency range from 1MHz to 0.1 Hz, with 12 points collected per decade. EIS curves were modelled and fitted using the CHI software. Tafel plots were obtained using a scan rate of 1 mV/s in the anodic direction.

In addition, EIS experiments were conducted using a rotating disc electrode (RDE). The RDE had a diameter of 5 mm and was made of 5052 aluminium alloy, polished to mirror finish

(Pine Research). The RDE was placed in the flow through cell used in the EC experiments. An aluminium 5052 alloy plate with 56 cm^2 surface area was used as the counter electrode, and a Ag/AgCl electrode was used as the reference electrode.

3.3.2.4 Surface and Water Characterization

Solution pH was measured using a portable pH meter (Thermo Scientific, Orion 720A), and turbidity was measured using a turbidity meter (Hach, 2100P). Al, Si, Mg and Ca concentrations were measured using inductively coupled plasma-mass spectroscopy (ICP-MS, PerkinElmer, NexION 2000). Contaminant removal efficiency was calculated using the following equation:

$$Removal\ efficiency\ (\%) = \frac{C_o - C_f}{C_o} * 100 \qquad (18)$$

Where C_o is the initial concentration of silica or hardness and C_f is the supernatant concentration of silica hardness after EC and 24 hours of settling.

The chemical composition of the electrode surface was determined using X-ray photon spectroscopy (XPS) (Kratos Axis Ultra DLD spectrometer equipped with a monochromatic Al Kα X-ray source). High-resolution spectra were calibrated using carbon tape (Ted Pella) with a known C1s binding energy of 284.6 eV. Raw data were processed using CasaXPS software (version 2.3.19). The electrode surface was characterized using scanning electron microscopy (SEM ZEISS, Supra 40VP) equipped with an energy-dispersive X-ray detector (EDAX). Cross sections of the electrode were obtained using ion beam etching and viewed by transmission electron microscopy (TEM, FEI Titan S/TEM). The electrode surface area index was obtained using an optical profiler (Bruker NT9300).

3.4 Results and Discussion

3.4.1 Electrocoagulation

EC was conducted in a cell as depicted in Figure 12 at different flow rates and current densities; pH, conductivity, turbidity, silica, and hardness removal were measured for the different time intervals after a settling time of 24 h and are shown in Figure 13. It can be seen that both hardness and silica removal rates improve with increasing current densities. Turbidity after settling on the other hand, becomes higher with increased current densities, plateauing at around when 4 NTU when EC was run at 25 mA/cm^2.

The total concentration of dissolved aluminium (measured using ICP-MS) as a function of the charge loading (C/L) is shown in Figure 14(a). The concentration of aluminium was compared to the theoretical concentration of aluminium that can be dissolved as a function of current passed through the electrodes, estimated using the Nernst equation [161]:

$$Theoretical\ Al\ concentration = \frac{I*t}{F*Z*V} \qquad (19)$$

where I is current, t is the retention time, F is the Avogadro number, Z is the aluminium ion charge and V is the volume of water passed between the electrodes within the retention time.

It was found that the experimental aluminium concentration measured by ICP-MS was higher than the theoretical Al concentration in this study, and the % increases with higher charge loading (Figure 14(a)). The % difference between theoretical aluminium concentration and total aluminium concentration was calculated using the following equation:

$$\% \, difference = {(Total\ Al\ conc - Theoretical\ Al\ conc)}/{Theoretical\ Al\ conc} \qquad (20)$$

This difference reaches a maximum at 57 C/L and starts to decrease thereafter. We attribute the higher experimental aluminium concentration to high local hydroxide concentration at the surface of the cathode that causes the aluminium cathode to corrode and release aluminium into the aqueous stream [162-164]. At high pH, aluminium predominantly exists in the form of AlO^{2-} according to the Pourbaix diagram [165]. Hydrogen evolution at the cathode could also lead to the formation of aluminium hydrides (AlH^{3+} and AlH^{2+}), which could also lead to the observed aluminium loading [166]. Aluminium corrosion in alkaline media begins from the formation of an aluminium hydroxide film, followed by the incorporation of hydroxide ions into the film and migration towards the aluminium / film interface. The aluminium hydroxide film is then chemically attacked by hydroxide ions to form soluble aluminate ($Al(OH)_4^-$) according to the following reactions [162]:

$$Al + 3OH^- \rightarrow Al(OH)_3 \qquad (21)$$

$$Al(OH)_3 + OH^- \rightarrow Al(OH)_4^- \qquad (22)$$

Based on the above chemical reactions, the aluminium dissolution rate at the cathode will depend on the concentrations of $Al(OH)_4^-$ and OH^- ions. As the transport limit of $Al(OH)_4^-$ ions is reached at the electrode/electrolyte interface, less Al can be hydrolysed into the solution and the % difference between theoretical and measured Al concentration becomes increasingly dominated by Al dissolution at the anode. Thus, the % difference in theoretical and measured dissolved Al decreased. Contrary to most studies, solution pH did not increase as EC proceeds (Figure 14(b)). This could be due to hydroxide ions formed at the cathode being completely taken up by Al^{3+} ions to form $Al(OH)_3$ or possibly poly hydroxides in the bulk solution. Changes in pH for the different flow rates is shown in Appendix 3. 1.

The concentration of Al measured in the supernatant after a 24h settling period was measured as a function of the charge loading (Figure 14(a)). At low charge loading (30 C/L), the concentration of Al in the supernatant was nearly identical to the theoretical and measured concentrations, indicating that at these low charge loadings, little floc was formed. Incidentally, this correlates well with the observed Si and hardness removal at low current densities (all flow rates with 2 mA/cm^2) and high flow rates, which showed low removal, emphasizing the importance of floc formation for water quality enhancement (Figure 14(c) and Figure 14(d)). Importantly, the concentration of Al in the supernatant plateaued, and actually somewhat declined, with increasing charge loading (while total Al concentrations increased), indicating that floc formed and settled out at higher charge loadings. As the current density increased, the total Al concentration increased, and as a result, silica and hardness removal improved. Silica reached the highest removal efficiency of 50 ± 4% and hardness removal reached 11 ± 1 % at the highest charge loading investigated in this study (167 C/L).

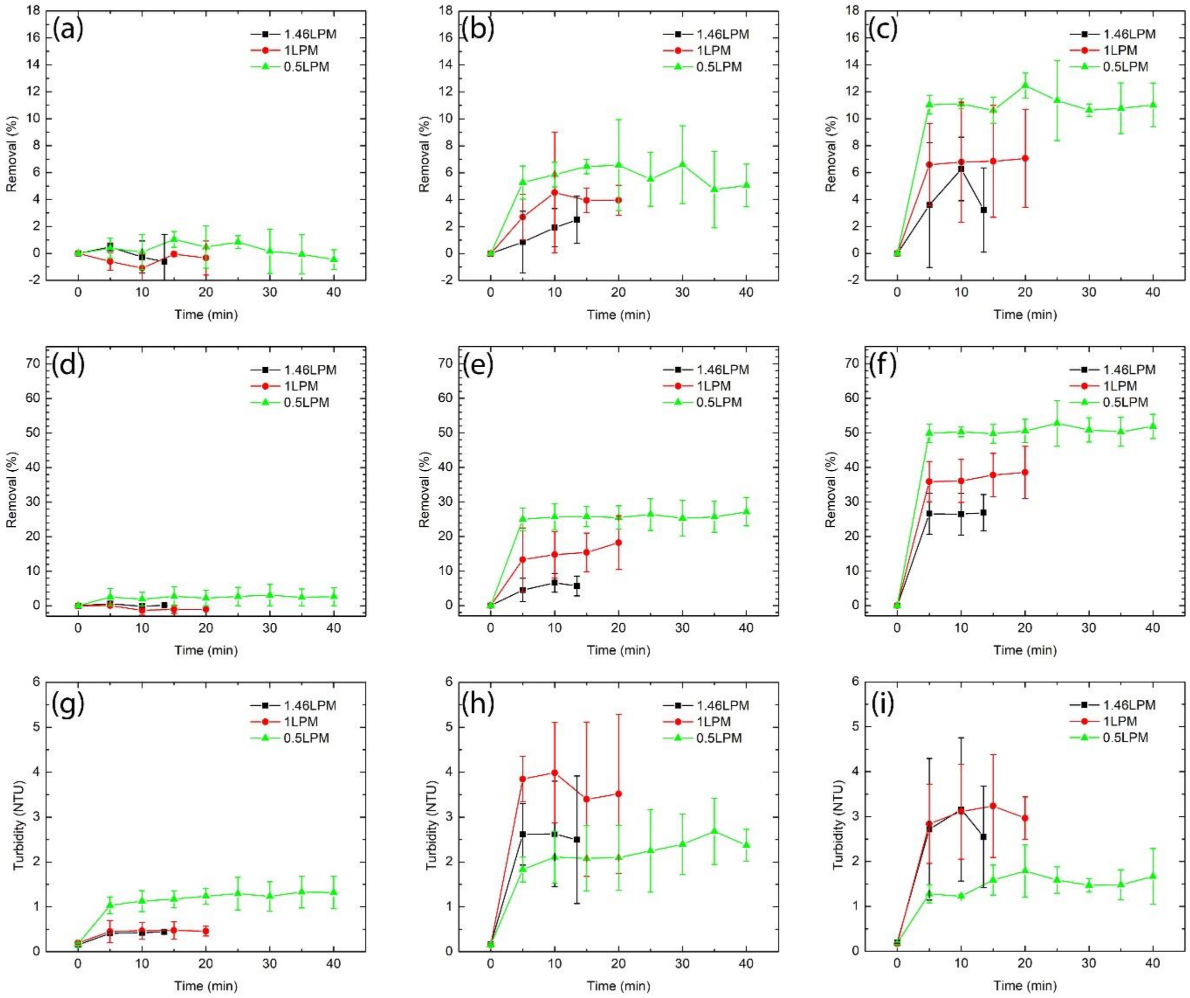

Figure 13: Hardness removal from synthetic groundwater at (a) 2mA/cm², (b) 10mA/cm² and (c) 25mA/cm². Si removal from synthetic groundwater at (d) 2mA/cm², (e) 10mA/cm² and (f) 25mA/cm². Turbidity changes in synthetic groundwater at (g) 2mA/cm², (h) 10mA/cm² and (i) 25mA/cm².

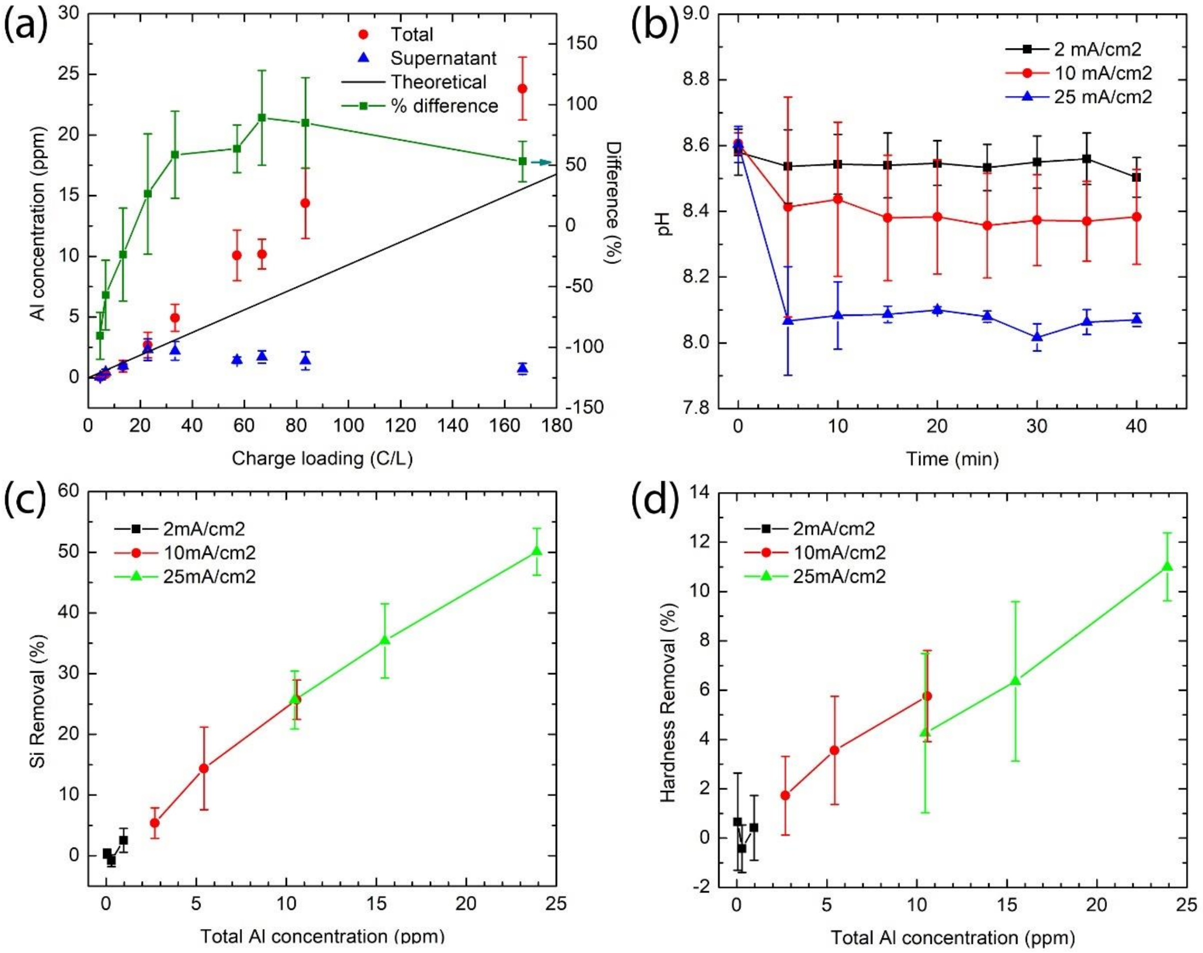

Figure 14: (a) Aluminium concentration in treated synthetic groundwater measured by ICP-OES plotted against charge loading for total dissolved aluminium, supernatant aluminium and theoretical aluminium concentrations. (b) Silicon and (c) hardness removal (%) from synthetic groundwater supernatant measured by ICP-OES plotted against charge loading. (d) treated synthetic groundwater pH changes overtime at a flowrate of 0.5 LPM.

3.4.2 Electrode characterization

The voltage necessary to drive the EC process at a flow rate of 0.5 LPM, and current densities of 2, 10 and 25 mA/cm^2 were recorded (Appendix 3. 2). The stable voltage at the different current densities indicates that minimal electrode cathode scaling occurred, as mineral scale creates a layer that increases the resistance to charge transfer, requiring higher voltages to maintain a given current density.

XPS was performed on the electrodes used in the experiments at the different current densities at 0.5 LPM to determine changes to the their surface chemical composition, with the data plotted as a ratio between the % atomic composition of a given element to the % atomic composition of aluminium (Figure 15(a) and Figure 15(b)). The original atomic % of the elements are displayed in Appendix 3. 3. On both the anode and cathode at all current densities, the ratio between oxygen and aluminium increases after EC indicating the presence of a thicker layer of aluminium oxide, or the formation of metal oxide/hydroxide scale. A small amount of magnesium and calcium detected on the anode were likely part of the aluminium 5052 alloy content and impurities [167]. At the cathode, the calcium and magnesium ratio increased after EC, indicating the formation of scalants.

In cross-sectional TEM images of the electrode surface for a fresh piece of aluminium, the anode, and the cathode after EC at 25 mA/cm^2 for 40 min, a second aluminium phase, likely aluminium oxide, was observed (Figure 15(c)-(e)). For fresh aluminum, the aluminium oxide thickness was only 3.5 ± 0.5 nm. However, after EC, the second phase thickness increased to 7 ± 1 nm at the anode, which is consistent with the XPS results showing an increase in the O/Al ratio on the anode. In contrast, the aluminium oxide layer on the cathode did not exhibit a single layer like that of a fresh piece of Al or the anode and had an average thickness of 5 ± 2 nm. This could be caused by different dissolution mechanisms and environmental conditions at the cathode and anode. While aluminium was electrochemically dissolved at the anode with a high concentration of oxygen, aluminium dissolution was purely chemical in nature on the cathode, i.e., driven by hydrolysis (Equations 21 and 22).

Figure 15(f)-(h) show SEM images of fresh aluminium, the anode, and cathode surfaces after EC at 25 mA/cm^2 for 40 min, respectively. At the anode (Figure 15(g)), crystalline square pits were observed across the entire surface, which are a result of aluminium dissolving at certain facets of the aluminium lattice [168]. At the cathode (Figure 15(h)), some mineral scale was observed together with some circular pits. The coverage of scalants increases with current density, where coverage was the highest at 25mA/cm^2 followed by 10mA/cm^2 and 2mA/cm^2 (Appendix 3. 6). The shallow circular pits were observed on cathodes subjected to 10 and 25 mA/cm^2. The pits are formed due to high local pH at the cathode, which leads to aluminium dissolution [169, 170]. Importantly, these pits were observed on 5052 aluminium cathodes even when used in a Na_2SO_4 solution (i.e., a solution with no pitting agent), in which case the anode did not experience significant corrosion (Appendix 3. 7(a)), strengthening the claim that cathodic dissolution does occur on aluminium surface as a result of the elevated local pH (Appendix 3. 7(b))

Appendix 3. 8 shows the surface area index (SAI) (given by the total surface area divided by the area of a completely flat surface) of the electrodes after EC at different current densities for 40 min, measured using an optical profiler. SAI of the cathode remained relatively constant at the different current densities, indicating no significant change in its effective surface area regardless of the applied current densities. In contrast, the SAI of the anode increases as EC proceeds at higher current densities but does not change much if it is raised above 10 mA/cm^2. Plateauing of the SAI above 10 mA/cm^2 was because of complete corrosion of the anode surface and similar corrosion pattern where a certain aluminium crystal facet was preferentially dissolved (Appendix 3. 9). An increase in the effective surface area of the electrode would mean lower resistance. Resistance across a conductor is inversely proportional to the surface area exposed. With increased surface area after corrosion of the aluminium electrode, total resistance decreases, bringing about lower required voltages to supply the same current according to Ohm’s law (V=IR).

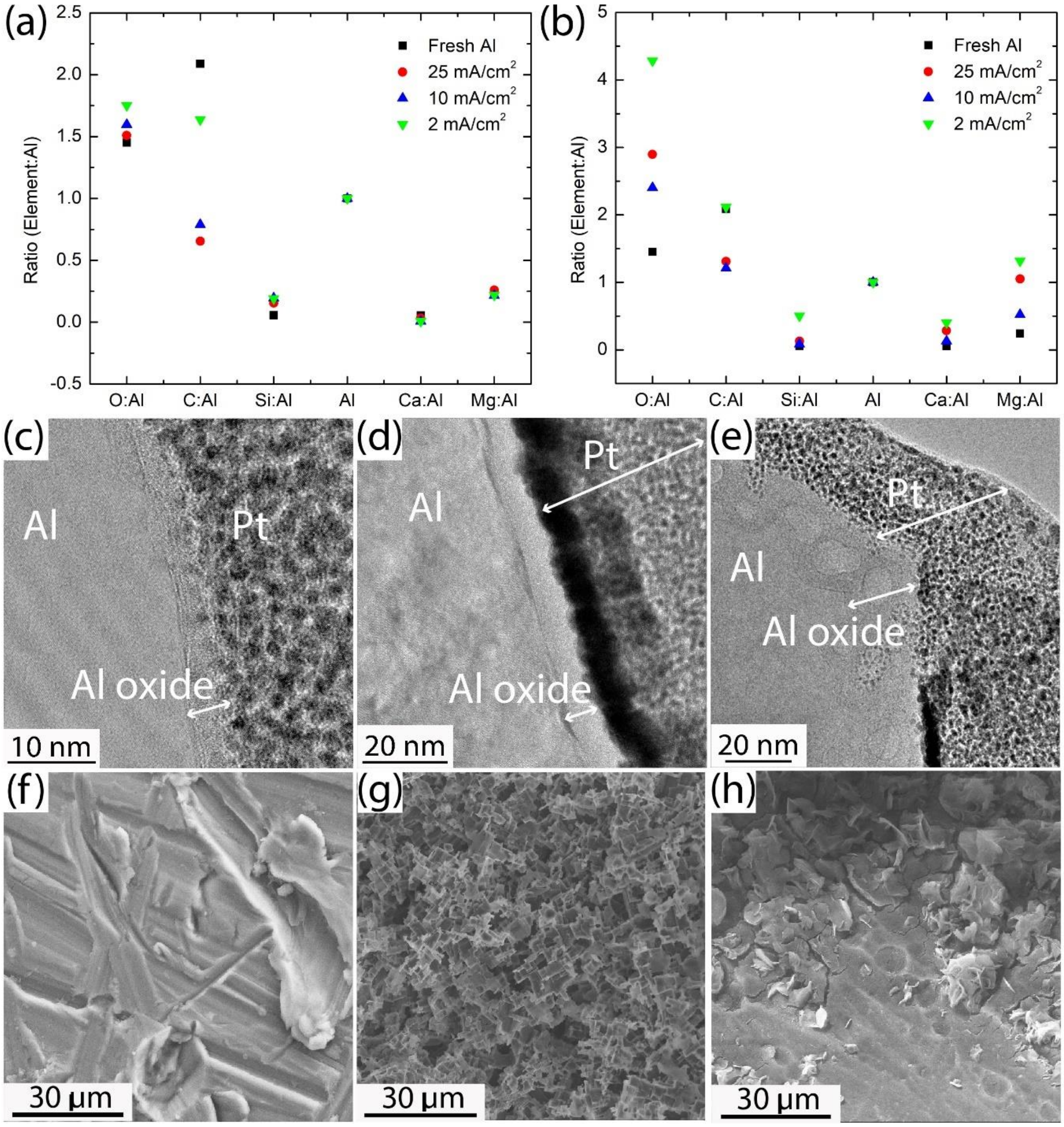

Figure 15: XPS (a) anode and (b) cathode surface atomic composition normalized against Al atomic composition. Cross-sectional TEM images of (c) fresh aluminium electrode, (d) Al anode and (e) cathode after EC at 25 mA/cm^2 for 40 min. SEM surface characterization of (f) fresh aluminiuml electrode, (g) aluminium anode and (h) cathode after EC at 25 mA/cm^2 for 40 min.

3.4.3 Electrochemical characterization during EC

High-voltage EIS measurements and Tafel plots were obtained by masking the anode or cathode to reduce their effective surface area and achieve the needed current densities with the potentiostat. Importantly, the working electrode of the potentiostat (either anode or cathode) was masked (active surface area of 2 cm^2), while the counter electrode was unmasked and had a larger surface area (55.6 cm^2). The cell potential was supplied and monitored throughout the experiments using a power supply where the current density of the working electrode was set to 15 mA/cm^2 in synthetic groundwater and a 3 mM Na_2SO_4 solution (Figure 16(a) and (b)). At 10, 20, 30 and 60 min time intervals, the power supply was disconnected, and the potentiostat was connected to obtain the EIS measurements and Tafel plots.

When the anode was used as the working electrode, the cell potential remained comparatively stable at approximately 7.3 V. From the SAI values shown in Appendix 3. 8, we know that the effective surface area of the anode increases after the application of a corroding potential. The increase in effective surface area would lower the overpotential necessary to supply a specific current. However, although the effective surface area of the anode increased, the effects were counteracted by an increase in the oxide layer thickness from 3.5 ± 0.5 nm (fresh aluminium) to 7 ± 1 nm (after EC) at the anode as shown by the TEM images in Fig 3(c),(d). Because of the balance between an energy-conserving (increase in SAI) and an energy-consuming (increase in oxide layer thickness) structural change on the anode, the overpotential needed to drive the same current throughout the experiment remained constant.

In contrast to the anode-controlled experiment, the required total cell potential in the cathode-controlled experiment dropped as the EC experiment proceeds. It is also shown in Figure 15(e), the oxide layer thickness increased from 3.5 ± 0.5 nm on a fresh aluminium electrode to around 5 ± 2 nm after EC at the cathode. Both the formation of mineral scalants and increase in oxide thickness on the cathode did not cause a rise in the required overpotential to drive the same current. This could be caused by the presence of chloride ions that induced a drop in the local pH at the cathode [171]. It is known that chloride affects aluminium dissolution by enabling pitting, which is caused by chloride's ability to penetrate through the protective Al_2O_3 layer to form soluble complexes such as $AlCl_3$ [168, 172]. A possible reaction at the cathode caused by chloride is shown by the following equation [173]:

$$AlCl_3 + 3H_2O \leftrightarrow Al(OH)_3 + HCl \qquad (23)$$

The formation of HCl increases local pH at the cathode. According to the Pourbaix diagram, the required overpotential to drive water splitting at the cathode drops at lower pH values [174]. However, the Pourbaix diagram only describes a change of -59.2 mV/pH. Changes in pH at the cathode does not completely explain the nearly 2 V drop after 1 hour of electrocoagulation. We speculate the oxide layer was in the form of gibbsite or boehmite. These hydrated forms of aluminium oxide (gibbsite and boehmite) has been shown to be more electrically conducting than the naturally occurring Al_2O_3 [175, 176], explaining the decrease in the cell potential required at the cathode over time.

To compare aluminium dissolution in a chlorine-free environment, Na_2SO_4 with the same ionic strength as synthetic groundwater (3 mM) was used to conduct EC under the same conditions (Figure 16(b)). To achieve a current density of 15 mA/cm^2 in the anode-controlled experiment, a potential of more than 40 V was necessary, which was 5 times higher than in synthetic groundwater (i.e., in the presence of Cl). Further inspection of the aluminium anode surface by SEM after EC revealed little to no dissolution of the electrode (Appendix 3. 7(a)). It is likely that the application of anodic potentials in the Na_2SO_4 solution only caused the migration of oxygen ions through the aluminium oxide layer towards aluminium to thicken the layer of electrically insulating aluminium oxide.

In the cathode-controlled experiment in Na_2SO_4, the cell potential required remained constant unlike in synthetic groundwater where the cell potential decreased. TEM images of the cathode after EC in Na_2SO_4 and in groundwater were very different (Appendix 3. 10(a) and Appendix 3. 10(b)). Instead of having circular oxide structures that extend deep into aluminium, the oxide layer was flat, similar to that observed on fresh aluminium and the anode. A TEM-EDS image shows a 2nd phase near the surface of the Al electrode composed primarily of aluminium and oxygen (Appendix 3. 10(c-f)). The difference in structure of the aluminium oxide layer could be caused by a difference in the mechanism of aluminium dissolution at the cathode in chloride-containing and chloride-free solutions. While aluminium dissolution at the cathode is mainly caused by hydrolysis in chloride-free solutions, dissolution in chloride-containing solution is partly caused by the penetration of chloride ions and formation of soluble aluminium chloride complexes.

Tafel plots were obtained for the electrodes at different time intervals of the 15 mA/cm^2 anode- and cathode-controlled EC experiment in synthetic groundwater after 60 minutes of operation (Figure 16(c) and Figure 16(d)). Over time, the corrosion potential (E_{corr}) moved to more negative values in the anode-controlled experiment (-0.6 to -0.71 V), indicating a loss in passivity [177]. This loss in passivity could be caused by pH changes at the anode as Al^{3+} ions take up hydroxide ions to create a low pH environment [178]. At the cathode, the shift of E_{corr} was more pronounced (-0.6 to -1.3 V), which could indicate a larger drop in local pH. In both cases, once the EC reaction begins, the corrosion current increases, once again indicating a weakened protective film around the aluminium electrodes.

EIS was conducted throughout the experiments in synthetic groundwater at different time intervals (0, 10, 20, 30 and 60 min) at the voltage needed to achieve 15 mA/cm^2. Nyquist plots show a single semi-circle that has a relatively constant value (Figure 16e)). A Randle's circuit was used to fit the EIS data, with Rs being the electrolyte resistance, R1 being the charge transfer resistance and CPE1 being a constant phase element. For the anode, R1 did not change over time (at approximately 190 Ω). In contrast, R1 of the cathode decreased over time, from 180 Ω to 120 Ω over 60 min (Figure 16(f)). This is likely caused by a combination of an increase in surface area due to pit formation by chloride attack, and a rise in local pH surrounding the cathode. The required overpotential to drive water splitting drops at lower pH values according to the Pourbaix diagram [174]. The constant anode R1 and the decreasing cathode R1 are in-line with the observed changes in the cell potential shown in Figure 16(a).

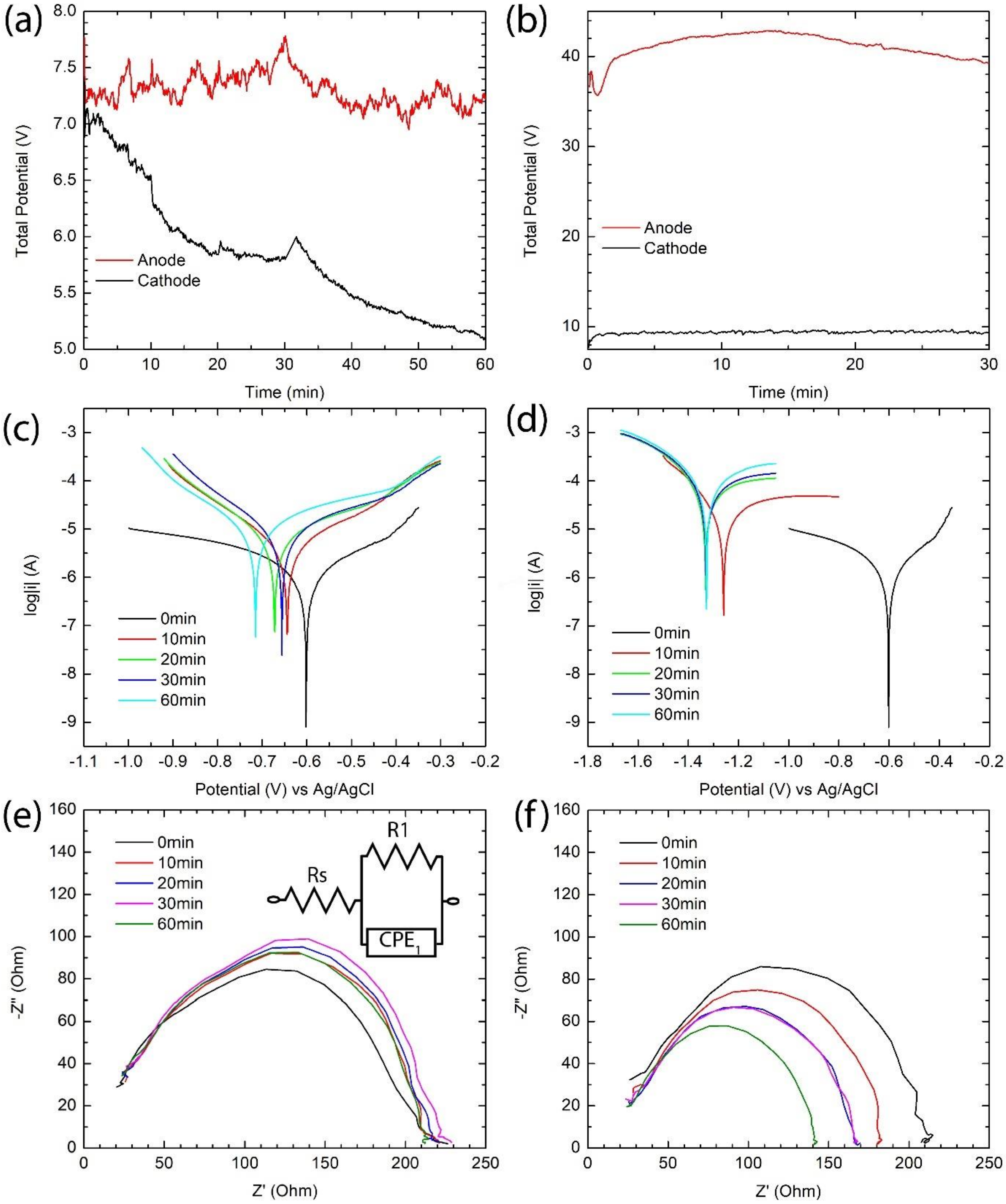

Figure 16: Overpotential changes in the electrodes in (a) synthetic groundwater and (b) 3 mM Na_2SO_4. Tafel plots of the (c) anode-controlled and (d) cathode-controlled experiments in synthetic groundwater over time at 15 mA/cm^2. EIS of the (e) anode-controlled and (f) cathode-controlled experiments in synthetic groundwater over time at 15 mA/cm^2.

3.4.4 EIS at different current densities

To further explore changes on the electrode surface during EC, EIS was conducted at different voltages to achieve a range of current densities from 0 to 15 mA/cm^2, with Nyquist plots obtained at the anode and cathode (Figure 17(a) and Figure 17(b)). The experiments were conducted starting from high current densities to the OCP (15 mA/cm^2 to 0 mA/cm^2) so that surface area changes between the different current densities would be kept to a minimum. It was observed that at lower current densities, 2 semi-circles can be seen at both the electrodes. However, with increasing current densities, the semi-circle that appears at low frequencies diminished in size and eventually disappeared above 2 mA/cm^2.

To find out the cause of the low-frequency semicircle, EIS was conducted using a rotating disc electrode (RDE) at OCP. The RDE rotates at high speeds during experiments to induce a high flux of electrolyte to the surface of the electrode and minimize the impact of mass transport. As the rotation speed increases, the thickness of the diffusion layer changes and can be approximated by the following equations [179, 180]:

$$\delta = 1.61\sqrt[3]{D_o}\frac{\sqrt[6]{v}}{\sqrt[2]{\omega}} \qquad (24)$$

$$\omega = 2\pi(rpm)/60 \qquad (25)$$

Where δ is the diffusion layer thickness, D_o is the diffusion coefficient, v is the kinematic viscosity and ω is the angular rotation rate, and rpm is rotations per minute.

Rotations speeds were adjusted from 100 rpm to 2000 rpm, corresponding to δ values between 6.8 – 1.5 µm for $AlCl_3$, assuming the diffusion coefficient of $AlCl_3$ in solution is 1.2 x 10^{-9} m^2/s [181, 182]. Figure 17(c) shows Nyquist plots conducted at OCP at 4 different rotation speeds. There were no apparent changes in the semi-circles at both high and low frequency.

This indicates that the low frequency semi-circle is not controlled by the diffusion of Al^{3+} ions through the diffusion boundary layer on the surface of the electrode. Thus, we attribute the high-frequency semi-circle observed in the Nyquist plots to charge transfer resistance (R1), and the low-frequency semi-circle to the diffusion of Al^{3+} ions or electrons through the aluminium oxide layer, (Rd). Figure 17(d) shows the equivalent circuit model used to describe the EIS results at both high voltage and at OCP. At high voltage, a simple Randles circuit that consists of the electrolyte resistance (Rs), R1 and a constant phase element (CPE_1) is used since only one semi-circle was observed [183]. At OCP, the Randles circuit is modified to include another resistor (Rd) and constant phase element (CPE_d) placed in parallel to model the second observed semi-circle at low frequency.

EIS was also conducted at 15 mA/cm^2 at different rotation speeds. There was only 1 semi-circle in the high frequency region and no obvious change in R1 at the different rotation speeds. (Figure 17(e)). Based on this observation, it is likely that diffusion of Al^{3+} ions away from the electrode surface is not a limiting factor to the aluminium dissolution rate in the conditions tested in this study. Even without the use of the RDE, we speculate that the continual movement of synthetic groundwater in the flow-through EC cell helped to reduce concentration polarization along the aluminium anode surface that prevented the formation of a thick diffusion boundary layer.

The disappearance of Rd at high current densities can be explained by the higher rate of transfer of aluminium ions to the electrolyte solution as current density increases. Since the aluminium oxide barrier layer is continually being dissolved at high current densities, Rd which is attributed to aluminium diffusion in the oxide layer disappeared. It was also noted that Rd at OCP at the anode is larger than at the cathode. From TEM images in Figure 15(d) and (e), the thickness of the oxide layer is larger at the anode than the cathode. This once again supports the claim that Rd is controlled by diffusion of Al^{3+} ions or electrons through the oxide layer.

From the EIS measurements conducted at different voltages it was determined that as the current density increased, R1 continues to decrease in magnitude (from 230 ± 15 Ω at OCP to 164 ± 4 Ω at 15 mA/cm^2) (Figure 17(a) and Figure 17(b)). The decrease in R1 as applied potential is increasingly positive on the anode and negative on the cathode is similar to the non-linear relationship between current and overpotential observed by Tafel [184], which is:

$$\eta = a + b \log i \tag{26}$$

Where η is the overpotential, i is current, and a and b are constants. The exponential relationship between η and i results in R1 (given by η/I) decreasing as the current density increases.

An explanation for the drop in R1 is that as the electrode potential is increased in the negative or positive direction, the energy level of electrons/holes in the electrode rise to a point that permit them to transfer from the electrode to the electrolyte [185]. As the electrode potential is continually raised, a larger percentage of electrons/holes [186], not necessarily linear to the applied potential, are raised to the electron transfer energy level, explaining the drop in R1 at the cathode.

Figure 17(f) shows changes in R1 values as the electrodes are polarized at increasing and then decreasing current densities. Starting from high current densities, R1 values increase as the current density decreases from left to right. However, when the current density increases again, R1 values decrease to values lower than their original point. This hysteresis could result from an increasing effective surface area at the anode, and a decreasing local pH at the cathode. When the EIS was first measured at 15 mA/cm^2 at the anode, the fresh surface of the aluminium electrode had not corroded yet. As the electrode was continually polarized to conduct EIS measurements at high current densities, the electrode surface corroded, resulting in a growing anode surface area. A larger anode surface would mean the effective current density supplied to the anode was lower the second time the same current was applied. Thus, a lower overpotential was required, resulting in a drop in R1 (given by η/i). On the other hand, the effective surface area of the cathode did not change significantly (Appendix 3. 8)). The hysteresis at the cathode can be explained by a decrease in local pH as the electrode is continually being used at high current densities. The required overpotential to drive water splitting at the cathode drops at lower pH, according to the Pourbaix diagram [174], resulting in a lower overpotential necessary to drive the same current density.

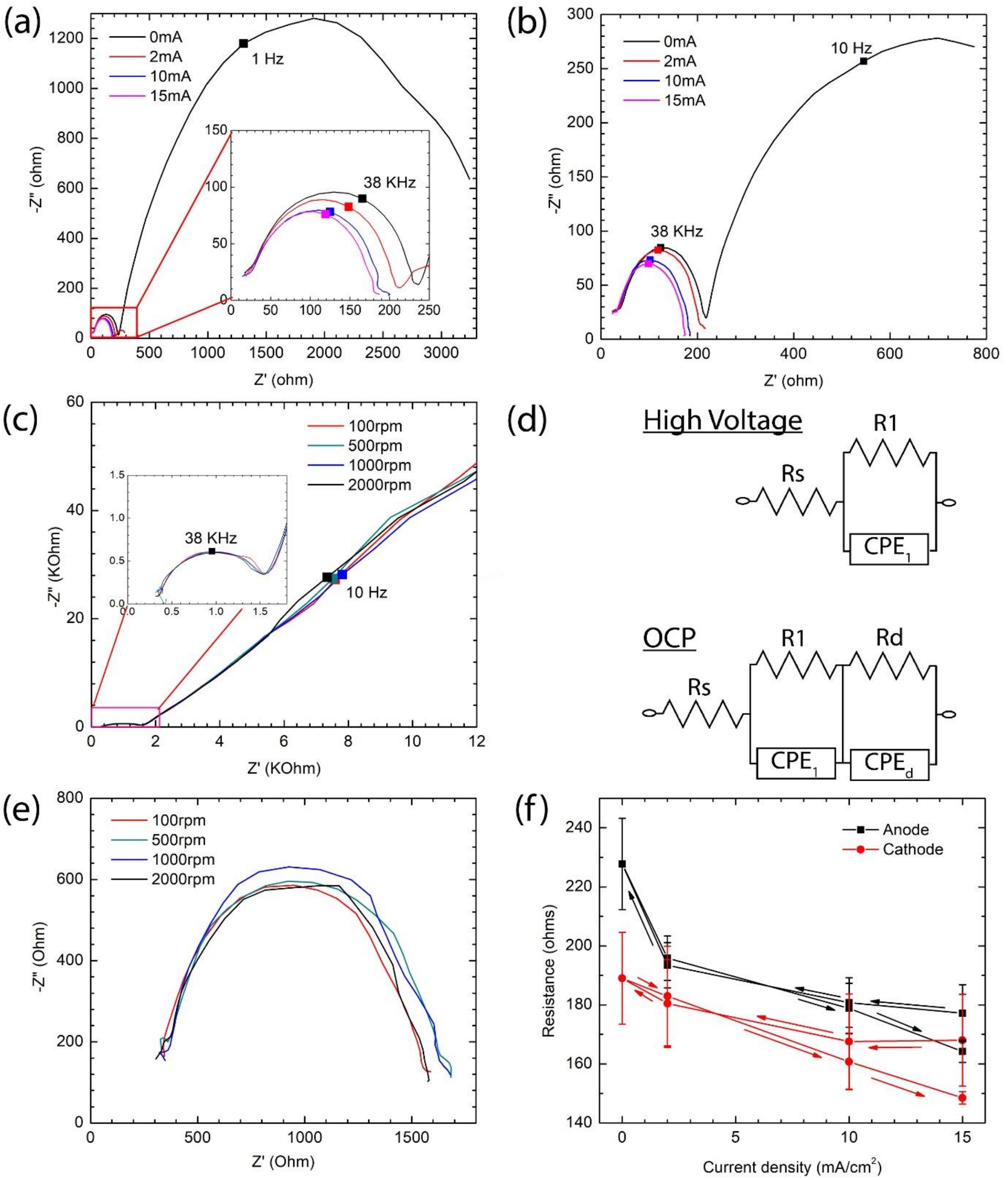

Figure 17: Nyquist plots of the Al (a) anode and (b) cathode at various current densities. (c) Nyquist plots of the Al anode at OCP using an RDE at different rotation speeds. (d) Equivalent circuit model used to fit the EIS experimental data at both high voltage and at OCP. (e) R1 values of the Al anode and cathode at various current densities. (f) Nyquist plots of the Al anode at 15 mA/cm^2 using an RDE at different rotation speeds.

3.5 Conclusion

An EC process in synthetic groundwater was explored using 5052 aluminium alloy in a flow-through cell analogous to a PFR with very short retention times from 0.73 s up to 2.1 s at current densities of 2, 10 and 25 mA/cm^2. The removal of Si reached 50 ± 4%, and hardness removal reached 11 ± 1 % when EC was operated at 25 mA/cm^2 with a retention time of 2.1 s. pH of the synthetic groundwater decreased for a maximum point of 0.6 pH, while turbidity increased with increased current density. Silica and hardness removal improved with increased current density and longer retention times. The EC reactions were allowed to proceed for 40 min or more, and electrode characterizations were done using SEM, TEM, XPS, optical profilometry and electrochemical measurements. It was shown that the most energy consuming step in the EC of synthetic groundwater is not caused by scaling at the cathode, but rather a thickened aluminium oxide film at the anode in such a set-up. At the cathode, a less electrically insulating aluminium oxide layer formed that led to a reduction in energy consumption as EC proceeds. The difference in the energy consumption trends of the two electrodes is attributed to a difference in aluminium dissolution mechanisms. While aluminium oxide formation at the anode is a direct combination of oxygen and aluminium ions, the formation of aluminium oxide at the cathode is through the dissolution of soluble aluminium chloride complexes. High mass transfer rates of the flow-through cell prevented the formation of thick amorphous $Al(OH)_3$ on the electrodes that could lead to higher energy consumption. A thickened oxide layer on the aluminium anode was however not preventable but did not cause a rise in the overpotential necessary to drive the required current density.

3.6 Appendix

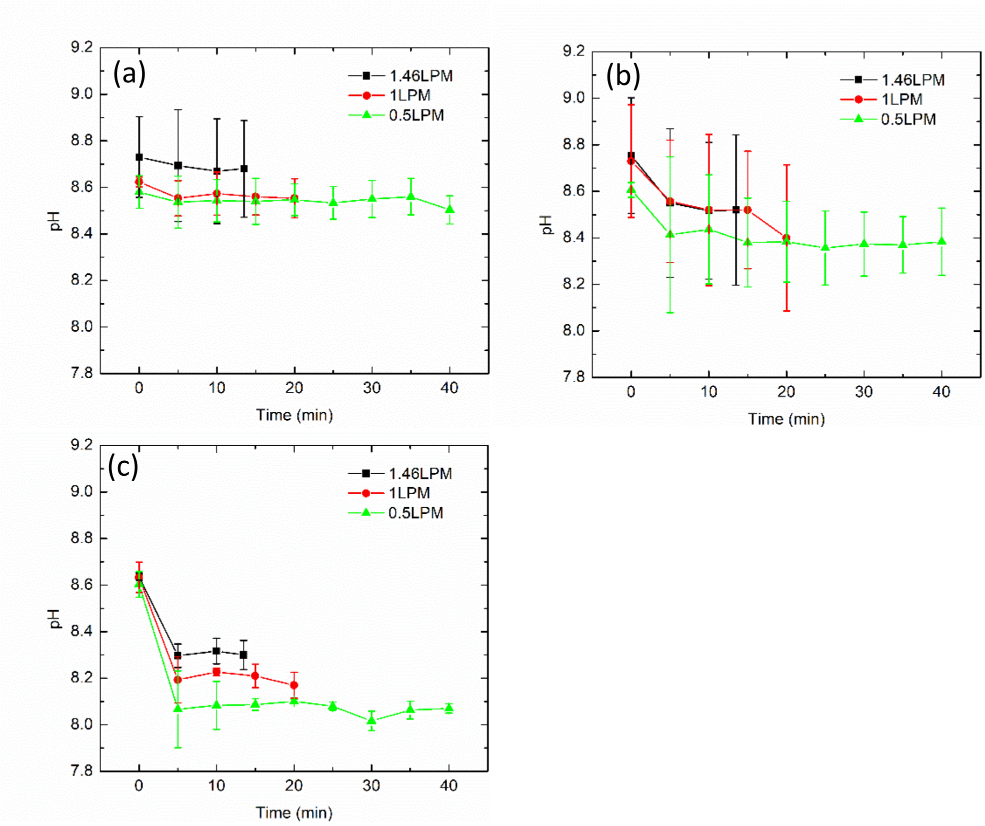

Appendix 3. 1:pH changes in synthetic groundwater at (a) 2mA/cm2, (b) 10mA/cm2 and (c) 25mA/cm2.

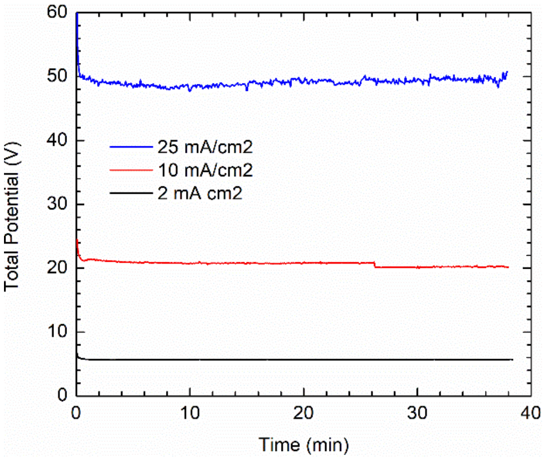

Appendix 3. 2: Overpotential required to drive 2, 10 and 25 mA/cm^2 over 38 min of EC in synthetic groundwater at a flow rate of 0.5 LPM using a once-through EC cell.

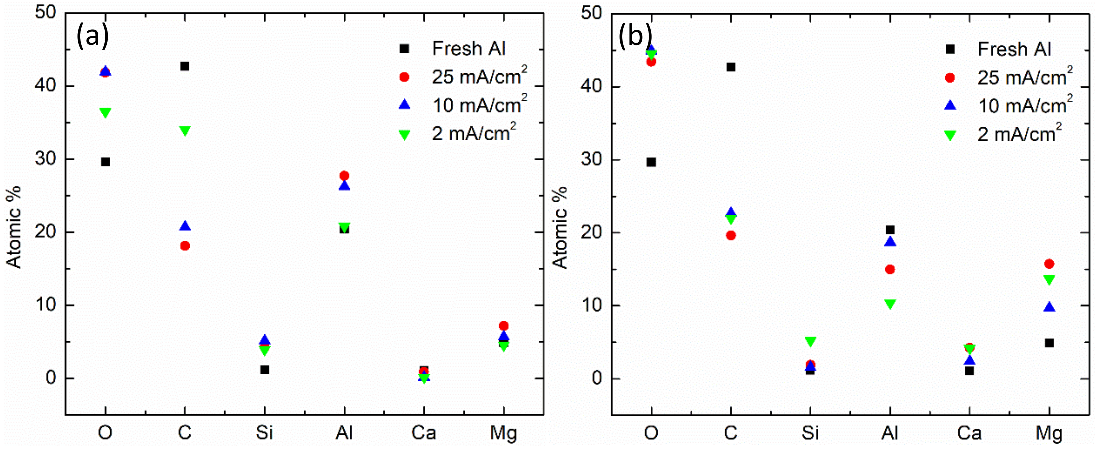

Appendix 3. 3: XPS surface composition of Al (a) anode and (b) cathode after EC at 0.5 LPM for 38 min in synthetic groundwater.

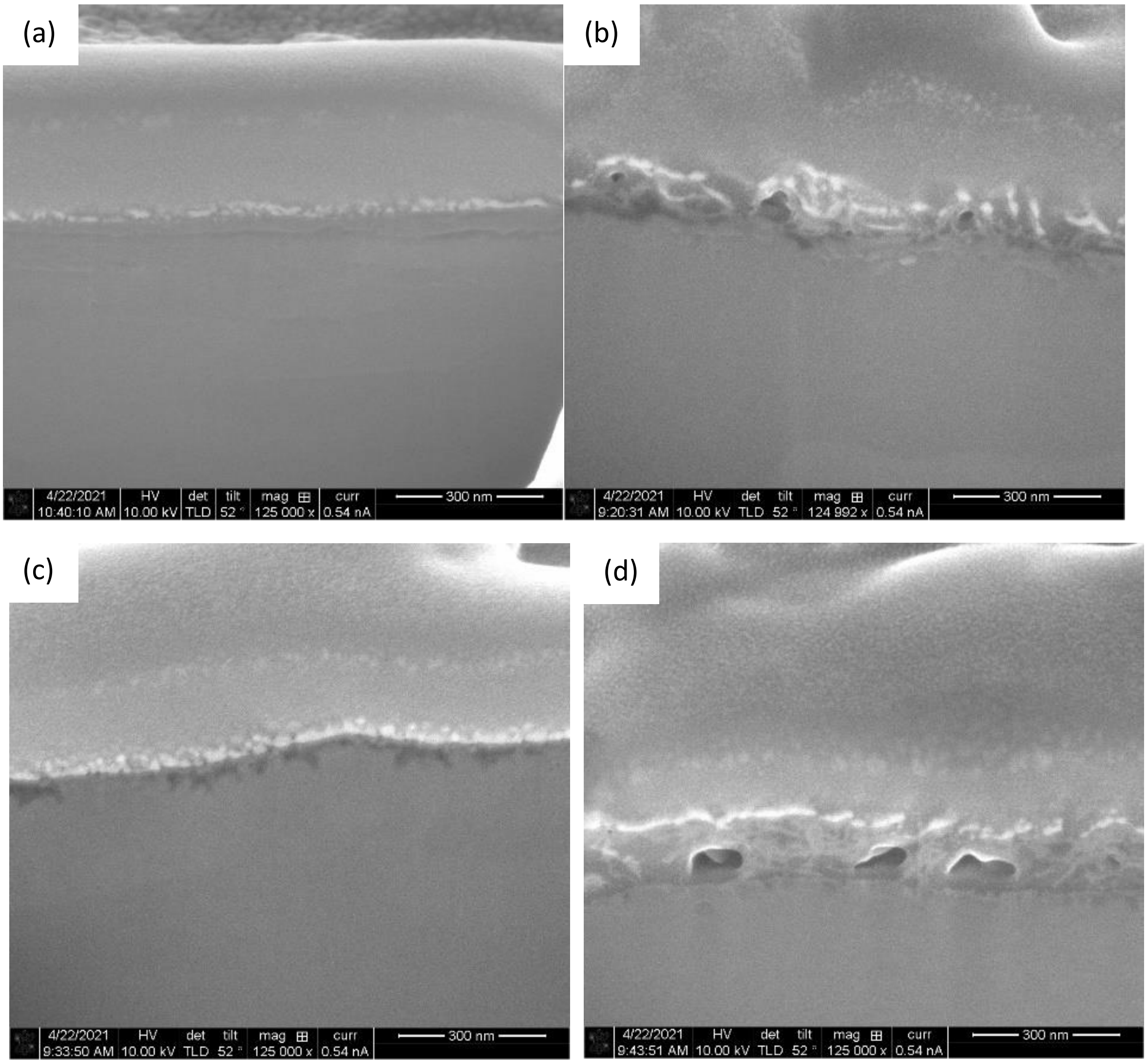

Appendix 3. 4: SEM cross-sectional image of (a) fresh aluminium electrode, (b) cathode after subjecting to current densities of 2mA/cm2, (c) 10 mA/cm2 and (d) 25 mA/cm2 for 38 min in synthetic groundwater, obtained through ion beam etching.

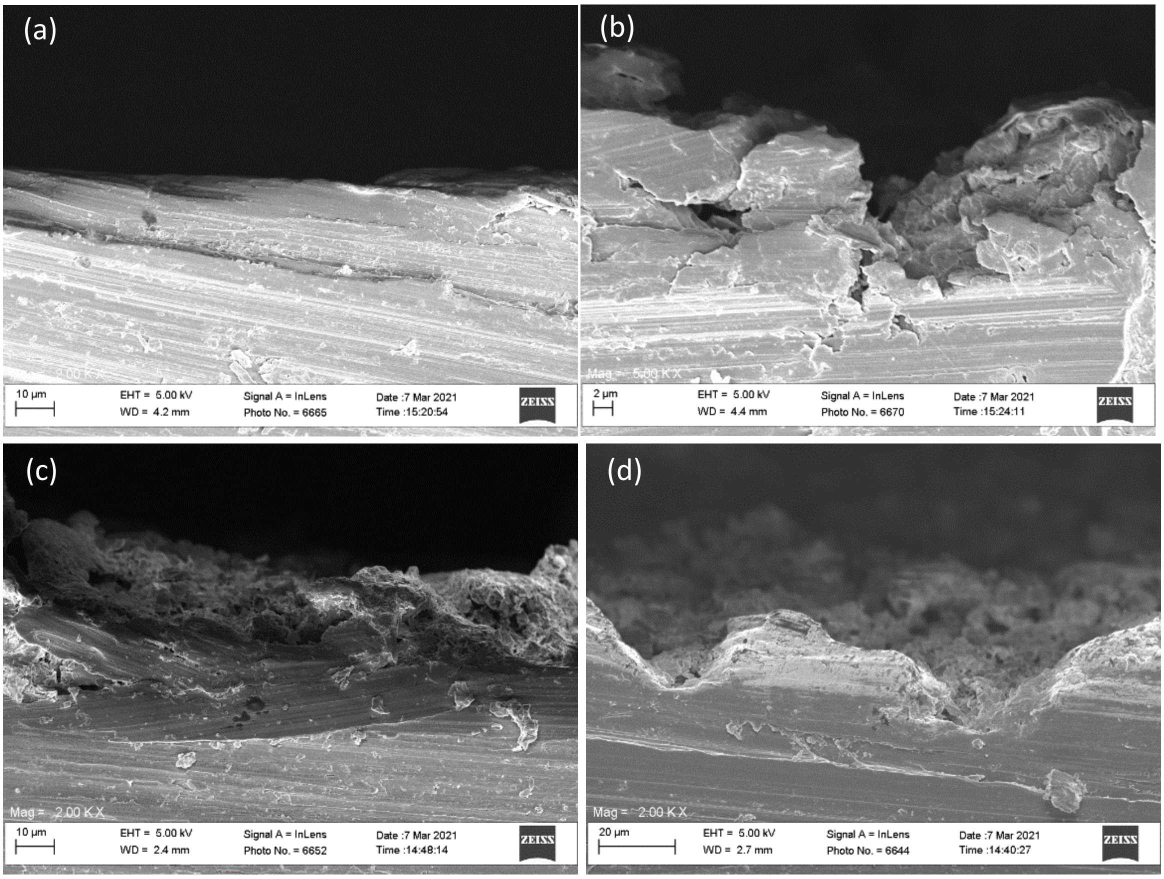

Appendix 3.5: SEM cross-sectional images of (a) fresh aluminium electrode, and anode after subjecting to current densities of (b) 2mA/cm^2, (c) 10 mA/cm^2 and (d) 25 mA/cm^2 for 38 min in synthetic groundwater, obtained through abrasion with sandpaper.

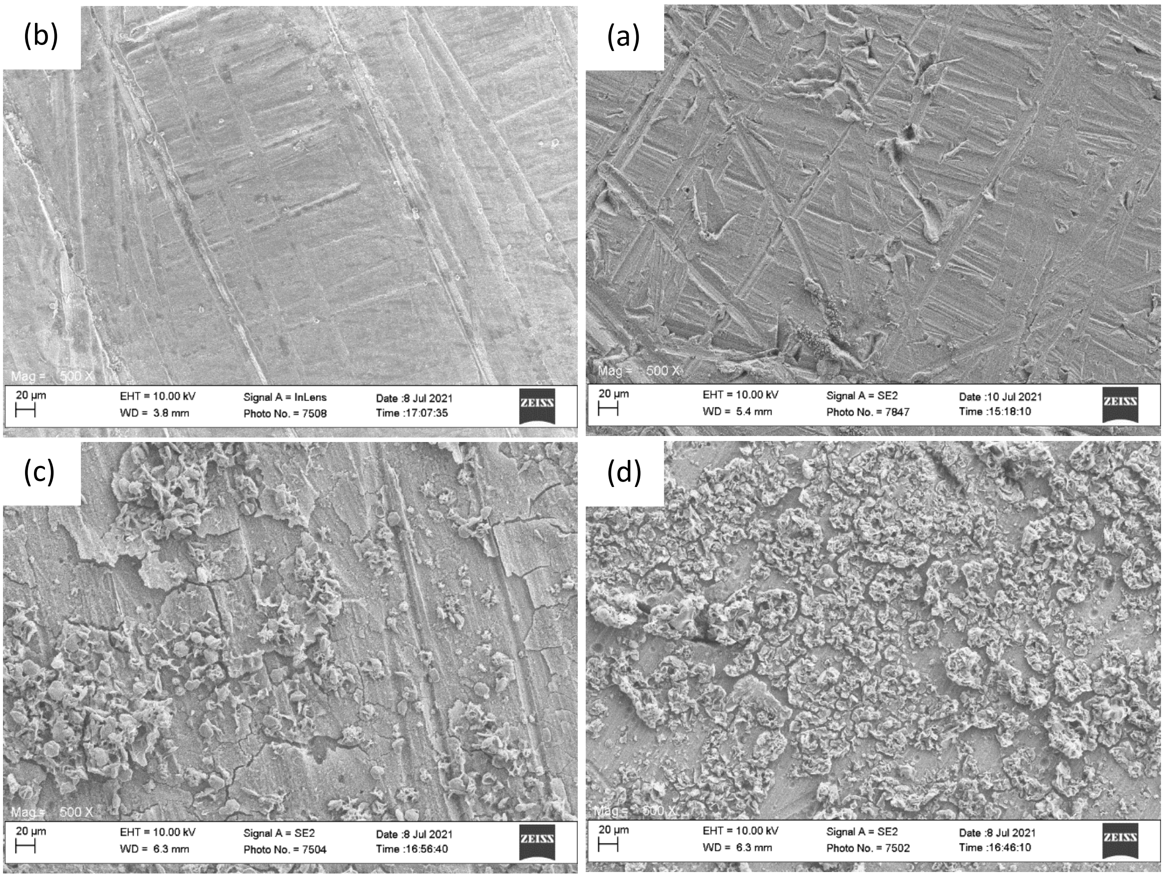

Appendix 3. 6: SEM images of (a) fresh aluminium electrode (b) cathode after EC at 2 mA/cm^2, (c) 10 mA/cm^2 and (d) 25 mA/cm2 for 38 min in synthetic groundwater.

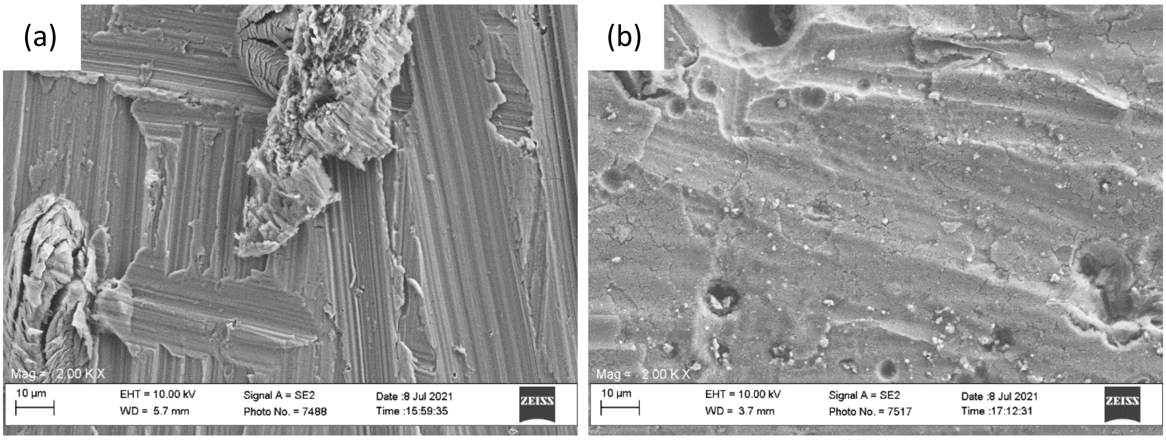

Appendix 3. 7: SEM image of the (a) anode and (b) cathode after EC at 15 mA/cm2 38 min in Na2SO4 solution.

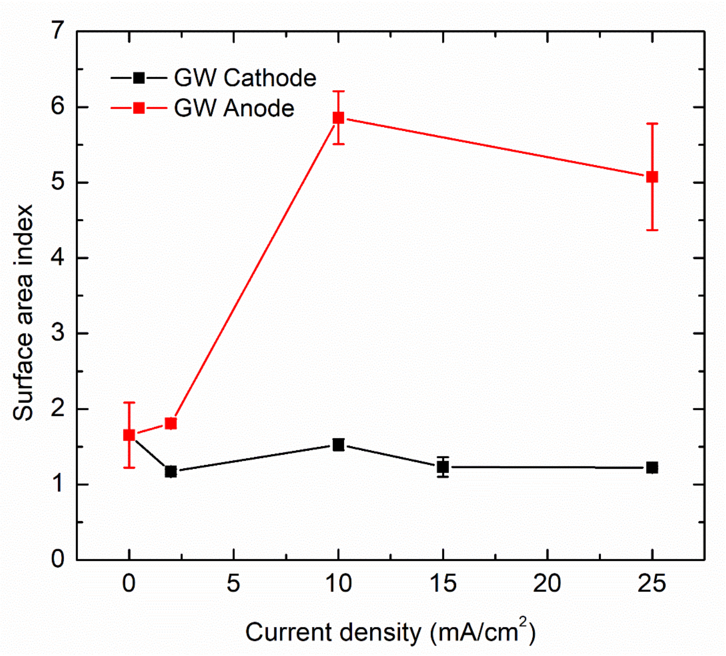

Appendix 3. 8: Surface area index of aluminium electrode surface measured by an optical profiler

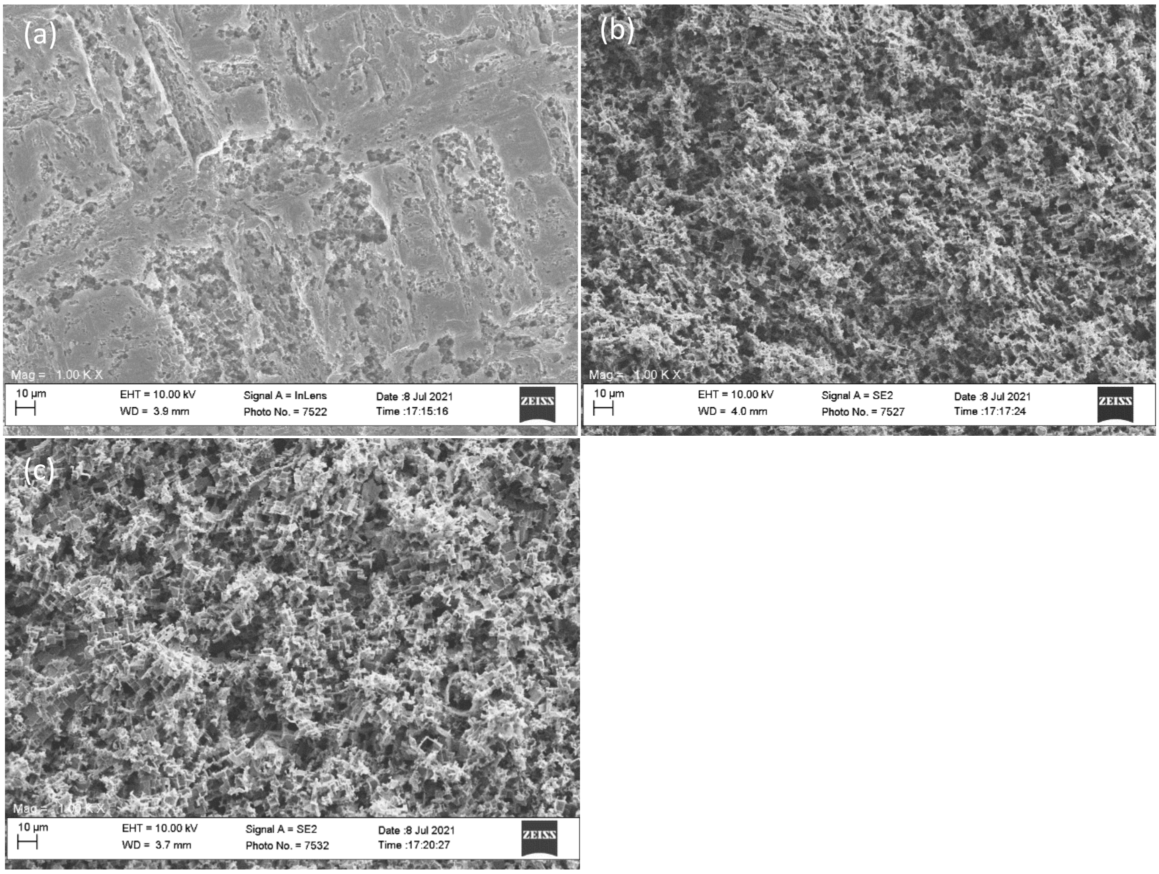

Appendix 3. 9: SEM images of anode after EC at (a) 2 mA/cm^2 (b) 10 mA/cm2 and (c) 25 mA/cm^2 for 40 min in synthetic groundwater

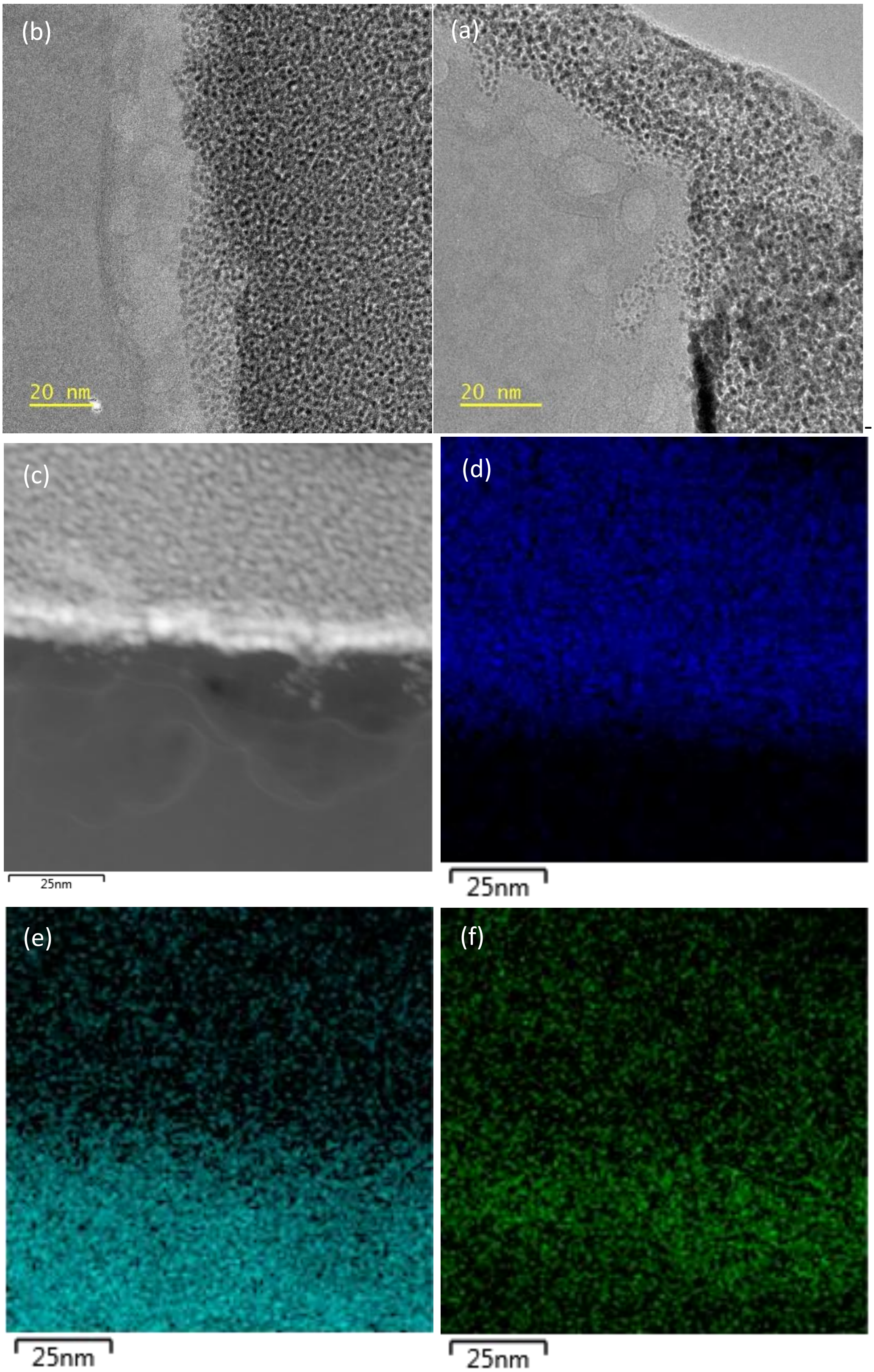

Appendix 3. 10: TEM images of cathode after EC for 40 min at (a) 25 mA/cm^2 in synthetic groundwater and (b) 15 mA/cm^2 in 3mM Na_2SO_4 solution. (c) STEM image and STEM-EDX maps of (d) platinum, (e) aluminium and (f) oxygen for cathode after EC at 25 mA/cm^2 in synthetic groundwater for 40 min.

Chapter 4: Electropolymerization of aromatic monomers for salt-rejecting membranes

4.1 Abstract

Electropolymerization of aromatic moieties similar to state-of-the-art polyamide RO membranes have allowed the fabrication of salt-rejecting membranes capable of up to 84±2% NaCl rejection. Multiple monomers in various electropolymerizing permutations have been explored, and the electropolymerization of a mixture of resorcinol and trimesic acid resulted in membranes with the highest salt rejection capability owing to a dense structure formed with reasonable flexibility to withstand high pressures in a cross-flow module. An electropolymerization mixture of phloroglucinol with and without trimesic acid did not result in significantly different chemical structures, possibly due to a much lower O-H bond dissociation energy in phloroglucinol compared to trimesic acid. However, the resulting polyphloroglucinol membrane was too brittle to withstand compaction during salt rejection tests as a result of a rigid highly cross-linked structure formed.

4.2 Introduction

To date, reverse osmosis (RO) membranes is one of the most promising membrane separation processes for producing drinking water due to its energy efficiency and ability for high salt rejection together with high water flux. Commonly, these membranes are made from the interfacial polymerization of trimesoyl chloride (TMC) in an organic phase, and 1,3-phenylenediamine (MPD) in water. A non-porous dense thin film is created this way.

Separation is achieved as a result of a difference in dissolution and diffusion rate of the different molecules through the polyamide layer.

One of the most common configurations for polyamide RO membranes is a spiral wound flat sheet thin film composite (TFC). A TFC contains 3 layers of materials: a non-woven fabric layer for mechanical strength, subsequently a microporous support layer, and finally the active layer (polyamide) where separation takes place. The spiral wound configuration is the cheapest to make from flat sheet TFC membranes [187]. It also grants a high specific membrane surface area, simple scale-up, and low replacement costs.

During interfacial polymerization, an organic solvent is often required for the dissolution of TMC. Organic solvents are recognized for their neurotoxicity [188, 189] and low flash points where they can evaporate into explosive mists [190, 191], posing an occupational health risk [192-195]. A recent explosion involving organic solvents at a waste-management center in Germany left 2 dead and 31 injured [196]. In a separate case study, a man was diagnosed with organic solvent-induced chronic toxic encephalopathy after exposure to mixed solvents for 15 years [197]. As such, alternative polymerization techniques that reduces the use of toxic solvents could be beneficial for both the environment and industries.

Electropolymerization as a means to fabricate salt rejecting membranes is a potential technique for salt-rejecting membrane fabrication. Further, it is possible to get rid of leftover aromatic monomers in the polymerization solution after membrane fabrication through electrochemical treatment methods [198]. The generally accepted mechanism for electropolymerization concerns the formation of a cationic radical by monomer oxidation on the conducting surface. Polymer propagation then involves either radical coupling, or reaction of the radical with a neutral molecule. Electropolymerization can be conducted using a variety of electrochemical techniques, including potentiostatic, galvanostatic and potentiodynamic methods. Control of electropolymerized film thickness can easily be achieved by changing the polymerization time or applied potential, while the electropolymerization of non-conducting films is a self-limiting reaction where polymerization stops when an insulating film is formed between the conductive substrate and the polymerizing solution. Some conductive polymers include polyaniline and polypyrrole. Non-electrically conducting polymers include derivatives of polyphenol, such as polyresorcinol and poly(o-aminophenol).

Formation of electropolymerized films has been achieved for water purification and gas separation applications. A microporous polymer membrane electropolymerized using 2,2’,7,7’-tetra(carbazol-9-yl)-9,9’-spirobifluorene inside a CNT scaffold was recently reported. The resulting membrane had a uniform pore size of around 1 nm and accomplished fast solvent transport exceptional molecular sieving [199]. Flexible electropolymerized polythiophene membranes have also been reported for H_2 gas separation where the membrane was free-standing. The membranes had excellent gas separation properties above the Roberson upper bound value, and was stable over 7 days under high temperature and acidic conditions [200]. Poly(o-aminophenol) has been synthesized by electrooxidation on a platinum electrode which functioned as a perselective membrane for glucose oxidase biosensor [201]. A slight tweak in the electrosynthesis condition of the membrane resulted in improved sensor response.

As far as our knowledge, electropolymerization of salt-rejecting membranes has not been reported. In this study, 3 electrically active monomers similar to the structure of TMC and MPD (commonly used in the fabrication of RO membranes) are used to electropolymerize salt-rejecting films. A combination of resorcinol, phloroglucinol and trimesic acid were electropolymerized in water to form 4 types of membrane structure and tested for their salt-rejecting properties. TMC was also used in an attempt to improve the salt-rejection properties of these films.

4.3 Materials and methods

4.4 Materials

Single-wall Carbon nanotubes were purchased from cheaptubes (VT, USA). Resorcinol, trimesic acid, phloroglucinol, sodium chloride, dodecylbenzenesulfonic acid and trimesoyl chloride were purchased from Sigma Aldrich (MO, USA). Hexane, triethylamine and sodium perchlorate were purchased from Alfa Aesar (MA, USA). Polysulfone ultra-filtration membranes were kindly provided by Nanostone Water (MA, USA). DI water used in the experiments were provided in-house.

4.5 Methods

4.5.1 Conductive membrane support fabrication

SWCNTs were suspended in deionized water with 1% w/w dodecylbenzenesulfonic acid by using a sonication probe for 30 min to make a 0.1 g/L CNT suspension.[202] The resulting suspension was centrifuged at 14,000 rcf for 45 min. 15 mL of the prepared CNT suspension was then pressure-deposited at 60 PSI onto a 20 kDa polysulfone UF membrane support.

4.5.2 Electropolymerization – polyresorcinol and polyphloroglucinol

Electropolymerization was carried out using a 3-electrode cell. The reference electrodes was Ag/AgCl in 3M KCl saturated with Ag^+. The counter electrode was a stainless steel mesh, and the working electrode was a conductive membrane deposited with SWCNT. To emulate the conditions in state-of-the-art RO membrane formation, 2% w/w resorcinol or phloroglucinol were used for electropolymerization with and without 0.15% w/w trimesic acid. 0.1 M sodium perchlorate was used as the supporting electrolyte. Polyresorcinol and polyphloroglucinol were electropolymerized at 0.6 V and 0.8 V vs Ag/AgCl respectively for 17h.

4.5.3 Active layer fabrication – TP

0.15% w/w trimesic acid, 2% w/w phloroglucinol and 0.1 M sodium perchlorate were dissolved in DI water. The resulting mixture was poured onto the conductive membrane support. 0.8 V vs Ag/AgCl was applied to the membrane for 17 h. The membrane was washed with DI water and allowed to dry.

4.5.4 Active layer fabrication – TRT

0.15% w/w trimesic acid, 2% w/w resorcinol and 0.1 M sodium perchlorate were dissolved in DI water. The resulting mixture was poured onto the conductive membrane support. 0.6 V vs Ag/AgCl was applied to the membrane for 17 h. The membrane was washed with DI water. Next, 0.3 g of trimesic acid and 2.8 g of sodium perchlorate was added to 200 mL of DI water. The resulting mixture was then poured onto the membrane and 1.0 V vs Ag/AgCl was applied for 17 h. The membrane was washed with DI water and allowed to dry.

4.5.5 Active layer fabrication – TRTMC

0.15% w/w of trimesic acid, 2% w/w resorcinol and 0.1 M sodium perchlorate were dissolved in DI water. The resulting mixture was poured onto the conductive membrane support and 0.6 V vs Ag/AgCl was applied to the membrane for 17 h. The membrane was washed with DI water. Next, the membrane was soaked in 50 mL hexane containing 2% v/v TEA for 1 minute, and a 150 mL mixture of 0.2% w/w TMC dissolved in hexane was poured over the membrane mixture. After 30 seconds, the membrane was washed with hexane and allowed to dry.

4.5.6 Salt rejection test

Fabricated membranes were tested in a cross-flow filtration module capable of housing electroactive membranes, which is described in detail in previous publications.[203, 204] The flat sheet membrane module had a feed channel with the dimensions 100 mm × 40 mm × 3.80 mm. The cross-flow filtration system was operated at constant pressure of 17 bar. Prior to filtration tests, membranes were compressed at 17 bar with DI water until a stable flux was observed. 2000 ppm sodium chloride solution was used as the feed solution for salt rejection tests. Conductivities of the feed and permeate were checked using a conductivity probe to obtain the salt rejection results.

4.5.7 Membrane characterization

Chemical bonds on the membrane were characterized using Fourier transform infrared spectroscopy (FTIR) operated in the attenuated total reflectance mode (Thermo Scientific FTIR iS10 Smart iTR Basic, Mandison, WI), with a Ge prism as an internal reflection element.

Surface morphology was characterized using atomic force microscopy (AFM) (Bruker Dimension FastScan Scanning Probe Microscope, Santa Barbara, CA). AFM images were obtained using ScanAsyst-Air and probes (Camarillo, CA).

The chemical composition of the membrane's surface was determined using X-ray photon spectroscopy (XPS) (Kratos Axis Ultra DLD spectrometer equipped with a monochromatic Al Kα X-ray source). High-resolution spectra were calibrated using carbon tape (Ted Pella) with a known C1s binding energy of 284.6 eV. Raw data were processed using CasaXPS software (version 2.3.19).

Polymer wt% of the electropolymerized film was checked using thermogravimetric analysis (TGA). In an argon gas atmosphere, the temperature was ramped from 20^{o}C to 100^{o}C at 5^{o}C per minute and allowed to dry for 30 minutes before continuing to ramp up the temperature to 900^{o}C at 5^{o}C per minute. The samples for TGA analysis were prepared on glass substrates coated with SWCNT and electropolymerized using the same method as above. The prepared polymer films were scraped off the glass substrate for TGA analysis.

4.4 Results and Discussion

4.4.1 Fabrication

Cyclic Polarization Measurements

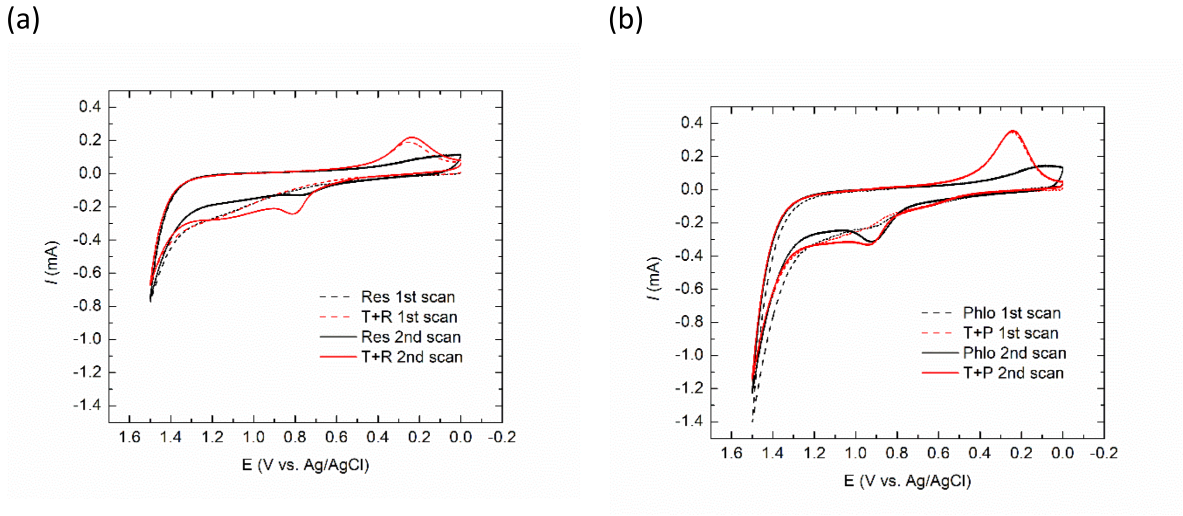

Figure 18: Cyclic voltammetry of (a) resorcinol and (b) phloroglucinol with and without the addition of trimesic acid in the polymerizing solution.

Electropolymerization depends on the oxidation of monomers onto a conducting substrate to form polymers. Cyclic voltammograms of phloroglucinol, resorcinol with and without trimesic acid are shown in Figure 18. An oxidation peak was observed at 0.78 V and 0.93 V vs Ag/AgCl for resorcinol and phloroglucinol respectively. With the addition of trimesic acid, a reduction peak was observed at 0.25 V, and the oxidation peaks of resorcinol and phloroglucinol shifted to higher potentials at 0.814 V and 0.940 V, respectively. The reduction peak at 0.25 V is attributed to the reduction of an oxide layer when the Pt wire was polarized to 1.5 V vs Ag/AgCl in the anodic sweep. It was also observed that the addition of trimesic acid resulted in a higher oxidation current for resorcinol polymerization.

It was previously reported that the adherence of resorcinol films start with the formation of an oxide film on a conductive substrate [205], explaining the absence of an oxidation peak on the first anodic sweep for both resorcinol and phloroglucinol. The appearance of an oxide film after the anodic sweep to 1.5 V allowed the oxidation of resorcinol and phloroglucinol onto the Pt wire thereafter. The presence of trimesic acid increased platinum oxidation rates when potential was swept to 1.5 V, evident from the increase in the reduction peak current density (0.25 V) after its addition. The peak oxidation current density for resorcinol increased by around 90%, while that of phloroglucinol did not change significantly.

During oxidative polymerization, phenolic compounds propagate through free radicals [206-209]. It is generally accepted that the free radical scavenging ability of phenolics is impacted by the number of -OH substituents present, with more -OH substituents leading to a higher reactivity due to higher hydrogen atom donating ability [210-212]. Thus, phloroglucinol has a higher reactivity than resorcinol. The lack of improvement in oxidation peak current density after the addition of trimesic acid to the phloroglucinol electropolymerization solution could be due to the quick formation of an insulating polymer layer that prevents further increase in the peak oxidation current as a result of diffusion limitations.

SWCNT originally contains a large amount of oxygen on its surface due to carboxylic and hydroxyl groups. Thus, formation of an oxide layer was not necessary before an electropolymerized layer could be formed. Direct oxidation of phloroglucinol and resorcinol was formed through the application of an oxidizing potential on SWNT. Since these films were nonconductive, electropolymerization was self-limiting when a sufficiently thick film forms. Electropolymerization was allowed to carry out for 17h.

4.4.2 Characterization

Membrane chemical structure

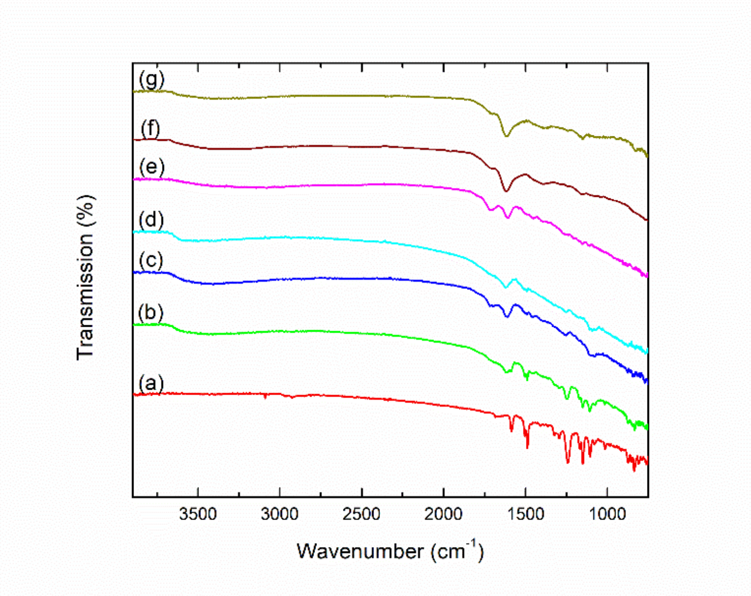

Figure 19: FTIR of (a) SWCNT on PS35, electropolymerized (b) resorcinol, (c) TR, (d) TRT, (e) TRTMC, (f) phloroglucinol and (g) TP on SWCNT with PS35 as support.

Table 10: XPS composition of carbon and oxygen of the different electropolymerized materials.

MEMBRANE	C:O	ORGANIC O=C	ORGANIC O-C
SWCNT	**57.82**	**69.75**	**30.25**
POLYRESORCINOL	**4.07**	**11.65**	**88.35**
TR	**3.45**	**30.41**	**69.59**
TRT	**3.40**	**19.61**	**80.39**
TRTMC	**3.81**	**50.03**	**49.97**
POLYPHLOROGLUCINOL	**2.46**	**22.04**	**77.96**
TP	**2.53**	**21.91**	**78.03**

Figure 19 shows the FTIR spectrum of the fabricated membranes and Table 10 shows the amount of carbon and oxygen detected, and the deconvoluted components of oxygen.

On a membrane coated with pure SWNT, C:O ratio detected by XPS was 58. After electropolymerization, a large increase in the amount of Oxygen reduced the C:O ratios to values ranging from 2.5 to 4. This indicates coverage of SWNT by the different polymers. C:O ratio decreases as the number of oxygen atoms increases on the electropolymerizing monomer. High resolution O 1s peak was deconvoluted into two significant peaks at ~533 eV (organic O-C groups) and ~531.5 eV (organic O=C groups such as ketone and carbonyl).

The FTIR spectrum of SWCNT on PS35 contains SO_2 peaks of PS35 at 1490 and 1500 cm^{-1} (Figure 19(a)). The layer of deposited SWCNT was not thick enough to block FTIR signals from reaching PS35 underneath.

Upon electropolymerization with resorcinol (Figure 19(b)), the peak at 1330 to 1300 cm^{-1} attributed to S=O stretching decreased in size, indicating the successful coating of a resorcinol layer on SWNT. The film was however not thick enough to completely cover the PS35 support underneath.

The addition of trimesic acid to the electropolymerization mixture resulted in the formation of a thicker electropolymerized film (Figure 19(c)). Transmission peaks of polysulfone could no longer be detected at 1330 and 1300 cm^{-1}. The appearance of ester O=C peak at 1720 cm^{-1} indicates the participation of trimesic acid in the electropolymerization of T+R to form ester bonds. The peak at 1070 and 1100 cm^{-1} indicates the formation of ether C-O bonds [213]. The peak at 3600 cm^{-1} indicates the presence of free hydroxyl groups.

Previously, it was reported a chlorine resistant RO membrane was made of polyester from layer-by-layer interfacial polymerization of 3,5-dihydroxybenzoic acid and TMC. [214]

Residual OH groups were capped with isophthaloyl dichloride to prevent reaction with chlorine, and the fabricated membrane exhibited high salt rejection properties as high as 99.4%.

In an attempt to end-cap the free hydroxyl groups, trimesic acid was used as a final electropolymerized layer on top of T+R (Figure 19(d)). After electropolymerization, the C=O peak at 1712 cm^{-1} was no longer detected. Instead of acting as a capping monomer for free hydroxyl groups in the T+R film formed, trimesic acid acted as an oxidizing agent for the oxidation of ester bonds in T+R film to form free carboxylic acid and alcohol. The drop in C:O ratio detected by XPS after electrooxidation with trimesic acid for the second time, supports the occurrence of de-esterification reaction. During de-esterification, H_2O molecules are incorporated into the TRT film. In addition, the percentage of O-C bonds increased by 10%, also pointing towards de-esterization.

Figure 19 (e) shows the FTIR spectrum of TRTMC. A layer of TMC was added to the T+R film to end-cap free hydroxyl groups into ester bonds. A reduction in alcohol OH stretch peak at 3600cm^{-1} reduced in size compared to T+R (Figure 19(c)) after adding the layer of TMC [215]. Ester C=O peak at 1720 cm^{-1} was also apparent. Additionally, the percentage of O=C groups increased from 30% to 50% after the addition of TMC. This shows successful condensation reaction between free hydroxyl groups and TMC.

The FTIR spectrums of pure phloroglucinol film and TP contains one C-O peak at 1613 cm^{-1}. There is also an ester C-O peak at 1150 cm^{-1}, indicating the presence of ester bonds. The addition of trimesic acid to phloroglucinol during electropolymerization did not yield a significantly different film chemistry from if only phloroglucinol were used. Similar to FTIR results, XPS did not detect a significantly different surface composition of TP and polyphloroglucinol film structures. The C:O ratio as well as the percentage of O=C and O-C groups deconvoluted from the oxygen peaks of polyphloroglucinol and TP were very similar. This could be because trimesic acid did not take part in the electropolymerization of TP films. The presence of 3 electron-withdrawing -COOH groups on trimesic acid brought about a much higher O-H bond dissociation energy than in phloroglucinol containing 3 electron-donating -OH groups. O-H bond dissociation is crucial in the formation of phenoxium radical during electropolymerization [216]. When trimesic acid and phloroglucinol monomers were mixed, phloroglucinol was preferentially electropolymerized onto the conducting substrate.

SEM

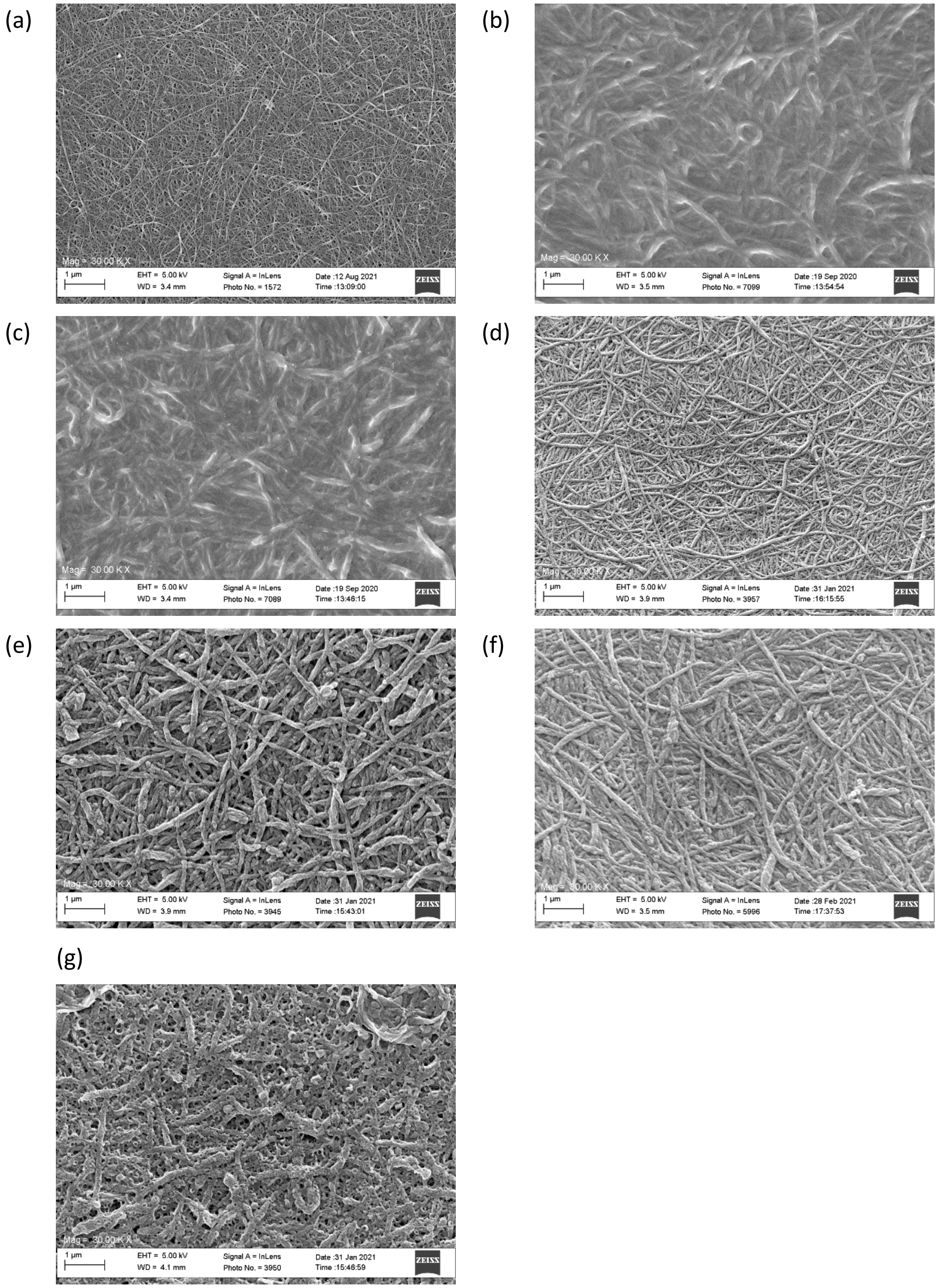

Figure 20: Electropolymerized films of (A) phloroglucinol, (C) phloroglucinol and trimesic acid, (D) resorcinol, and (E) resorcinol and trimesic acid (F) TRT (G) TRTMC

SEM figures of the electropolymerized films are shown in Figure 20. A very dense and smooth polymer layer was electropolymerized onto SWCNT by both phloroglucinol a mixture of trimesic acid and phlroglucinol. Nearly no pores could be found on the polymer, indicating a high degree of cross-linking and a very thick polymer layer.

For the other monomers on the other hand, distinct strands of SWCNT could still be distinguished under SEM after electropolymerization, but with increased widths. Instead of forming a film of polymers on the percolated SWCNT network underneath, electropolymerization occurred around each individual strand of SWCNT and formed a polymer layer surrounding the strands. SWCNT had a tube width of around 0.03 ± 0.01 µm before electropolymerization, and increased to 0.07 ± 0.02 µm for polyresorcinol, 0.14 ± 0.06 µm for T+R, 0.11 ± 0.03 µm for TRT, and 0.18 ± 0.04 µm for TRTMC.

Similar to the FTIR results, polyresorcinol film thickness was the lowest. The width of SWCNT was the smallest after electropolymerization with resorcinol compared to other combinations of monomers. The width of SWCNT after electropolymerization would correspond to the thickness of the electropolymerized film, assuming electropolymerization was uniform around SWCNT. This explains detection of PS35 sulfone groups (supporting membrane) by FTIR after electropolymerization. There is a slight decrease in SWCNT width from 0.14 ± 0.06 µm in T+R to 0.11 ± 0.03 µm after further oxidation with trimesic acid (TRT). However, taking standard deviation into consideration, the decrease in SWCNT width was not significant. SWCNT width with TRTMC was the highest. Its surface morphology looks rougher than the polymer films formed via only electropolymerization. The reaction between TMC and free hydroxyl groups on T+R film is a vigorous condensation reaction that releases H_2O

and HCl similar to formation of state-of-the-art polyamide RO membranes. The release of H_2O and HCl molecules cause folds to form on polyamide RO membranes. However, in the case of adding TMC to a layer of pre-formed polymer containing free hydroxyl groups, instead of the formation of folds, round holes were formed. When TMC was added to the T+R film that is not fully cross-linked, TMC molecules penetrate through the polymer chains to the lower layers close to SWCNT. Since T+R is covalently attached to SWCNT, there is no space to expand when H_2O and HCl molecules were released. The round holes observed on TRTMC were formed when trapped H_2O and HCl breaks through the polymer surface.

Salt rejection

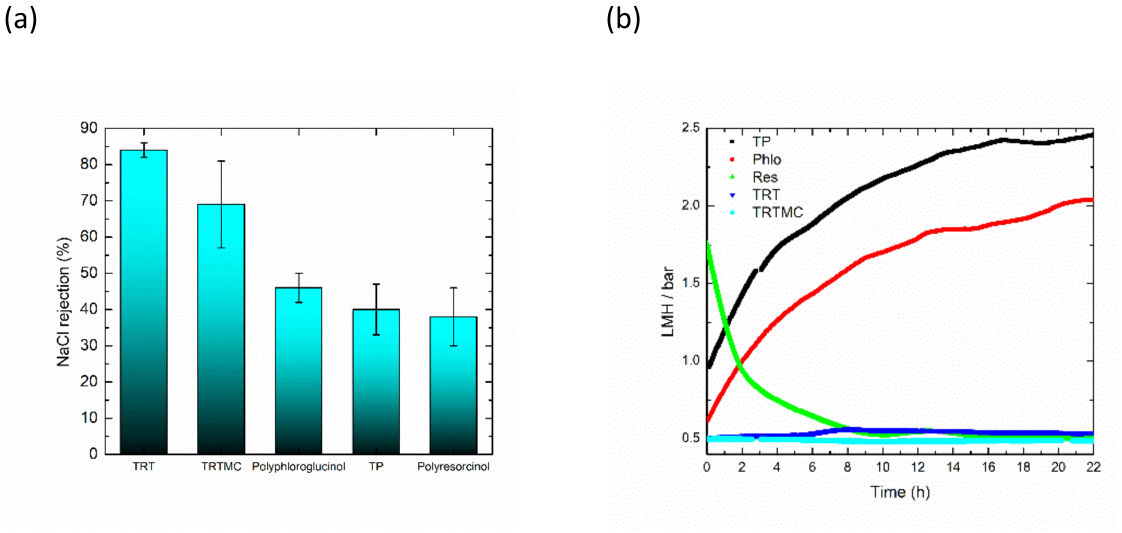

Figure 21: (a) 2000 ppm NaCl rejection by the different electropolymerized membranes. (b) Change in flux of the different electropolymerized membranes over time as 17 bar is applied in a cross-flow module.

Salt rejection of the polymer films were tested using 2000 ppm NaCl solution in a cross-flow module at 17 bar (Figure 21a). Among the 5 types of polymer films, TRT film had the highest NaCl rejection at 84±2 %, followed by TRTMC at 69±12 %. Polyphloroglucinol, TP and polyresorcinol films had low NaCl rejections at 46±4 %, 40±7 % and 38±8 % respectively.

The low salt rejection of Polyresorcinol films is caused by low coverage of polyresorcinol, as shown by both FTIR and SEM images in Figure 19 and Figure 20, respectively. The low coverage and low thickness of polyresorcinol was exhibited by a higher water flux at the start of the salt rejection experiment compared to TRT and TRTMC (Figure 21b). Water flux started at around 1.76 LMH/bar for polyresorcinol, which is around 3.5 times higher than the water flux of TRT and TRTMC. However, the water flux of polyresorcinol decreased over time to match the values of TRT and TRTMC at around 0.5 LMH/bar. The drop in water flux for polyresorcinol is caused by compression of the polymer by water pressure in the cross-flow module operating at 19 bar.

The water flux of T+P and phloroglucinol films increased over time and did not seem to reach a steady state even after 22 hours. The salt rejection experiments were stopped at 22 h for phloroglucinol and T+P films due to their instability, and their salt rejection was measured at 20 h. The salt rejection results for R, T+R+T and T+R+TMC were obtained when the conductivity of the permeate became stable after 20 h.

To find out if the electropolymerized phloroglucinol films were dissolving in water, the films were soaked in 2000 ppm NaCl over a period of 7 days. Thereafter, SEM (Appendix 4. 1) and TGA (Appendix 4. 2) characterization were performed.

Loss of weight due to pyrolysis of polyphloroglucinol (Wt loss %) up to 900 ^{o}C was calculated using the equation:

$$Wt\ loss\ \% = Total\ wt\ loss\ \% - Water\ wt\ loss\ \% - SWNT\ wt\ loss\ \% \quad (1)$$

The weight loss of polyphloroglucinol right after polymerization was 41 %, and the weight loss of polyphloroglucinol after soaking in 2000 ppm NaCl for 7 days was 46.5 %. This means there was no loss of polyphloroglucinol after soaking it for 7 days. The slight increase of wt loss % of polyphloroglucinol after soaking in water was possibly a result of fluctuations between experiments.

SEM images of the phloroglucinol film before and after soaking in 2000 ppm NaCl reveals no significant change in the surface morphology (Appendix 4. 1). SWNT coverage by polyresorcinol was equally dense before and after soaking.

We speculate the drop in salt rejection and the increase in water flux observed during the salt rejection tests were caused by cracks formed in the phloroglucinol and T+P films.

Compared to polyresorcinol, TRT and TRTMC films, the degree of cross-linking in polyphloroglucinol films is expected to be higher. Phloroglucinol contains 3 ring-activating substituents (-OH) compared to 2 on resorcinol, making it highly activated for ring-substitution activities. Polyphloroglucinol chain flexibility is also expected to be stiffer due to steric hindrance of another -OH on its aromatic ring. Under pressure in the cross-flow module during salt rejection tests, instead of getting compressed like polyresorcinol, polyphloroglucinol and T+P formed micro cracks. The cracks then led to an irreversible rise in water flux and salt permeation.

4.5 Conclusion

Electropolymerization of aromatic moieties similar to state-of-the-art polyamide RO membranes have allowed the fabrication of salt-rejecting membranes capable of up to 84±2% NaCl rejection. Multiple monomers in various electropolymerizing permutations have been explored, and the electropolymerization of a mixture of resorcinol and trimesic acid, followed by de-esterification resulted in membranes with the highest salt rejection capability owing to a dense structure formed with reasonable flexibility to withstand high pressures in a cross-flow module. End-capping free -OH groups with TMC did not result in improved salt rejection performance probably as a consequence of bubbles from condensation reactions breaking through the dense confined electropolymerized layer. An electropolymerization mixture of phloroglucinol with and without trimesic acid did not result in significantly different chemical structures, possibly due to a much lower O-H bond dissociation energy in phloroglucinol compared to trimesic acid. However, the resulting polyphloroglucinol membrane was too brittle to withstand compaction during salt rejection tests as a result of a rigid highly cross-linked structure formed.

4.6 Appendix

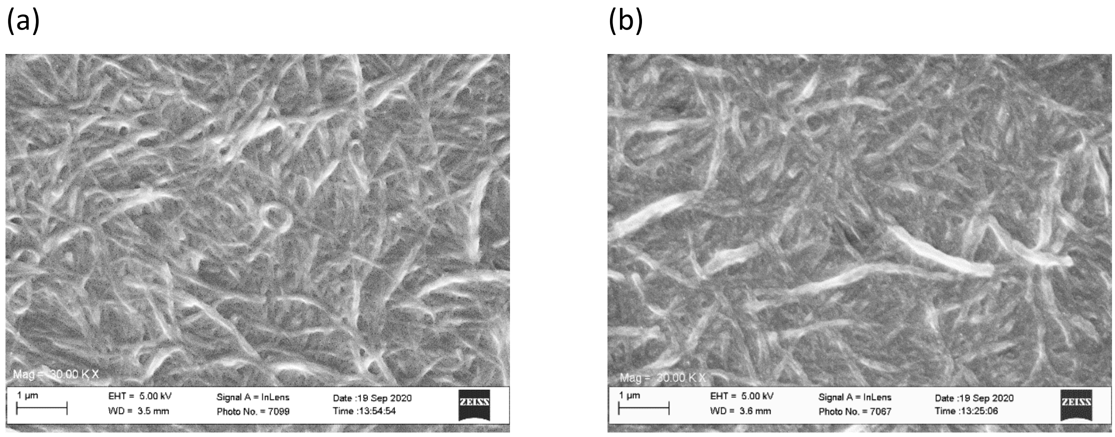

Appendix 4. 1: SEM of electropolymerized polyphloroglucinol film on SWCNT (a) before and (b) after soaking in 2000ppm NaCl for 7 days.

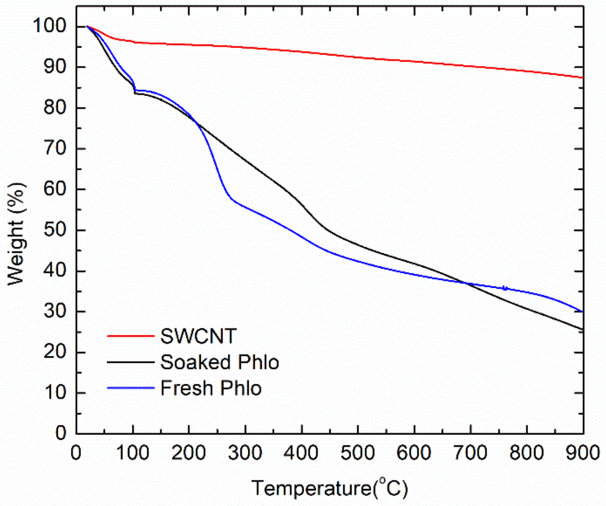

Appendix 4. 2: TGA of phloroglucinol before and after soaking in 2000 ppm NaCl, and SWCNT used directly purchased.

Chapter 5: Electrically Mediated Membrane Pore Gating via Grafted Polymer Brushes

5.1 Abstract

Stimuli-responsive membranes that enable the smart control of membrane transport properties represent an interesting class of materials for a wide range of separation processes. In this work, surface initiated, electrochemically-mediated atom transfer radical polymerization was used to grow poly(acrylic acid) brushes from the surface of a percolating network of carbon nanotubes coating an ultrafiltration membrane. Brush molecular weights as high as 930 kDa were achieved, with very low dispersivity. When no potential was applied, the material was able to reject 88% of 12 kDa dextran in 50 mM NaCl solution. Membrane rejection and flux were readily changed upon the application of electrical potentials, with positive potentials increasing flux by 85% and reducing rejection by 56%, while negative potentials reduced flux by 30% and increased rejection by 5%. We show evidence that counter-ion migration, moving in response to the applied electric field, is responsible for the expansion or collapse of the grafted charged polymer brushes, which induced or eliminated pore gating. In addition, atomic force microscopy was used to probe the forces exerted by brush conformational changes in response to the applied field. These materials can find applications in industrial separations where gating is needed and may possess interesting anti-fouling properties.

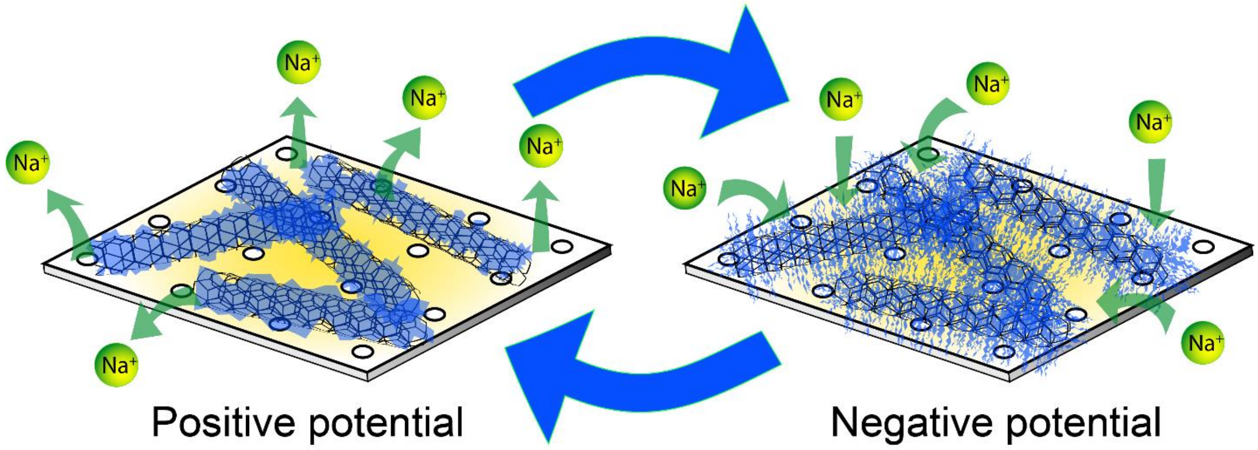

5.2 Introduction

Polymeric membrane separation processes are used across a wide range of industrial activities, including water and wastewater treatment, pharmaceutical and semiconductor manufacturing, and food and beverage production.[217-220] However, standard membrane materials are passive, in that their surface and transport properties (*e.g.*, molecular weight cut-off (*MWCO*), surface hydrophilicity, surface charge) are largely determined by the polymer properties that compose the membrane material, which respond only weakly to the surrounding environment.[221-223] Stimuli-responsive membranes, defined as membranes whose surface/transport properties respond rapidly and dramatically to changes in the local environment, offer distinct advantages over traditional membrane materials, such as the ability to transform from hydrophobic to hydrophilic, the ability to rapidly modify the conformation of surface groups (which change the transport properties of the material), as well as self-healing capabilities.[224-226] External stimuli can be applied in the form of an electrical signal, pH, temperature, and UV light.[202, 227-229] Out of these methods, electrical stimuli offer a promising approach, as they can be rapidly applied, can be incorporated into standard membrane module packaging, and do not require the modification (i.e., chemical or thermal) of the entire feed stream.

Various coatings have been demonstrated to respond to electrical stimuli, one of which is poly(acrylic acid) (*PAA*).[229, 230] This polymer has also been shown to respond (expand or contract) to pH changes,[231] making it suitable for applications where pH changes are common, such as in the digestive tract.[232] Owing to the abundance of carboxylic groups present on the polymer, *PAA* has the ability to “open” and “close” pores in gating applications.[233] An example is in glucose-responsive gating: when in contact with glucose, glucose oxidase immobilized on *PAA* produced a carboxylic acid, which caused *PAA* to shrink and open pores on the membrane it was grafted to.[234] A blend of *PAA* and polyvinyl alcohol as a hydrogel membrane has also been shown to respond to electrical fields, where trypsin diffusion increased as a result of increased electric field that caused expansion of pore channels within the suspended hydrogel membrane.[235]

A common manifestation of stimuli-responsive membranes involves the presence of polymer brushes attached to the membrane surface.[222, 236] Surface-initiated electrochemically mediated atom transfer radical polymerization (*SI-eATRP*) is a grafting-from technique that enables polymer growth directly from material surfaces.[237-240] The polymerization of acidic monomers using *ATRP* is typically difficult to carry-out due to coordination of transition-metal-based species (*e.g.* Cu(I)) to the carboxylate groups present on the growing polymer chains, halide anion displacement from the deactivated complex, and protonation of the ligand at low pH.[241, 242]

In this study, *SI-eATRP* was used to grow *PAA* brushes onto an electrically conducting support composed of a percolating network of carbon nanotubes (*CNTs*) deposited on a polysulfone ultrafiltration (*UF*) membrane support. We demonstrate how the grafted *PAA* brushes respond to the application of electrical potentials to the *CNT* network, and show how membrane rejection and flux can be easily modified by simply switching the polarity of the applied potential. Atomic force microscopy (*AFM*) is used to describe the forces exerted by the extended/contracted *PAA* brushes, and a mechanism for the observed phenomena is proposed. To the best of our knowledge, this is the first time a *PAA*-grafted membrane material is shown to respond to direct electrical stimuli, without the need to modify feed stream conditions.

5.1 Material and methods

5.1.1 Materials

Polysulfone UF membranes (molecular weight cut-off of 20 kDa) were kindly provided by Solecta Membranes (Oceanside, CA). Carboxyl-functionalized multiwalled CNTs were purchased from Cheaptubes (Grafton, Vt). Dodecylbenzenesulfonic acid, Sodium chloride, Sodium hydroxide, α-Bromoisobutyryl bromide, 12 kDa dextran and Copper(II) chloride were purchased from Sigma Aldrich (St. Louis, MO). 3-hydroxytyramine hydrochloride (Dopamine-HCl), Acrylic acid, Tris(hydroxymethyl aminomethane), Hydrochloric acid, Tetrahydrofuran, 10kDa dextran and Triethylamine were purchased from Thermo Fisher Scientific (Grand Island, NY). 4-(Chloromethyl)phenyltrichlorosilane and 6kDa dextran was purchased from Alfa Aesar (Haverhill, MA). Tris(2-pyridylmethyl)amine was purchased form Tokyo Chemical Industries (Portland, OR). Difac tryptic soy agar was purchased from BD Biosciences (San Jose, CA) 2.5

kDa dextran was purchased from Chem-Impex International (Wood Dale, IL). Aluminium foil was a commercial product from Reynolds kitchen (Louisville, KY). DI water used in the experiments was provided in house. All chemicals and membrane support were used as received.

5.1.2 Methods

5.1.2.1 CNT modified membrane fabrication

COOH-functionalized CNTs were suspended in deionized water with 0.1% w/w dodecylbenzenesulfonic acid (a surfactant) by using a sonication probe for 30 min to make a 0.1 g/L CNT suspension.[202] The resulting suspension was centrifuged at 11,000 rcf for 30 min. The prepared CNT suspension was then pressure-deposited at 60 PSI onto a 20 kDa polysulfone UF membrane support.

5.1.2.2 DOPA coating on CNT modified membrane fabrication

In the second step, polydopamine (DOPA) was deposited onto the CNT layer using a previously-reported method.[243] In short, 0.55 g of 3-hydroxytyramine hydrochloride and 18.2 g of Tris(hydroxymethyl aminomethane) were dissolved in 150 ml of deionized water. The solution pH was adjusted to pH 8.5 using NaOH, and the CNT modified membrane was immersed into the solution in a vertical orientation. For our studies, air was bubbled into the solution for 1 h.

5.1.2.3 Membrane support fabrication with 4-(Chloromethyl)phenyltrichlorosilane (CMPS)

The initiator, 4-(Chloromethyl)phenyltrichlorosilane (CMPS) was deposited onto the CNT modified membrane via chemical vapour deposition at 6.5 kPa and 333.15 K in a desiccator, where the CNT-coated UF membranes were taped to the desiccator cover and CMPS vapor was generated at the bottom of the desiccator and allowed to drift upwards towards the membranes.

5.1.2.4 Membrane support fabrication with α-Bromoisobutyryl bromide (BiBB)

Immobilization of α-Bromoisobutyryl bromide (BiBB) on carboxylic acid-functionalized CNTs was achieved as follows: 0.2 g COOH-functionalized CNT was sonicated in tetrahydrofuran (THF) for 1 hour. Thereafter, 1 mL of triethylamine and 5 mL of BiBB was added to the reaction mixture and stirred at 333.15 K for 24 h. The produced BiBB immobilized CNT (BiBB-CNT) was washed extensively with water and dried under vacuum at 333.15 K. To produce the initiator-functionalized conductive membrane support, BiBB-CNT was suspended in deionized water with 0.1% w/w dodecylbenzenesulfonic acid (a surfactant) by using a sonication probe for 30 min to make a 0.1 g/L CNT suspension.[202] The resulting suspension was centrifuged at 11,000 rcf for 30 min. The prepared CNT suspension was then pressure-deposited at 60 PSI onto a 20 kDa polysulfone UF membrane support.

5.1.2.5 Growing PAA brushes using eATRP

The fourth step of the fabrication process involves the growth of PAA brushes using eATRP. The reaction solution was prepared by mixing 1 mM Copper(II) Chloride, 1 mM Tris(2-pyridylmethyl)amine, and 10% v/v acrylic acid in 350 ml of deionized water. The pH of the solution was then adjusted to pH 10 using NaOH. A 3-electrode system connected to a potentiostat (CHI600E, Austin, TX) was used for the eATRP process, with a Ag/AgCl in 3 M KCl electrode (Fisherbrand Accumet, Hampton, NH) used as the reference electrode, and a 3 g roll of aluminium foil made from commercial aluminium foil (Reynold’s wrap) and separated from the eATRP solution in a fritted glass cell with agar gel at the bottom and filled with saturated NaCl was used as the counter electrode; the working electrode was a piece of stainless steel foil (McMaster, Santa Fe Springs, CA) (Figure 22). The solution was purged with nitrogen gas for 30 min before an electrical potential was applied. Under potentiostatic conditions, a reducing potential (-0.6V), determined using cyclic voltammetry (performed in the range of 0 V to -1 V at 0.1 V/s) was applied to the working electrode for 3 hours with the initiator-deposited membrane immersed near the working electrode. After polymerization, the modified membrane was flushed with water in the UF system for 2 hours before experiments.

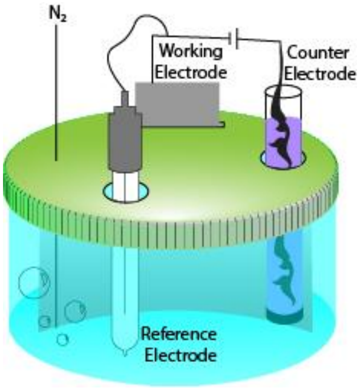

Figure 22: Electrochemical set-up for synthesis of PAA using the eATRP method

5.1.2.6 Gel permeation chromatography analysis of PAA polymer brushes

Gel permeation chromatography (GPC) was used to determine the MW of the PAA brushes grown using the eATRP process as a function of reaction time. Following polymerization, PAA – grafted filter paper was sonicated in a pH 13 solution (adjusted with NaOH) for 30 min. The suspension was then filtered through a 3 μm filter (GE Healthcare Whatman, Grade 6, Pittsburg, PA) and neutralized with HCl to pH 4. Excess HCl and NaCl was removed by dialysis using a 3.5K MWCO dialysis tubing (Sigma Aldrich). The concentration of

PAA in the resulting dialysed solution was determined using total organic carbon (TOC) analysis (Shimadzu TOC-L, Carlsbad, CA). Aqueous GPC was carried out on a Malvern Viscotek GPCMax (Westborough, MA) system equipped with a triple detector array and two Viscotek A6000M, general mixed aqueous columns (300 x 8.0 mm). 100 µL of samples were injected into the instrument, with 0.2 M sodium sulfate (80%) + 20% acetonitrile used as the eluent with a flow rate of 1 mL/min. The dn/dc value was calculated to be 0.15.

5.1.2.7 Membrane characterization

Static water contact angles were obtained using a contact angle goniometer (Rame-hart, Succasunna, NJ). Reported contact angle values are an average of five measurements obtained for each sample with a drop volume of 5 μl. Chemical bonds on the membrane were characterized using Fourier transform infrared spectroscopy (FTIR) operated in the attenuated total reflectance mode (Thermo Scientific FTIR iS10 Smart iTR Basic, Mandison, WI), with a ZnSe prism as an internal reflection element. Surface morphology and forces exerted by the extended/retracted polymer brushes were characterized using atomic force microscopy (AFM) (Bruker Dimension FastScan Scanning Probe Microscope, Santa Barbara, CA). AFM images were obtained using ScanAsyst-Air and probes (Camarillo, CA). A rounded AFM tip of 30 nm radii (Nanosensors, Neuchâtel, Switzerland) and spring constant 0.26 N/m, was used for the determination of AFM force curves. The cantilevers were not grounded. Cantilever deflection sensitivity was determined from 10 force curves, using the slope of the noncompliance region of the cantilever deflection vs the piezo displacement curve obtained on a glass surface. The spring constant of the cantilever was determined using the thermal tune method at 293.15 K. Each force curve was produced from an average of 128 individual force curves taken at a frequency of 1 Hz. The obtained force curves were analysed using NanoScope Analysis (version 1.80). Young's modulus of the surface was obtained using the cone sphere model. The chemical composition of the membrane's surface was determined using X-ray photon spectroscopy (XPS) (Kratos Axis Ultra DLD spectrometer equipped with a monochromatic Al Kα X-ray source). High-resolution spectra were calibrated using carbon tape (Ted Pella) with a known C1s binding energy of 284.6 eV. Raw data were processed using CasaXPS software (version 2.3.19).

5.1.2.8 Ultrafiltration system set-up and operating procedure

The membrane was tested in a cross-flow filtration module capable of housing electroactive membranes, which is described in detail in previous publications (Figure 23).[203, 204] The flat sheet membrane module had a feed channel with the dimensions 100 mm × 40 mm × 3.80 mm. The UF system was operated at constant pressure, with a proportional-integral-derivative control valve used to adjust and maintain the hydraulic pressure of the system. During the filtration process, feed flow rate was maintained at 0.7 L/min (crossflow velocity of 7.7 cm/s) using a gear pump (Leeson Electric). Prior to filtration tests, membranes were compressed at 90 psi with deionized water until a stable flux was observed.

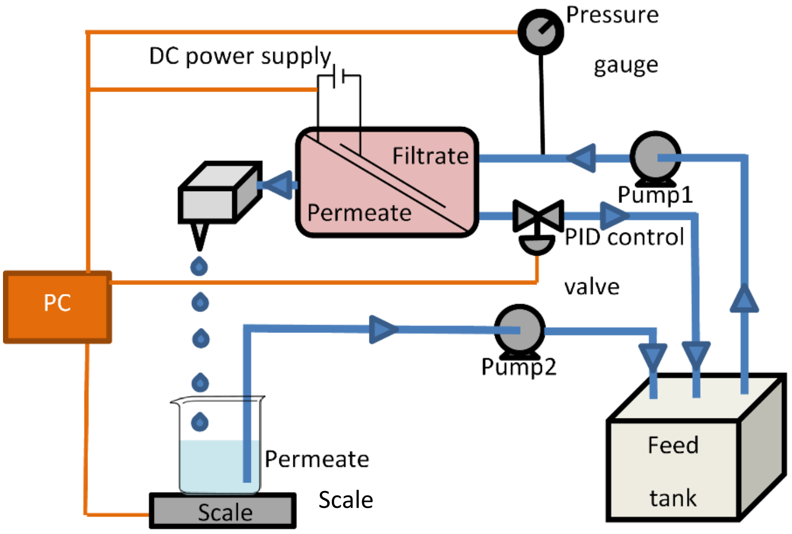

Figure 23: UF system design. Orange lines represent power and data connection, blue lines represent water flow.

5.1.2.9 Membrane module

Figure 24 describes the membrane module used in our experiments. A power supply is connected to the working and counter electrodes where a titanium plate located above the membrane acts as the counter electrode, and the conductive membrane acts as the working electrode.

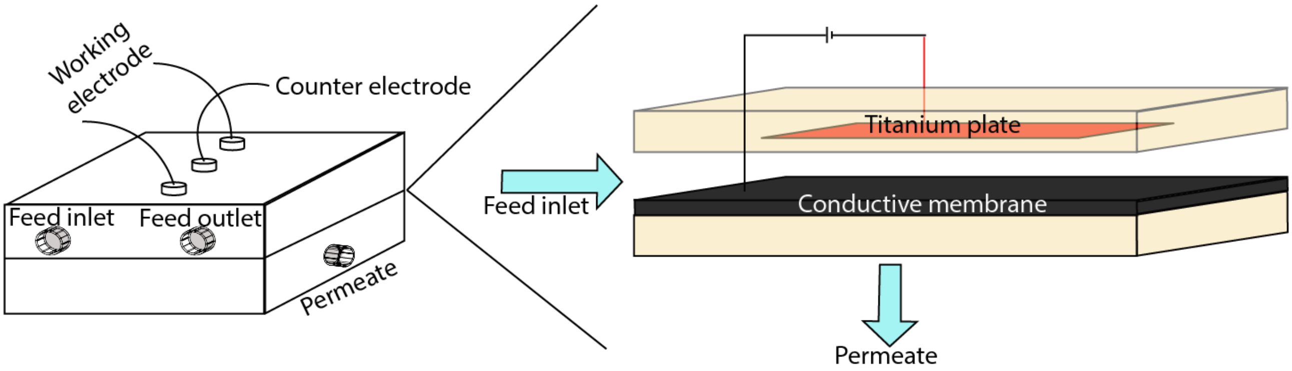

Figure 24: Membrane module. Electrical potentials are applied onto the membrane through a wire connected to the inside of the membrane module, and a counter elecctrode fixed above the membrane.

5.1.2.10 AFM – calculation of pressure exerted by PAA on AFM tip

From the manufacturer's data, the rounded AFM tip has a spherical apex of 30 nm radius, and a half angle of 15^0. Figure S13 shows the idealized shape of the rounded AFM tip.

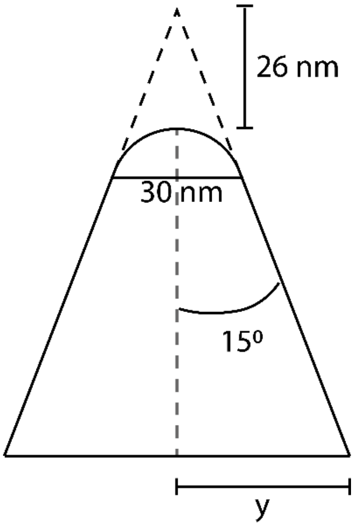

Figure 25: Idealized shape of the rounded AFM tip viewed from the side

Pressure exerted by the PAA brushes on the AFM tip was calculated by:

$$\mathrm{P} = \mathrm{L}/\mathrm{A} \tag{27}$$

Where L is the indentation load, and A is the area of contact.

To calculate the area of contact normal to the indentation load for indentation (δ) ≤ 30 nm, the following equation was used:

$$\mathrm{x} = \sqrt{30^2 - (30 - \delta)^2} \tag{28}$$

$$\mathrm{A} = \pi \mathrm{x}^2 \tag{29}$$

Where x is the radius of the sphere in contact with the membrane.

For the area of contact normal to the indentation load when δ > 30 nm, the radius of the cone AFM tip (y) was calculated using:

$$y = \tan 15^0 (\delta + 26 \text{ nm}) \quad (30)$$

$$A = \pi y^2 \quad (31)$$

δ is obtained from the force curves as the distance between the point where cantilever deflection occurs to the point where the prominent peak force is observed.

5.3 Results and discussion

A novel 4-step approach was used to fabricate the electro-responsive *PAA*-grafted membranes (Figure 26: Membrane modification pathway. Step 1: pressure deposition of CNTs. Step 2: polymerization of DOPA. Step 3: CVD of CMPS. Step 4: eATRP of PAA from CNT modified membrane.). First, carboxyl-functionalized *CNTs* 1% w/w were suspended in deionized (*DI*) water with 0.1% w/w dodecylbenzenesulfonic acid, and pressure pressure-deposited onto a 20 kDa polysulfone *UF* membrane support.[202] Next, to increase the number of anchoring sites for the *ATRP* initiator, polydopamine (*DOPA)* was deposited onto the *CNT* modified membrane using a previously-reported method.[243] In our system, air was bubbled into the solution during the *DOPA* deposition step to enhance mixing and reduce the time necessary for the polymerization reaction. In the third step, the *ATRP* initiator, 4-(chloromethyl)phenyltrichlorosilane (*CMPS*) was deposited onto the *CNT* modified membrane via chemical vapor deposition (*CVD*) (6.5 kPa and 333.15 K). Finally, *eATRP* was employed for the grafting of *PAA* brushes from the surface of the membrane. To overcome difficulties inherent to polymerizing acidic monomers via *eATRP*, the reaction solution was adjusted to pH 10, [243, 244] and a very low Cu(I):Cu(II) ratio (0.01) was targeted through the application of a reducing voltage to the polymerization solution.

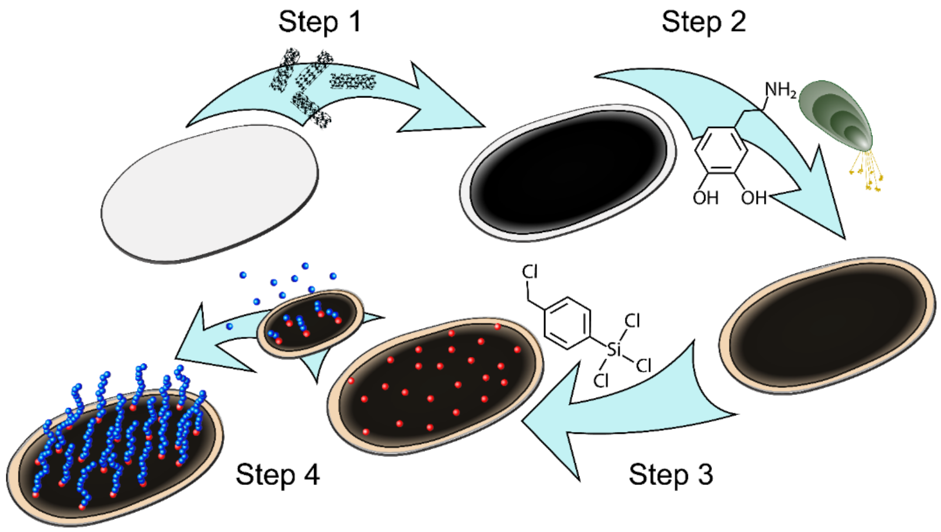

Figure 26: Membrane modification pathway. Step 1: pressure deposition of CNTs. Step 2: polymerization of DOPA. Step 3: CVD of CMPS. Step 4: eATRP of PAA from CNT modified membrane.

X-ray photoelectron spectroscopy (*XPS*) was employed to determine the evolving surface composition of the fabricated material (Figure 27a and Table 1). The *CNT* modified membrane is composed primarily of carbon (C 1s 284.8eV) and oxygen (O 1s 531.8 eV). Following *DOPA* deposition, nitrogen peaks (N 1s 399.8 eV), associated with the *DOPA* amine groups, appeared, accounting for 3.58% of the surface composition; there was also an increase in oxygen surface composition from 2.03% to 8.56%, associated with the hydroxyl substituents present on *DOPA*. The increase in O:N ratio was approximately 2:1, in agreement with the theoretical molecular ratio found in *DOPA*. Following *CMPS* deposition, the appearance of chlorine peaks (Cl 2p 200.3 eV), which accounted for 2.33% of surface atoms, and silicon peaks (Si 2p 102.3 eV), accounting for 2.79% of surface atoms, demonstrates the successful deposition of *CMPS* on the membrane surface. Figure 2b and 2c show the high-resolution spectra of C 1s after *CMPS* deposition and *PAA* polymerization, respectively. The peaks were deconvoluted into 4 components, centered at 284.8 eV, 285.4 eV, 286 eV and 289 eV, which can be attributed to C-C bonds, C-O bonds, C-N bonds, and O-C=O bonds, respectively.[245, 246] The appearance of a peak at 289 eV indicates the successful formation of

PAA, with the amount of carboxylic groups increasing from 1.7% to 10.9%. Additionally, the continual existence of chlorine (Figure 2a) on the membrane surface after *PAA* polymerization indicates the successful implementation of *eATRP* reaction; these chlorine groups act as initiating sites that would allow further extension of the polymer chains so that targeting of specific degrees of polymerization is possible.[247, 248] Surface characterization using contact angle goniometry and Fourier-transform infrared spectroscopy (*FTIR*) also showed the successful fabrication of the membrane in each step (Appendix 5. 5).

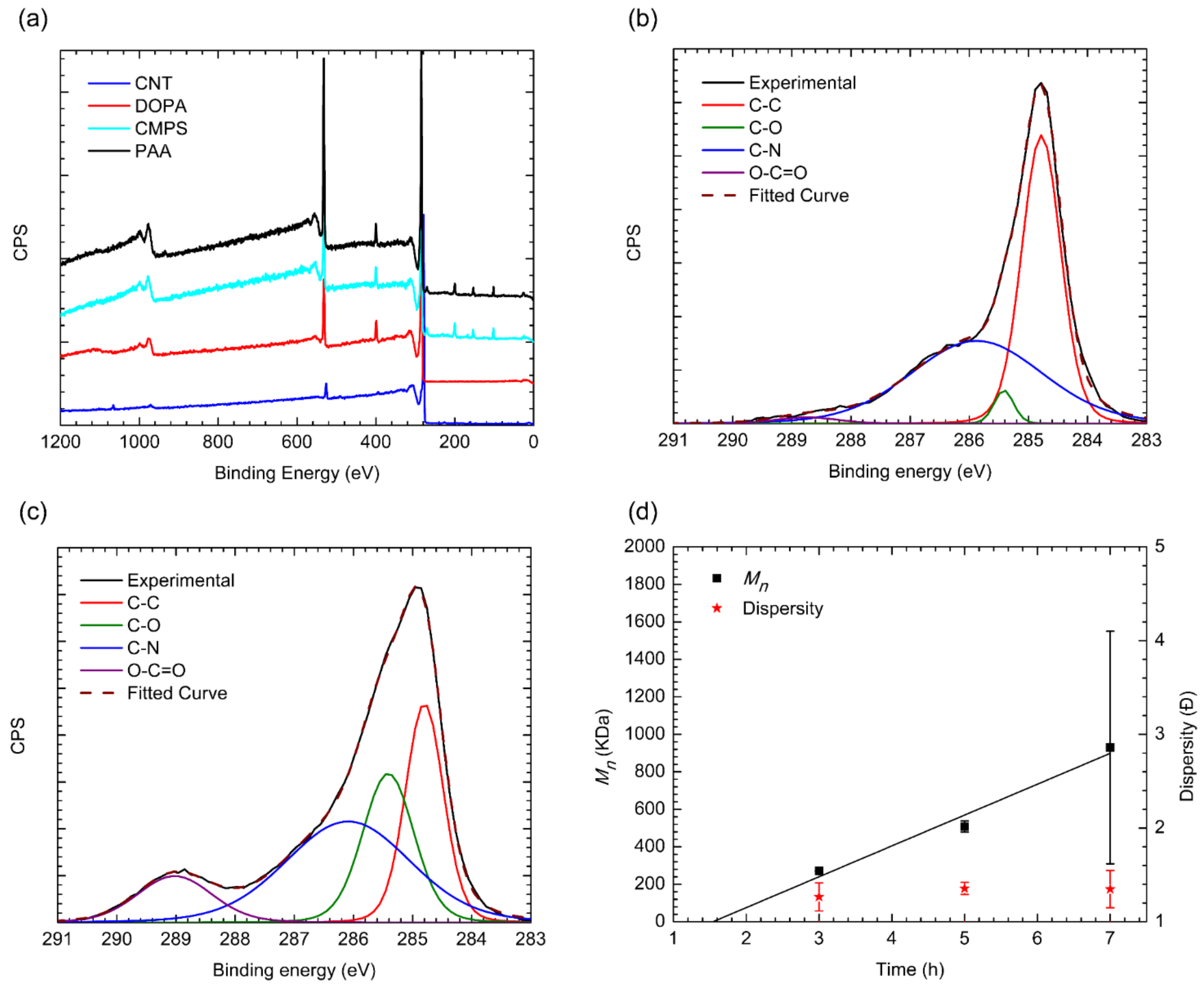

Figure 27: (a) XPS spectra of the membrane at different fabrication stages. (b) C 1s high-resolution spectra of CMPS coated membrane. (c) C 1s high-resolution spectra of PAA-grafted membrane following eATRP. (d) Molecular weight evolution of PAA with time is linear with low dispersity.

Table 11. Atomic % composition of different elements on the membrane surface after each modification step

Sample	*Atomic % of each element*				
	C	**O**	**N**	**Cl**	**Si**
CNT	**97.97**	**2.03**	**-**	**-**	**-**
DOPA	**87.86**	**8.56**	**3.58**	**-**	**-**
CMPS	**78.88**	**13.23**	**2.77**	**2.33**	**2.79**
PAA	**76.45**	**17.39**	**2.54**	**1.47**	**2.16**

Gel-permeation chromatography (*GPC*) was used to determine the number average molecular weight (M_n) and dispersity of the grafted *PAA*. The weight average MW was obtained by a Low angle and right-angle light scattering detector that came with the analytical equipment (Viscotek TDAmax). To conduct the characterization, *PAA* brushes were cleaved from filter paper coated with *CMPS*, rather than from the *CNT* modified membranes, due to difficulty encountered when attempting to separate *PAA* from solubilized *DOPA* and polysulfone. The conditions used to conduct *eATRP* on filter paper were the same as that used for *CNT* modified membranes, but *CNT* and *DOPA* were not deposited on the filter paper before *CMPS* deposition. Si-O bonds in the *CMPS* molecule, which serves as the brush anchor for *PAA*, are readily hydrolysed under alkaline conditions (pH > 8), enabling the cleavage of *PAA* from the support. Unfortunately, under such conditions, *DOPA* and polysulfone are also hydrolysed, which adds extra molecular weights to the *GPC* readings, which is why these polymers were not included to determine polymer molecular weight.[249] Filter paper is composed of cellulose that contains abundant hydroxyl groups, enabling direct covalent linkage of *CMPS* to the surface. The surface composition of Cl on both filter paper and the *CNT* modified membranes were found to be similar, with 2.39% Cl on filter paper, and 2.33% Cl on *CNT* modified membranes (Appendix 5. 6). Thus, we assume that the grafting density of *PAA* on both substrates were similar. It should be noted that the root mean square roughness of filter paper (58.3 nm) is approximately twice that of the deposited CNT layer (30.1 nm), which could result in differences in PAA dispersivity, and chain length due to differences in catalyst and monomer diffusion towards the two surfaces (Appendix 5. 6).[250] *GPC* analysis of *PAA* chains grown on filter paper showed a linear increase in the M_n with reaction time (Figure 2d). Experiments were done in duplicate. The linear relationship allows for the easy tuning of brush M_n, which can allow optimal pairing between brush length and the desired application. The large error bar associated with the 7 h time point could be a result of small differences in the reactor (e.g., mixing conditions and temperature variability), which could impact reaction rates, being magnified over the prolonged reaction period, leading to some variability in the overall molecular weight of the brushes. Although the polymer dispersity is relatively high for controlled polymerization (1.27-1.37), other studies reported similar PDI values when growing high MW polymers using ATRP methods.[251, 252] The very low Cu(I) to Cu(II) ratio targeted during the *eATRP* process, was used to control the polymerization reaction, which minimized the dispersity of the resulting polymer brushes.[253] The low dispersity hints at the possibility for uniform sized pore gating that would provide a sharp molecular weight cut-off (*MWCO*) for the membrane. After 3 h of polymerization, the M_n of *PAA* reached 343 kDa.

To demonstrate the electro-responsive properties of PAA-grafted membranes, membrane transport properties were evaluated while applying different potentials to the *CNT* network. Specifically, we evaluated the permeability and percentage of dextran rejection to calculate the *MWCO* of the membrane as a function of the applied potential. Dextran was chosen as a model molecule due to its charge neutrality and globular structure, which minimizes electrostatic interactions and the propensity for conformational changes in response to the applied pressure gradient at the membrane/water interface.[254] Further, it was shown that dextran does not significantly foul polysulfone membranes, and thus, it is suitable for membrane characterization.[255-257]

Figure 28a shows changes in membrane permeability during the filtration of a 50 mM NaCl solution at a constant pressure of 6.2 bar when a positive potential was applied to the modified membrane (2 V cell potential with membrane as anode). When no potential was applied, membrane permeability was 5.4 L m^{-2} h^{-1} bar^{-1}. However, when +2 V cell potential were applied, permeability nearly doubled, to 10 L m^{-2} h^{-1} bar^{-1}. The ability of the *PAA*-grafted membrane to respond to the applied potential was rapid, with maximum permeability achieved within 10 min. We speculate that the complex and dynamic nature of the counter ion concentration profile inside the brush matrix leads to inhomogeneous distribution of ions, potentially forcing the migration of sodium counter ions against their concentration gradient, which could result in overall lower transport rates out of the brush matrix. On the other hand, the slow swelling rate of the polymer brushes could have been caused by strong Van der Waals' forces among the ultra-high molecular weight PAA brushes. However, we do not have direct evidence of this, and this is certainly something that needs to be investigated further.

Cycling between 0 V and +2 V cell potential repeatedly (and consistently) cycled the permeability, indicating good stability of the modified membrane, making it suitable for pore gating applications. Cycling between 0 V and -2 V cell potential did not result in a significant change in permeability, indicating that the native negative charges associated with the *PAA* carboxyl groups were insufficient to induce conformational changes in the *PAA* structure (i.e., the addition of a negative charge on the *CNT* surface does not lead to any additional phenomena) (Appendix 5. 7).

In *DI* water, one would expect that electrostatic repulsive forces between *PAA* chains to be stronger than in salt solution due to a compressed electrical double layer. This would cause the *PAA*-grafted membrane pores to become constrained (due to brush expansion), and flux to decrease. In addition, we expected the impact of the applied potential to be larger. However, previous studies have shown that the swelling of PAA brushes in DI water is hampered due to enhanced protonation, compared to PAA in salt solution, where the dissociated form of PAA dominates.[258] In our experiments, when *DI* water was used to determine permeability, no significant changes were observed when an external potential was applied, with permeability stable at approximately 13.5 L m^{-2} h^{-1} bar^{-1} (Figure 28b). We hypothesize that the lack of responsiveness observed in *DI* water is due to the absence of Na^+ ions. In solution, the negative charge of deprotonated *PAA* chains will be balanced by hydrated Na^+ ions, which causes the polymer chains to swell. When a positive potential is applied, these Na^+ ions migrate away from the membrane surface in response to the applied field, which causes the chains to collapse, and the pores on the membrane to become larger;

the negative charges of the deprotonated *PAA* chains are balanced by the induced positive charges on the *CNT* surface.

It was further observed that membrane permeability in DI water (13.5 L m^{-2} h^{-1} bar^{-1}) was higher than in 50 mM NaCl (5.4 L m^{-2} h^{-1} bar^{-1}) when no voltage was applied. This is attributed to reduced PAA brush swelling in DI water, which is caused by enhanced protonation of the carboxylic acid groups, due to charge imbalances in the polymer.[258] However, in the presence of NaCl, more extensive deprotonation is expected, which leads to expanded brushes and pore closing. In DI water and during the application of +2 V in salt water, the absence of Na^+ ions caused the collapse of PAA brushes. However, it was observed in Figure 28 that DI water permeability was higher than the maximum permeability of the membrane in saltwater. We believe that when +2 V was applied in 50 mM NaCl, not all Na^+ ions migrated out of the membrane. Further increasing the applied voltage results in further increase of the membrane permeability (data not shown). However, electrooxidation of the CNT substrate at these elevated voltages prevented the exploration of these conditions.

To test the impact of the applied potential on the rejection properties of the membrane, the *PAA*-grafted membranes were used to reject dextran molecules with different molecular weights (between 2.5 kDa and 12 kDa). Experiments were done in triplicates. Importantly, the porous polysulfone support used as the substrate for *CNT* deposition (which underlies all the membranes evaluated in this work), had a *MWCO* of 20 kDa according to manufacturer data. The impact of the applied potential on membrane rejection can be seen in Figure 28c. The highest dextran rejection was observed when -2 V cell potential was applied to the *PAA*-grafted membrane (membrane as cathode), followed by 0 V, and then +2 V cell potential (membrane as anode). The membranes coated only with *CNT* and *DOPA* showed nearly no rejection for all the dextrans evaluated in the study, regardless of the applied potential (Figure 28c). When +2 V were applied to the *PAA*-grafted membrane, very little rejection was observed, with maximum rejection of only 32 ± 6 % for the largest dextran evaluated (12 kDa). In contrast, when -2 V were applied to the membrane, the rejection of 12 kDa dextran increased to 93 ± 4 %. When 0 V were applied, the rejection of 12 kDa dextran was 88 ± 6 %, which was not significantly different than the -2 V case. A sigmoidal curve fit through the -2 V data points (R^2 = 0.997) showed that the *MWCO* of the *PAA*-grafted membrane (i.e., the molecular weight where 90% rejection was observed), when electrically actuated (- 2 V cell potential), was 11.5 kDa, while fitted *MWCO* of the membrane when no voltage was applied was 12.4 kDa (R^2 = 0.988). These results correspond well to the permeability data, where the application of a positive potential to the membrane increases permeability and decreases rejection due to the electrically-induced collapse of the polymer brushes. In contrast, when negative potentials are applied, *PAA* brushes are fully extended, resulting in a decline in permeability and concurrent increase in rejection. Thus, these data demonstrate the facile and reversible nature of the electrical actuation of the grafted *PAA* brushes, potentially serving as a molecular gate to membrane pores.

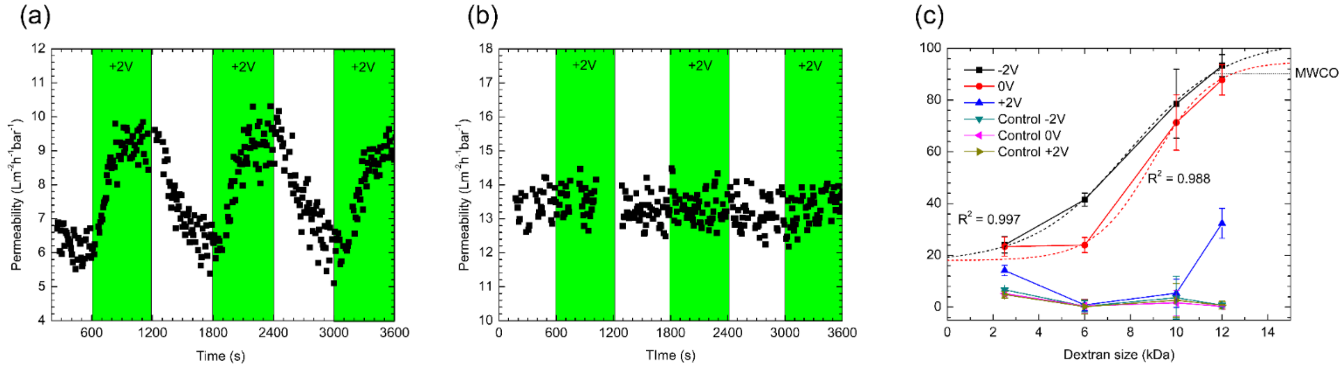

Figure 28: Flux of PAA-grafted membrane at +2 V and 0 V in (a) 50 mM NaCl and (b) DI water. (c) Dextran rejection by PAA-grafted and non-grafted membranes at different applied potentials.

To ensure that changes in polymer brush conformation were not a result of local pH changes due to water electrolysis, membrane potentials were measured vs. a Ag/AgCl, and found to be +0.84 V and -0.021 V when +2 V and -2 V cell potentials were applied, respectively; when no voltage was applied, the membrane potential was +0.006 V vs. Ag/AgCl. Cyclic voltammetry (*CV*) scans between +0.85 V and -0.03 V exhibited little Faradaic behavior in this range, indicating water electrolysis was minimal and not a significant factor at these applied potentials (Appendix 5. 8).

AFM was used to probe temporal changes in the interaction forces between the PAA brushes and solid objects (i.e., the AFM tip), as well as to provide insight into the membrane surface structural changes in response to an applied potential (Figure 29).

From the advancing tip curves (Figure 29a), it was observed that at equilibrium (*i.e.*, once the brushes were either completely extended or contracted, after 30 min of applied potential where there was no significant change in the obtained force curve), the relative thickness of the *PAA* layer (estimated as the point where cantilever deflection begins, to the point the cantilever deflects by 10 nm) when no potential were applied was approximately 600 nm. However, the overall thickness of the brush layer was not determined with complete confidence. Rather, we determined the differences in brush layer lengths when the brushes were fully extended or compacted. When the brushes are collapsed, there is likely a layer of compressed material under the AFM tip, making the absolute thickness difficult to determine. Therefore, changes in the brush length are relative to the fully collapsed brush. When -2 V cell potential were applied, the relative thickness of the brush increased by around 100 nm to 700 nm. At both -2 V and 0 V, penetration of the cantilever tip through the PAA layer was observed. When +2 V were applied, tip deflection began gently at 90 nm, and then rapidly at 17 nm. No tip penetration was observed. This indicates complete collapse of the polymer brushes which then act like a soft gel-like layer when +2 V were applied. These results are consistent with permeability and dextran rejection data. To study the transition between the fully retracted (when +2 V cell potential was applied) and fully extended (when -2 V cell potential is applied) brushes, we tracked the advancing and retracting *AFM* force curves using a rounded AFM tip over time (starting when the potential was switched from +2 V to -2 V cell potential) (Figures 4b and 4c, respectively). The advancing curves, taken at different time intervals (Figure 29b) continuously show a decrease in the elastic modulus calculated using the cone sphere model developed by Briscoe, Sebastian and Adams.[259] At curve (1), (0 min) the elastic modulus was 3.95 MPa which decreased to 0.101 MPa at curve (2) after 73 min. After this, the elastic modulus increased back to 0.287 MPa after 91 min (curve (3)). The initial decrease in the elastic modulus is likely a result of polymer chains stretching out in response to the applied potential.

PAA chain stretching in these experiments was not instantaneous, taking place over 129 min, compared to 10 min when the membrane was tested during filtration (Figure 28a). The prolonged polymer elongation process indicates that the process may be dependent on the diffusion of hydrated counter-ions into the *PAA* brush structure. The *AFM* force curves were taken under static conditions, where Na^+ ion transport was solely dependent on diffusion and migration, while in the filtration experiment, Na^+ ion transport also benefitted from convection.

Prominent repulsive peaks were observed in advancing force curves (3) – (6), at distances ranging between 30 and 180 nm from the surface. These peaks represent pressure exerted on the *AFM* tip by the *PAA* brushes. The pressure exerted by the prominent repulsive peaks were analysed for 24 curves and found to range from 1.4 to 54.8 bar, with an average of 13.2 bar. Calculations are discussed in detail in the supporting information. Based on these heightened repulsive forces, there is a possibility that particles (*e.g.*, colloidal matter, large proteins, bacteria) will be prevented from interacting with the membrane surface, which could minimize membrane fouling.

Figure 29d illustrates the proposed mechanism used to explain the movement of the *AFM* tip as it approaches the *PAA*-grafted membrane surface; the approaching force curve (4) from Figure 29b was used as an illustrative example. At approximately 134 nm (Figure 29d(I)), attractive van der Waals forces between the cantilever tip and the polymer brushes allow adsorption of the polymer brushes onto the cantilever tip. As the cantilever continues approaching the surface (Figure 29d(II)), the adsorbed *PAA* brushes begin to compress, giving rise to a repulsive force; this repulsive force increases as the tip continues to compress the brushes. However, at approximately 55 nm (Figure 29d(III)), the negative charge density within the packed *PAA* brushes is high enough to overcome any compressive steric forces, leading to the "peeling" of the brushes away from the tip, and a large drop in the repulsive force. As the cantilever moves downward, PAA continued to be compressed from 55 to 18 nm, eventually reaching the surface, it begins deflecting rapidly (below 18 nm). Figure 29c shows temporal changes in the retracting curves.

The composition of the local aqueous environment (e.g., pH, ionic strength, ionic species) is likely to impact brush behaviour, and will be investigated in a future study.

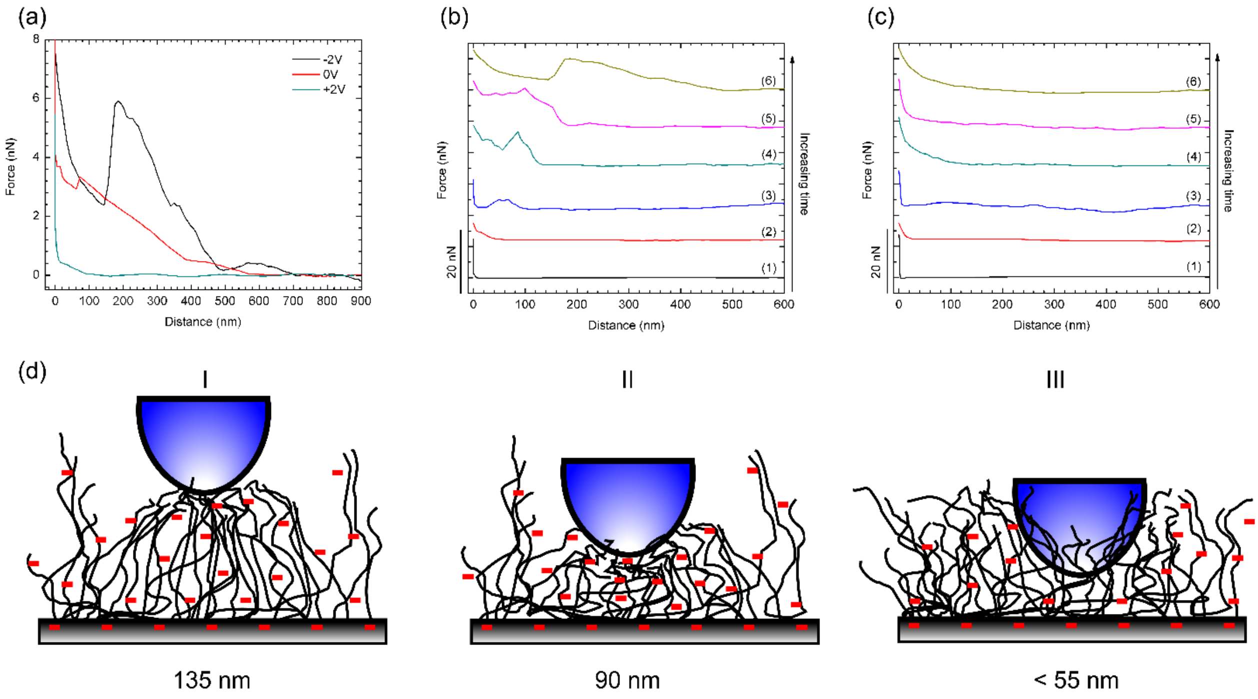

Figure 29: (a) AFM force curves at different applied potentials. (b) Advancing AFM force curves and (c) retracting AFM force curves taken at different time intervals over 129 minutes with curve (1) taken at 0 min, and curve (6) taken at 129 min. (d) Proposed mechanism for PAA brush movement as the AFM tip approaches the PAA-grafted membrane surface.

5.4 Conclusion

In summary, *PAA* brushes were grown on electrically conducting *CNT* modified membranes using *SI-eATRP*. The process yielded polymer brushes of uniform length (evidenced by their low dispersity on filter paper), and the brush length could be controlled by tuning the reaction time. The conformation of grafted *PAA* brushes could be modulated through the application of an electrical potential to the *CNT* surface, with positive potentials leading to brush collapse and negative potentials leading to their extension. It was determined that the mechanism responsible for these conformational changes was the intercalation/deintercalation of counter-ions (in this case, Na^+) that migrated into or out of the brush matrix in response to the applied electrical potential. The extension of the polymer brushes under negative potentials led to membrane pore closure and a decrease in permeability; brush collapse, induced under positive potentials, led to lower rejection and higher permeability. A detailed investigation using *AFM* demonstrated that the extended polymer brushes can induce a strong force on approaching solid objects, indicating that the composite material may possess excellent anti-fouling properties, as approaching objects would be prevented from reaching the membrane surface. In addition to anti-fouling properties, the material presents interesting gating applications, where the application of an external electrical stimuli leads to opening and closing of pores. This can be exploited for different applications, such as drug delivery, size-selective separations, and self-cleaning surfaces.

5.5 Appendix

5.5.2 Experimental Results

5.5.2.1 Membrane fabrication

5.5.2.1.1 Polydopamine and initiator deposition

To increase the surface density of the eATRP initiator (CMPS), which requires amine or hydroxyl groups to form bonds with the CMPS chlorine group and anchor the molecule to the surface, DOPA was first deposited onto the CNT surface. DOPA is a mussel-inspired coating that adsorbs non-specifically onto most surfaces.[260] DOPA-deposited membranes turned light brown after the reaction, indicating oxidation and the formation of a DOPA coating (Appendix 5. 1).[261] In our experiments, it was observed that agitation of the polydopamine solution purely by stirring was insufficient to produce membranes with a uniform layer of DOPA (Appendix 5. 1). Membranes coated with DOPA with only stirring as the mixing mechanism formed a thick layer of DOPA only at the top of the membrane, yielding a non-uniform coating. In addition, a longer reaction time was needed for a visible amount of DOPA to be deposited on the membrane (5 h instead of 1 h). To shorten the time for DOPA deposition and polymerization, the solution was continuously bubbled with air that both agitated the solution and facilitated the quick oxidation of DOPA.

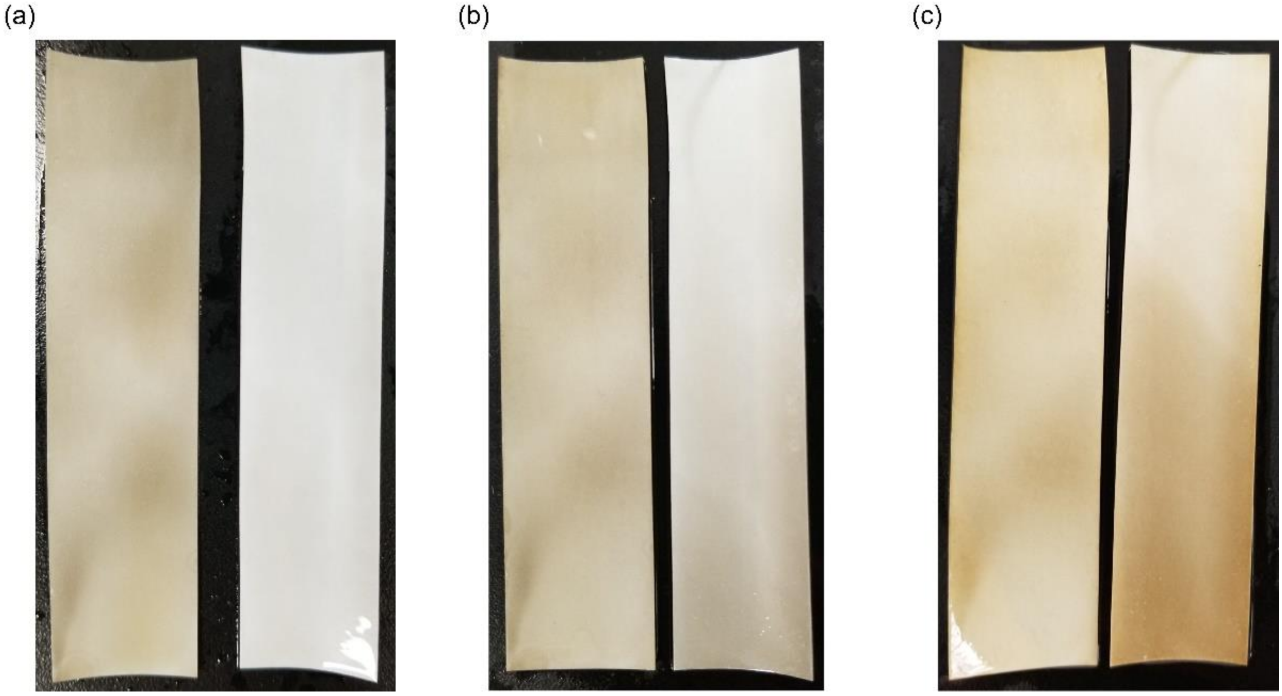

Appendix 5. 1: Comparison of DOPA coating on UF membrane after immersion in bubbled DOPA solution for 1h (left of each picture) and stirred DOPA solution (right of each picture) for (a) 1h, (b) 3h and (c) 5h, shows a gradient DOPA layer and a much longer time required for DOPA coatings agitated only by stirring the solution.

Bare CNTs (i.e., with no DOPA coating) could not provide sufficient binding sites for the initiator, with XPS analysis showing only 0.17 % Cl (an indicator of initiator deposition) on the surface of unmodified CNTs following the CVD of CMPS (Appendix 5. 2); each Cl molecule represents an initiating site for the growth of polymer brushes. In contrast, when DOPA was deposited on the CNTs, followed by CMPS deposition, the percent of Cl groups on the surface increased by more than an order of magnitude, to 2.33 % (Appendix 5. 2The addition of a large number of catechol groups, which are part of DOPA, enabled the high density of initiator deposition. Higher initiator surface densities enable a higher polymer grafting density.[262]

Two methods were evaluated for the deposition of eATRP initiators on the membrane: (1) direct immobilization of BiBB onto COOH-functionalized CNTs (in suspension) followed by pressure deposition of the CNT-immobilized BiBB (BiBB-CNT) on the UF membrane; and, (2) pressure deposition of CNTs on the porous support, followed by DOPA deposition and CMPS immobilization. The first method was not successful, with XPS showing no Br on the pressure-deposited CNTs, and only little Br detected on the BiBB-CNT powder. We speculate that the low initiator numbers on the CNTs is due to the harsh processing conditions needed to form a stable CNT suspension (i.e., sonication and centrifugation), which could dislodge any attached BiBB molecules. To prevent the need for sonication and centrifugation of initiator-coated CNTs, direct deposition of the initiator on a CNT-coated membrane was attempted. However, due to the electrophilic nature of the porous polymeric support used as the substrate for CNT deposition (polysulfone),[263] a suitable aprotic solvent as a carrier for BiBB was difficult to find. As an easier approach, the use of CMPS, a more volatile initiator, allowed for the complete elimination of solvents during the initiator deposition step, by switching to a vapor deposition step. This led to a high surface loading of initiator molecules.

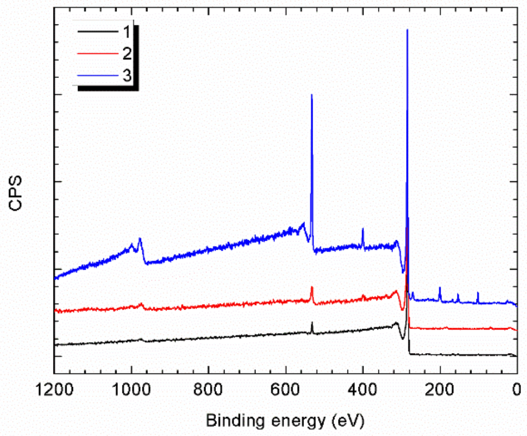

Appendix 5. 2: XPS of (1) CNT modified membrane coated with CMPS, (2) CNT powder immobilized with BiBB, and (3) CNT modified membrane immobilized with DOPA and CMPS.

5.5.2.1.2 Electrochemically mediated atom transfer radical polymerization

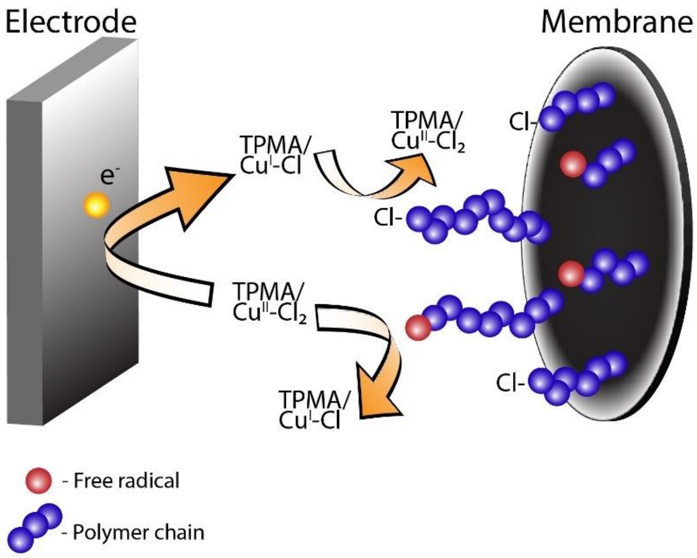

Appendix 5. 3: eATRP reaction process where the activator catalyst (TPMA/CuI-Cl) is generated in situ by reduction of the deactivator catalyst (TPMA/CuII-Cl2) at the electrode interface.

In this study, the eATRP process (Appendix 5. 3) was conducted under potentiostatic conditions at a potential determined using CV.[264] The rate of polymerization (R_p) is a function of monomer concentratin, concentration of dormant chains ($P_n X$), the Cu(I):Cu(II) ratio (Cu(I)/Cu(II)]), the propagation rate constant (k_p) and the ATRP equilibrium constant (K_{ATRP}).[253]

$$R_p = k_p K_{ATRP} \frac{[P_n X][Cu(I)][M]}{[Cu(II)]} \tag{32}$$

Control of the Cu(I):Cu(II) ratio at the electrode surface in a reversible system follows the Nernst equation, given by: [265]

$$E_{app} = E^{o'} - \frac{kT}{ne} ln \frac{[Cu(I)]}{[Cu(II)]} \tag{33}$$

Where E_{app} is the applied potential, and $E^{o'}$ is the formal potential. A high Cu(I) : Cu(II) is produced by when $E_{app} < E^{o'}$The mid-point between the cathodic and anodic peaks gives the half-wave potential, $E^{1/2}$, that can be estimated as $E^{o'}$ in a reversible reaction,[265] with the application of $E^{1/2}$giving a 1:1 ratio of Cu(II):Cu(I) at equilibrium.

In our experiments, we selected pH 10 for the eATRP reaction, due to hydrolysis of the UF support membrane, DOPA, and CMPS at higher pH values. Prior to conducting the experiment, CV curves were obtained using Pt as the working electrode (Appendix 5. 4(a)). The cathodic and anodic peaks obtained from this curve are at -0.294 V and -0.204 V vs Ag/AgCl, respectively. Thus, $E^{1/2}$ is estimated to be -0.249 V, with Pt as the working electrode. To save both time and cost, the working electrode was switched to a stainless-steel plate when driving the eATRP process of growing PAA onto the CNT modified membrane in a relatively large reactor volume (0.35 L). The stainless-steel plate provided a larger electrode surface area for faster reduction of Cu. To compensate for the overpotential of the stainless steel plate compared to Pt, a potential of -0.6 V vs. Ag/AgCl were applied to the working electrode, with a target of Cu(I) : Cu(II) ratio of 0.01. The low Cu(I) : Cu(II) ratio provides better polymerization control due to a lower concentration of propagating free radicals that will be available for radical-radical termination events.[242] Under potentiostatic conditions (-0.6 V vs. Ag/AgCl), there was a rapid current decay in the first 5400 s (Appendix 5. 4), indicating efficient conversion of Cu(II) to Cu(I). Thereafter, a constant current (~2E-4 $mA.cm^{-2}$) was maintained, where the Cu(II) : Cu(I) ratio dictated by equation 1 was reached in the bulk solution. Assuming all charges passed during the potentiostatic experiment were used for the

1-electron reduction of Cu(II) to Cu(I), the final Cu(I) : Cu(II) ratio was 0.0083, which is very close to the targeted 0.01 ratio.

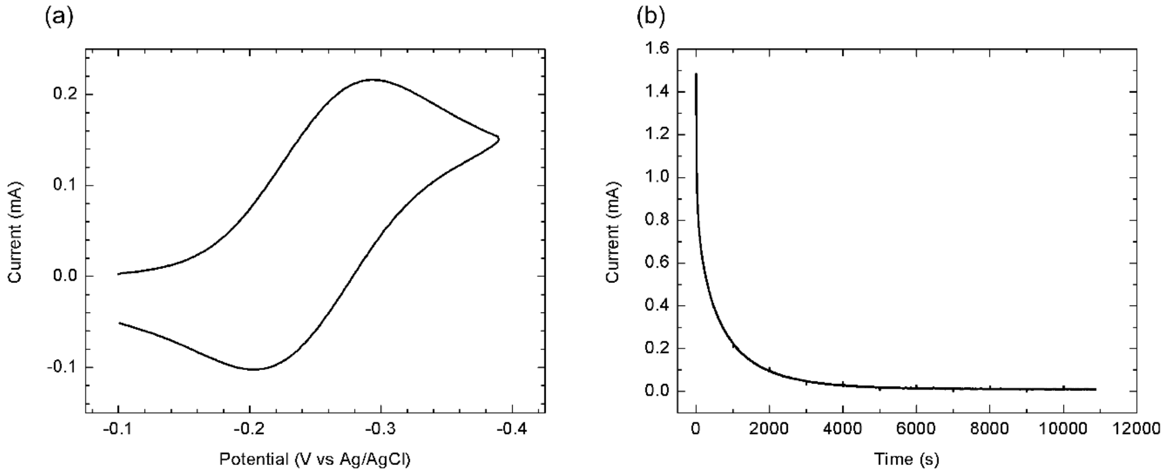

Appendix 5. 4: (a) Cyclic voltammetry of eATRP solution at pH 10, at 293.15 K with 10% acrylic acid, 1mM TPMA and 1mM Cu(II) at a sweep rate of 0.1 V/s. (b) Current drop over time of eATRP experiment at pH 10 with 10% acrylic acid, 1mM TPMA and 1mM Cu(II).

5.5.2.2 Membrane surface characterization

The surface and chemical properties of the membrane surface throughout the fabrication process were determined using a range of characterization techniques. Contact angle (CA) goniometry was used to determine the membrane's hydrophilicity. The static contact angle (with water) of the membrane deposited with CNT-only had a water contact angle of 132^o. After DOPA deposition, the contact angle dropped significantly to 26^o. The addition of CMPS increased the water contact angle to 105^o, that dropped significantly following PAA grafting, to 26^o (Appendix 5. 5(a – d)). This result is not surprising considering the hydrophilic nature of DOPA and the multiple carboxylic acid groups that make up PAA.[266] CNT and CMPS, on the other hand, contains an insignificant amount of hydrogen bond forming groups, leading to the observed elevated hydrophobicity.

FTIR was used to verify the presence of PAA on the modified membrane. The appearance of a peak at 1223 – 1273 cm^{-1} post polymerization corresponds to the presence of C-O bonds on carboxylic acid groups (Appendix 5. 5(d)).[267] In contrast, the CNT-only and CNT-DOPA membranes demonstrated a flat absorption spectrum, with no detectable peaks. It is possible that the DOPA coating does not contain sufficient bonds to be detected by our instrument. Once the CMPS is deposited on the CNT-DOPA material, an absorption peak appeared at 980 – 1178 cm^{-1} that corresponds to Si-O-Si bond stretching.[268] This is consistent with the silanol groups formed by the initiator as they attach to the membrane.

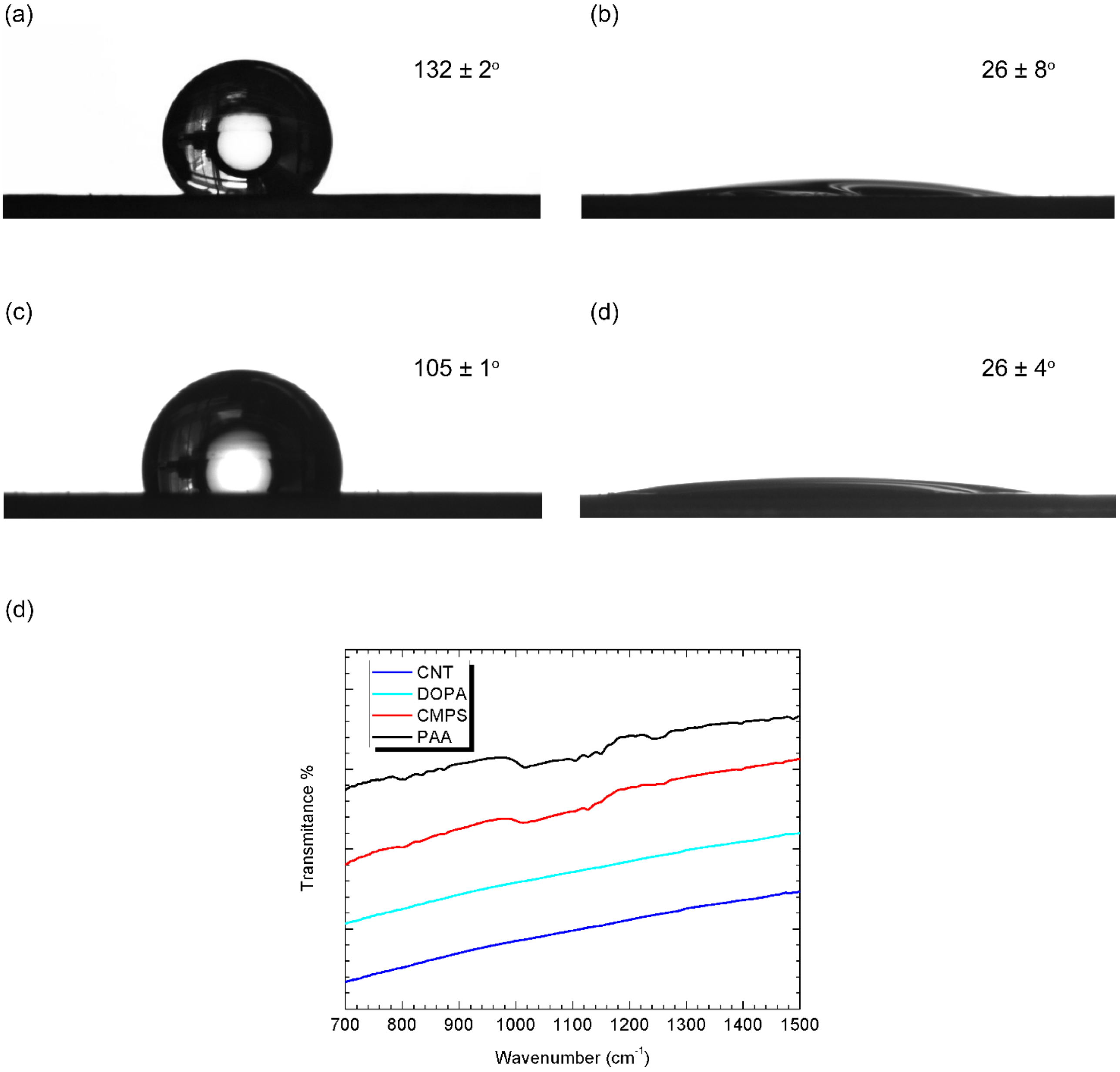

Appendix 5. 5: Water contact angle of (a) CNT-only membrane, (b) DOPA coated membrane, (c) CMPS coated membrane, and (d) PAA-grafted membrane. (e) ATR-FTIR of the membrane at different fabrication stages.

5.5.2.3 Filter paper vs CNT membrane surfaces

It should be noted that the root mean square (RMS) of roughness of filter paper (58.3 nm) is approximately twice that of the deposited CNT layer (30.1 nm), which could result in an increase in PAA dispersivity, and decreased PAA chain length on the filter paper due to differences in catalyst and monomer diffusion towards the two surfaces (Appendix 5. 6).[250]

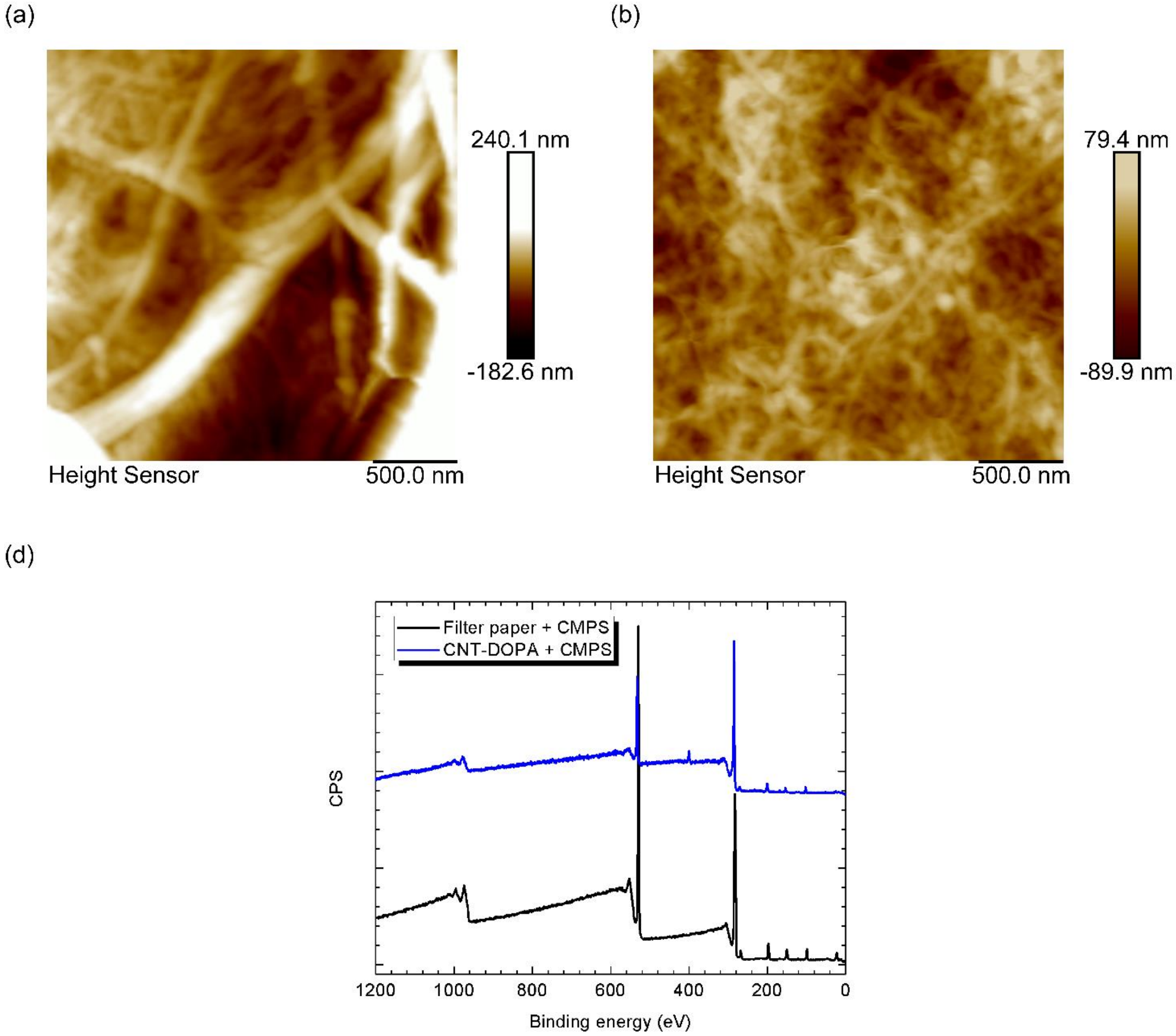

Appendix 5. 6:AFM image of (a) filter paper and (b) CNT deposited membrane (c) XPS spectra of filter paper coated with CMPS, and CNT modified membrane coated with CMPS.

5.5.2.4 Permeability changes at different voltages

PAA-grafted membrane permeability changes at different voltages. When -2 V were applied, the membrane permeability was around 1.8 $Lm^{-2}h^{-1}bar^{-1}$. When no voltage was applied, the permeability increased slightly from 1.8 to 2.2 $Lm^{-2}h^{-1}bar^{-1}$. Application of +2 V was more dramatic, with permeability increasing by around 2 times, to 5.1 $Lm^{-2}h^{-1}bar^{-1}$.

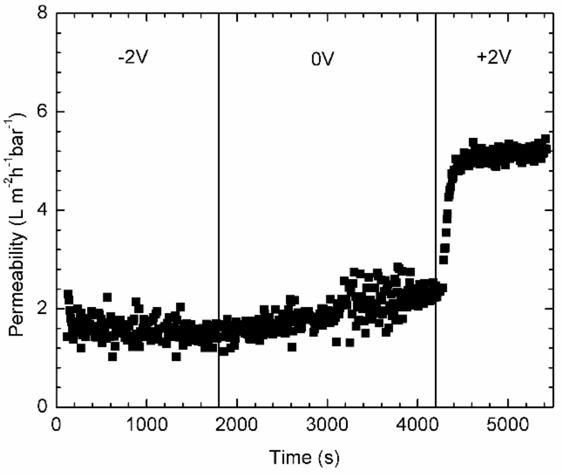

Appendix 5. 7: Permeability changes of PAA-modified membrane at different applied voltages.

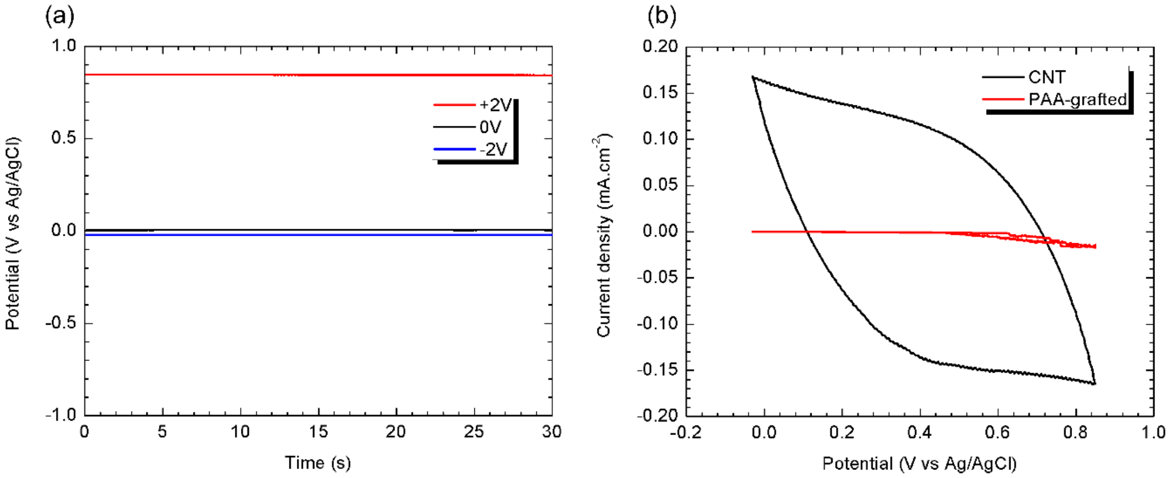

Appendix 5. 8: (a) Open circuit potential test with different voltages applied. (b) Cyclic voltammetry within the actual applied potential region.

6.0 Conclusion

This dissertation presents the utilization of electrochemistry in different water treatment processes, including coagulation and membrane fabrication. In Chapter 1, we discussed the fundamental mechanisms of coagulation and flocculation which can be impacted by pH, coagulant dosage, stirring speeds and ionic strength. Non-conventional coagulants as well as electrocoagulation were also briefly introduced. Next, looked at the fundamentals of membrane classification and transport mechanisms before further bringing the discussion into different types of membranes, namely RO membranes, mixed matrix membranes, and stimuli responsive membranes.

In Chapter 2, we compared the energy consumption and cost of iron coagulants, concluding with EC being more effective in an oily wastewater treatment where high coagulant doses are required. It was also found that EC is cheaper than CC when hauled over long distances due to the additional weight that chemical coagulants carry in the form of hydrated counterions. In Chapter 3, we explored the compositional and morphological changes that happens on aluminium electrodes as EC proceeds at different current densities and flow rates in a PFR configuration. This provided insights into possible energy saving ways to conduct EC in groundwater.

In chapters 4 and 5, we used an electrically conducting membrane formed from a percolating network of carbon nanotubes to create new membrane materials that individually exhibited salt rejection capability, and stimuli-responsiveness to electrical signals. Electropolymerization was successfully employed to form a dense salt-rejecting barrier using aromatic moieties similar to state-of-the-art polyamide membranes. This offers an alternative fabrication technique for the formation of salt rejecting membranes that enables the use of environmentally benign solvents (ie. water) as the polymerization medium. Poly(acrylic acid) brushes grafted from an electrically conducting ultrafiltration membrane was shown to respond to electrical signals by expanding and collapsing. Pore gating was achieved as a result, commanding the passage of 11 kDa particles on the flip of a switch. The response time was rather quick (within 10 minutes) and was attributed to the migration of hydrated counter ions as different voltages are applied to the membrane.

7.0 References

1. Boretti, A. and L. Rosa, *Reassessing the projections of the World Water Development Report.* npj Clean Water, 2019. **2**(1): p. 15.

2. Owa, F.D., *Water Pollution: Sources, Effects, Control and Management.* Mediterranean Journal of Social Sciences, 2013. **4**(8): p. 65.

3. Richardson, S.D., *Water Analysis: Emerging Contaminants and Current Issues.* Analytical Chemistry, 2009. **81**(12): p. 4645-4677.

4. Thai Pin Tan, S.R. *NEWater in Singapore*. 2018 15 Jan 2018 [cited 2021 16 August]; Available from: https://globalwaterforum.org/2018/01/15/newater-in-singapore/.

5. Beysens, D. and I. Milimouk, *The case for alternative fresh water sources.* Pour les resources alternatives en eau, Secheresse, 2000. **11**(4): p. 1-16.

6. Association, N.N.G.W. *Groundwater Use in the U.S.A.* 2020 13 January 2020; Available from: https://www.ngwa.org/docs/default-source/default-document-library/groundwater/usa-groundwater-use-fact-sheet.pdf?sfvrsn=5c7a0db8_4.

7. Robbins, J. *As Water Scarcity Increases, Desalination Plants are on the Rise*. 2019 June 11, 2019 [cited 2021 16 August]; Available from: https://e360.yale.edu/features/as-water-scarcity-increases-desalination-plants-are-on-the-rise.

8. Centers for Disease Control and Prevention, N.C.f.E.a.Z.I.D., Division on Foodborne, Waterborne, and Environmental Diseases. *Water Treatment Community Water Treatment*. 2015 January 20, 2015 [cited 2021 16 August]; Available from: https://www.cdc.gov/healthywater/drinking/public/water_treatment.html.

9. Authority, S.D.C.W. *Seawater Desalination*. 2021 2021 [cited 2021 16 August]; Available from: https://www.sdcwa.org/your-water/local-water-supplies/seawater-desalination/.

10. Jiang, J.-Q., *The role of coagulation in water treatment.* Current Opinion in Chemical Engineering, 2015. **8**: p. 36-44.

11. Ghernaout, D., et al., *Coagulation Process for Removing Algae and Algal Organic Matter—An Overview.* Open Access Library Journal, 2020. **7**(4): p. 1-21.

12. Bratby, J., *Coagulation and flocculation in water and wastewater treatment*. 2016: IWA publishing.

13. Guigui, C., et al., *Impact of coagulation conditions on the in-line coagulation/UF process for drinking water production.* Desalination, 2002. **147**(1): p. 95-100.

14. Xu, H. and L. Guo, *Intriguing changes in molecular size and composition of dissolved organic matter induced by microbial degradation and self-assembly.* Water Research, 2018. **135**: p. 187-194.

15. Tatsi, A., et al., *Coagulation–flocculation pretreatment of sanitary landfill leachates.* Chemosphere, 2003. **53**(7): p. 737-744.

16. Torres, L.G., et al., *Coagulation-flocculation pretreatment of high-load chemical-pharmaceutical industry wastewater: mixing aspects.* Water science and technology, 1997. **36**(2-3): p. 255-262.

17. Suarez, S., J.M. Lema, and F. Omil, *Pre-treatment of hospital wastewater by coagulation–flocculation and flotation.* Bioresource technology, 2009. **100**(7): p. 2138-2146.

18. Di Bella, G., M. Giustra, and G. Freni, *Optimisation of coagulation/flocculation for pre-treatment of high strength and saline wastewater: performance analysis with different coagulant doses.* Chemical Engineering Journal, 2014. **254**: p. 283-292.

19. Aguilar, M.I., et al., *Improvement of coagulation–flocculation process using anionic polyacrylamide as coagulant aid.* Chemosphere, 2005. **58**(1): p. 47-56.

20. Verma, S., B. Prasad, and I.M. Mishra, *Pretreatment of petrochemical wastewater by coagulation and flocculation and the sludge characteristics.* Journal of Hazardous Materials, 2010. **178**(1): p. 1055-1064.

21. Shiva Shankar, Y., et al. *Utilization of Water Treatment Plant (WTP) Sludge for Pretreatment of Dye Wastewater Using Coagulation/Flocculation*. in *Advances in Waste Management*. 2019. Singapore: Springer Singapore.

22. Derjaguin, B. and L. Landau, *Theory of the stability of strongly charged lyophobic sols and of the adhesion of strongly charged particles in solutions of electrolytes.* Progress in Surface Science, 1993. **43**(1-4): p. 30-59.

23. Richens, D.T., *The chemistry of aqua ions: synthesis, structure, and reactivity: a tour through the periodic table of the elements*. 1997: Wiley New York.

24. Duan, J. and J. Gregory, *Coagulation by hydrolysing metal salts.* Advances in Colloid and Interface Science, 2003. **100-102**: p. 475-502.

25. Ives, K.J., *The scientific basis of flocculation*. Vol. 27. 2012: Springer Science & Business Media.

26. Letterman, R., A. Amirtharajah, and C. O'melia, *Coagulation and flocculation.* Water quality and treatment, 1999: p. 6.1-6.66.

27. Pate, K. and P. Safier, *12 - Chemical metrology methods for CMP quality*, in *Advances in Chemical Mechanical Planarization (CMP)*, S. Babu, Editor. 2016, Woodhead Publishing. p. 299-325.

28. Al-Hamadani, Y.A.J., et al., *Application of psyllium husk as coagulant and coagulant aid in semi-aerobic landfill leachate treatment.* Journal of Hazardous Materials, 2011. **190**(1): p. 582-587.

29. Wei, N., et al., *Coagulation behavior of polyaluminum chloride: Effects of pH and coagulant dosage.* Chinese Journal of Chemical Engineering, 2015. **23**(6): p. 1041-1046.

30. Zhang, Z., et al., *Hydrolysis of polyaluminum chloride prior to coagulation: Effects on coagulation behavior and implications for improving coagulation performance.* Journal of Environmental Sciences, 2017. **57**: p. 162-169.

31. Shammas, N.K., *Coagulation and Flocculation*, in *Physicochemical Treatment Processes*, L.K. Wang, Y.-T. Hung, and N.K. Shammas, Editors. 2005, Humana Press: Totowa, NJ. p. 103-139.

32. Kim, S.-H., B.-H. Moon, and H.-I. Lee, *Effects of pH and dosage on pollutant removal and floc structure during coagulation.* Microchemical Journal, 2001. **68**(2): p. 197-203.

33. Wang, Y., et al., *The effect of total hardness and ionic strength on the coagulation performance and kinetics of aluminum salts to remove humic acid.* Chemical Engineering Journal, 2010. **160**(1): p. 150-156.

34. Li, R., et al., *Floc structural characteristics of ferrum-polymer dual-coagulant for treatment of synthetic dyes wastewater: effect of solution pH, hardness and ionic strength.* RSC advances, 2016. **6**(97): p. 94851-94858.

35. Yu, W.-z., et al., *The role of mixing conditions on floc growth, breakage and re-growth.* Chemical Engineering Journal, 2011. **171**(2): p. 425-430.

36. Jarvis, P., et al., *A review of floc strength and breakage.* Water Research, 2005. **39**(14): p. 3121-3137.

37. Yukselen, M.A. and J. Gregory, *The reversibility of floc breakage.* International Journal of Mineral Processing, 2004. **73**(2): p. 251-259.

38. Yu, W., J. Gregory, and L.C. Campos, *Breakage and re-growth of flocs: Effect of additional doses of coagulant species.* Water Research, 2011. **45**(20): p. 6718-6724.

39. Matijević, E., *Colloid stability and complex chemistry.* Journal of Colloid and Interface Science, 1973. **43**(2): p. 217-245.

40. Naceradska, J., L. Pivokonska, and M. Pivokonsky, *On the importance of pH value in coagulation.* Journal of Water Supply: Research and Technology-Aqua, 2019. **68**(3): p. 222-230.

41. Wang, D., et al., *Speciation stability of inorganic polymer flocculant–PACl.* Colloids and Surfaces A: Physicochemical and Engineering Aspects, 2004. **243**(1): p. 1-10.

42. Gao, B.-Y., et al., *Characterization and coagulation of a polyaluminum chloride (PAC) coagulant with high Al13 content.* Journal of Environmental Management, 2005. **76**(2): p. 143-147.

43. Cui, J., et al., *Groundwater arsenic removal by coagulation using ferric(III) sulfate and polyferric sulfate: A comparative and mechanistic study.* Journal of Environmental Sciences, 2015. **32**: p. 42-53.

44. Turunen, J., A. Karppinen, and R. Ihme, *Effectiveness of biopolymer coagulants in agricultural wastewater treatment at two contrasting levels of pollution.* SN Applied Sciences, 2019. **1**(3): p. 210.

45. Qudsieh, I., et al., *Preparation and characterization of a new coagulant based on the sago starch biopolymer and its application in water turbidity removal.* Journal of applied polymer science, 2008. **109**(5): p. 3140-3147.

46. Bhuptawat, H., G.K. Folkard, and S. Chaudhari, *Innovative physico-chemical treatment of wastewater incorporating Moringa oleifera seed coagulant.* Journal of Hazardous Materials, 2007. **142**(1): p. 477-482.

47. Brandt, M.J., et al., *Chapter 12 - Chemical Storage, Dosing and Control*, in *Twort's Water Supply (Seventh Edition)*, M.J. Brandt, et al., Editors. 2017, Butterworth-Heinemann: Boston. p. 513-552.

48. Brandt, M.J., et al., *Chapter 8 - Storage, Clarification and Chemical Treatment*, in *Twort's Water Supply (Seventh Edition)*, M.J. Brandt, et al., Editors. 2017, Butterworth-Heinemann: Boston. p. 323-366.

49. Zhao, X. and Y. Zhang, *Algae-removing and algicidal efficiencies of polydiallyldimethylammonium chloride composite coagulants in enhanced coagulation treatment of algae-containing raw water.* Chemical Engineering Journal, 2011. **173**(1): p. 164-170.

50. Huang, X., et al., *Polyacrylamide as coagulant aid with polytitanium sulfate in humic acid-kaolin water treatment: Effect of dosage and dose method.* Journal of the Taiwan Institute of Chemical Engineers, 2016. **64**: p. 173-179.

51. Mansouri, K., et al., *Anodic Dissolution of Pure Aluminum during Electrocoagulation Process: Influence of Supporting Electrolyte, Initial pH, and Current Density.* Industrial & Engineering Chemistry Research, 2011. **50**(23): p. 13362-13372.

52. Picard, T., et al., *Cathodic dissolution in the electrocoagulation process using aluminium electrodes.* Journal of Environmental Monitoring, 2000. **2**(1): p. 77-80.

53. Khan, S.U., M.S. Mahtab, and I.H. Farooqi, *Enhanced lead (II) removal with low energy consumption in an electrocoagulation column employing concentric electrodes: process optimisation by RSM using CCD.* International Journal of Environmental Analytical Chemistry, 2021: p. 1-18.

54. Malakootian, M. and N. Yousefi, *The efficiency of electrocoagulation process using aluminum electrodes in removal of hardness from water.* Journal of Environmental Health Science & Engineering, 2009. **6**(2): p. 131-136.

55. Tang, X., et al., *Chemical coagulation process for the removal of heavy metals from water: a review.* Desalination and Water Treatment, 2016. **57**(4): p. 1733-1748.

56. Ghosh, D., H. Solanki, and M.K. Purkait, *Removal of Fe(II) from tap water by electrocoagulation technique.* Journal of Hazardous Materials, 2008. **155**(1): p. 135-143.

57. Shahedi, A., et al., *A review on industrial wastewater treatment via electrocoagulation processes.* Current Opinion in Electrochemistry, 2020. **22**: p. 154-169.

58. El-Ashtoukhy, E.S.Z., et al., *Intensification of a new electrocoagulation system characterized by minimum energy consumption and maximum removal efficiency of heavy metals from simulated wastewater.* Chemical Engineering and Processing - Process Intensification, 2020. **154**: p. 108026.

59. Arambarri, J., B. Abbassi, and P. Zytner, *Enhanced removal of phosphorus from wastewater using sequential electrocoagulation and chemical coagulation.* Water, Air, & Soil Pollution, 2019. **230**(12): p. 1-9.

60. Muhammad Niza, N., et al., *Performance of batch electrocoagulation with vibration-induced electrode plates for landfill leachate treatment.* Journal of Water Process Engineering, 2020. **36**: p. 101282.

61. Mechelhoff, M., G.H. Kelsall, and N.J.D. Graham, *Electrochemical behaviour of aluminium in electrocoagulation processes.* Chemical Engineering Science, 2013. **95**: p. 301-312.

62. Harif, T., M. Khai, and A. Adin, *Electrocoagulation versus chemical coagulation: Coagulation/flocculation mechanisms and resulting floc characteristics.* Water Research, 2012. **46**(10): p. 3177-3188.

63. Pendergast, M.M. and E.M. Hoek, *A review of water treatment membrane nanotechnologies.* Energy & Environmental Science, 2011. **4**(6): p. 1946-1971.

64. Wijmans, J.G. and R.W. Baker, *The solution-diffusion model: a review.* Journal of Membrane Science, 1995. **107**(1): p. 1-21.

65. Association, A.W.W., *Microfiltration and Ultrafiltration Membranes for Drinking Water: M53*. Vol. 53. 2005: American Water Works Association.

66. McMordie Stoughton, K., X. Duan, and E.M. Wendel, *Reverse Osmosis Optimization*. 2013, Pacific Northwest National Lab.(PNNL), Richland, WA (United States).

67. Cadotte, J.E., *Interfacially synthesized reverse osmosis membrane*. 1981, Google Patents.

68. Cadotte, J.E., et al., *A new thin-film composite seawater reverse osmosis membrane.* Desalination, 1980. **32**: p. 25-31.

69. Hailemariam, R.H., et al., *Reverse osmosis membrane fabrication and modification technologies and future trends: A review.* Advances in Colloid and Interface Science, 2020. **276**: p. 102100.

70. Yalcinkaya, B., F. Yalcinkaya, and J. Chaloupek, *Thin Film Nanofibrous Composite Membrane for Dead-End Seawater Desalination.* Journal of Nanomaterials, 2016. **2016**: p. 2694373.

71. Gohil, J. and A.K. Suresh, *Performance and Structure of Thin Film Composite Reverse Osmosis Membranes Prepared by Interfacial Polymerization in the Presence of Acid Acceptor.* Journal of Membrane Science and Research, 2019. **5**(1): p. 3-10.

72. Bhave, R., *Inorganic Membranes Synthesis, Characteristics and Applications: Synthesis, characteristics, and applications*. 2012: Springer Science & Business Media.

73. Karimi, A., et al., *High-flux PVDF mixed matrix membranes embedded with size-controlled ZIF-8 nanoparticles.* Separation and Purification Technology, 2019. **229**: p. 115838.

74. Alkindy, M.B., et al., *Synthesis of polyethersulfone (PES)/GO-SiO2 mixed matrix membranes for oily wastewater treatment.* Water Science and Technology, 2020. **81**(7): p. 1354-1364.

75. Qadir, D., H. Mukhtar, and L.K. Keong, *Mixed matrix membranes for water purification applications.* Separation & Purification Reviews, 2017. **46**(1): p. 62-80.

76. Yang, B. and W. Yang, *Thermo-sensitive switching membranes regulated by pore-covering polymer brushes.* Journal of Membrane Science, 2003. **218**(1-2): p. 247-255.

77. Ito, Y., Y.S. Park, and Y. Imanishi, *Visualization of Critical pH-Controlled Gating of a Porous Membrane Grafted with Polyelectrolyte Brushes.* Journal of the American Chemical Society, 1997. **119**(11): p. 2739-2740.

78. Xiang, T., et al., *Ionic-Strength Responsive Zwitterionic Copolymer Hydrogels with Tunable Swelling and Adsorption Behaviors.* Langmuir, 2019. **35**(5): p. 1146-1155.

79. Jeon, G., et al., *Electrically Actuatable Smart Nanoporous Membrane for Pulsatile Drug Release.* Nano Letters, 2011. **11**(3): p. 1284-1288.

80. Neff, J., K. Lee, and E.M. DeBlois, *Produced water: overview of composition, fates, and effects*, in *Produced water*. 2011, Springer. p. 3-54.

81. Veil, J.A., et al., *A white paper describing produced water from production of crude oil, natural gas, and coal bed methane*. 2004, Argonne National Lab., IL (US).

82. Duraisamy, R.T., A.H. Beni, and A. Henni, *State of the art treatment of produced water.* Water Treatment, 2013: p. 199-222.

83. J. Wang, A.D.H., S. Bhattacharjee, A. Edalat, *Produced Water Management in Upstream Oil and Gas Production*, ed. E.M.V. Hoek. 2020: Morgan & Claypool Publishers.

84. Scanlon, B.R., et al., *Water Issues Related to Transitioning from Conventional to Unconventional Oil Production in the Permian Basin.* Environmental Science & Technology, 2017. **51**(18): p. 10903-10912.

85. Crittenden, J.C., et al., *Water Treatment: Principles and Design*. Second ed. 2005, Hoboken, New Jersey: John Wiley & Sons, Inc.

86. Canizares, P., et al., *Coagulation and electrocoagulation of oil-in-water emulsions.* Journal of Hazardous Materials, 2008. **151**(1): p. 44-51.

87. Canizares, P., et al., *Break-up of oil-in-water emulsions by electrochemical techniques.* Journal of Hazardous Materials, 2007. **145**(1-2): p. 233-240.

88. Changmai, M., M. Pasawan, and M.K. Purkait, *Treatment of oily wastewater from drilling site using electrocoagulation followed by microfiltration.* Separation and Purification Technology, 2019. **210**: p. 463-472.

89. Adhoum, N., *Decolourization and removal of phenolic compounds from olive mill wastewater by electrocoagulation.* Chemical Engineering and Processing, 2004. **43**(10): p. 1281-1287.

90. Flores, N., et al., *Treatment of olive oil mill wastewater by single electrocoagulation with different electrodes and sequential electrocoagulation/electrochemical Fenton-based processes.* Journal of Hazardous Materials, 2018. **347**: p. 58-66.

91. Kobya, M., M. Bayramoglu, and M. Eyvaz, *Techno-economical evaluation of electrocoagulation for the textile wastewater using different electrode connections.* Journal of hazardous materials, 2007. **148**(1-2): p. 311-318.

92. Papadopoulos, K.P., et al., *Treatment of printing ink wastewater using electrocoagulation.* Journal of Environmental Management, 2019. **237**: p. 442-448.

93. García-García, P., et al., *Treatment of wastewaters from the green table olive packaging industry using electro-coagulation.* Chemical Engineering Journal, 2011. **170**: p. 59-66.

94. Chen, G.H., X.M. Chen, and P.L. Yue, *Electrocoagulation and electroflotation of restaurant wastewater.* Journal of Environmental Engineering-Asce, 2000. **126**(9): p. 858-863.

95. Baran, W., et al., *Removal of veterinary antibiotics from wastewater by electrocoagulation.* Chemosphere, 2018. **194**: p. 381-389.

96. Al-Qodah, Z. and M. Al-Shannag, *Heavy metal ions removal from wastewater using electrocoagulation processes: A comprehensive review.* Separation Science and Technology, 2017. **52**(17): p. 2649-2676.

97. Kim, M.-K., et al., *Degradation mechanism of perfluorooctanoic acid (PFOA) during electrocoagulation using Fe electrode.* Separation and Purification Technology, 2020. **247**: p. 116911.

98. Xu, X. and X. Zhu, *Treatment of refectory oily wastewater by electro-coagulation process.* Chemosphere, 2004. **56**(10): p. 889-894.

99. Rossini, M., J.G. Garrido, and M. Galluzzo, *Optimization of the coagulation-flocculation treatment: influence of rapid mix parameters.* Water Research, 1999. **33**(8): p. 1817-1826.

100. Chawaloesphonsiya, N., P. Guiraud, and P. Painmanakul, *Analysis of cutting-oil emulsion destabilization by aluminum sulfate.* Environmental Technology, 2018. **39**(11): p. 1450-1460.

101. Mollah, M.Y.A., et al., *Electrocoagulation (EC) — science and applications.* Journal of Hazardous Materials, 2001. **84**(1): p. 29-41.

102. Garcia-Segura, S., et al., *Electrocoagulation and advanced electrocoagulation processes: A general review about the fundamentals, emerging applications and its association with other technologies.* Journal of Electroanalytical Chemistry, 2017. **801**: p. 267-299.

103. Mollah, M., et al., *Fundamentals, present and future perspectives of electrocoagulation.* Journal of Hazardous Materials, 2004. **114**(1-3): p. 199-210.

104. Moussa, D.T., et al., *A comprehensive review of electrocoagulation for water treatment: Potentials and challenges.* Journal of Environmental Management, 2017. **186**: p. 24-41.

105. Elazzouzi, M., K. Haboubi, and M.S. Elyoubi, *Electrocoagulation flocculation as a low-cost process for pollutants removal from urban wastewater.* Chemical Engineering Research and Design, 2017. **117**: p. 614-626.

106. Cañizares, P., et al., *Technical and economic comparison of conventional and electrochemical coagulation processes.* Journal of Chemical Technology & Biotechnology, 2009. **84**(5): p. 702-710.

107. Phalakornkule, C., et al., *Pretreatment of palm oil mill effluent by electrocoagulation and coagulation.* Scienceasia, 2010. **36**(2): p. 142-149.

108. An, C., et al., *Emerging usage of electrocoagulation technology for oil removal from wastewater: A review.* Science of The Total Environment, 2017. **579**: p. 537-556.

109. Bayramoglu, M., M. Eyvaz, and M. Kobya, *Treatment of the textile wastewater by electrocoagulation: economical evaluation.* Chemical Engineering Journal, 2007. **128**(2-3): p. 155-161.

110. Syam Babu, D., et al., *Industrial wastewater treatment by electrocoagulation process.* Separation Science and Technology, 2020. **55**(17): p. 3195-3227.

111. Subramani, A., et al., *Recovery optimization of membrane processes for treatment of produced water with high silica content.* Desalination and Water Treatment, 2011. **36**(1-3): p. 297-309.

112. Ju, H., et al., *Crosslinked poly (ethylene oxide) fouling resistant coating materials for oil/water separation.* Journal of Membrane Science, 2008. **307**(2): p. 260-267.

113. Beyaz, A., W.S. Oh, and V.P. Reddy, *Ionic liquids as modulators of the critical micelle concentration of sodium dodecyl sulfate.* Colloids and Surfaces B: Biointerfaces, 2004. **35**(2): p. 119-124.

114. European Commission, J.R.C., Institute for Prospective Technological Studies, *Additional Information submitted during the information exchange on Large Volume Inorganic Chemicals –Solid and Others Industry*. 2005: Seville, SPAIN.

115. Kristensen, H.O., *Cargo Transport by Sea and Road — Technical and Economical Environmental Factors.* Naval Engineers Journal, 2006. **118**(3): p. 115-129.

116. Martelaro, N. *Energy Use in US Steel Manufacturing*. 2016; Available from: http://large.stanford.edu/courses/2016/ph240/martelaro1/.

117. Alibaba. *96% Ferric Chloride Industrial grade, Ferric Chloride FeCL3 Price* 2020; Available from: https://www.alibaba.com/product-detail/96-Ferric-Chloride-Industrial-grade-Ferric_62326896646.html?spm=a2700.7724857.normalList.33.bb3044a6KnK7Ue.

118. Alibaba. *Poly Ferric Sulfate High Quality Low Price water treatment chemical* 2020; Available from: https://www.alibaba.com/product-detail/Poly-Ferric-Sulfate-High-Quality-Low_62336601744.html?spm=a2700.7724857.normalList.56.64142b95R16a6S&bypass=true.

119. Alibaba. *High Quality Foundry Steel Grade Pig Iron* 2020; Available from: https://www.alibaba.com/product-detail/High-Quality-Foundry-Steel-Grade-Pig_62010905759.html?spm=a2700.galleryofferlist.0.0.62366a6aGSlgkl&bypass=true.

120. Choice, E. *Find the best electric rate in your area for your home or business:*. 2020; Available from: https://www.electricchoice.com/electricity-prices-by-state/.

121. Austin, D., *Pricing freight transport to account for external costs.* Congressional Budget, 2015.

122. Water, A.D.o.E.C.D.o., *Listing Methodology for Determining Water Quality Impairments from Turbidity*. 2016.

123. Agency, U.S.E.P., *The NPDES general permit for new and existing sources and new dischargers in the offshore subcategory of the oil and gas extraction point source category for the western portion of the outer continental shelf of the gulf of mexico (GMG290000)* 2017.

124. Holt, P.K., et al., *A quantitative comparison between chemical dosing and electrocoagulation.* Colloids and Surfaces A: Physicochemical and Engineering Aspects, 2002. **211**(2-3): p. 233-248.

125. Phalakornkule, C., et al., *Pretreatment of palm oil mill effluent by electrocoagulation and coagulation.* Science Asia, 2010. **36**(2): p. 142-149.

126. Canizares, P., et al., *Coagulation and electrocoagulation of oil-in-water emulsions.* Journal of Hazardous Materials, 2008. **151**(1): p. 44-51.

127. Busscher, H.J., B. van de Belt-Gritter, and H.C. van der Mei, *Implications of microbial adhesion to hydrocarbons for evaluating cell surface hydrophobicity 1. Zeta potentials of hydrocarbon droplets.* Colloids and Surfaces B: Biointerfaces, 1995. **5**(3): p. 111-116.

128. Júnior, J.A.A. and J.B. Baldo, *The behavior of zeta potential of silica suspensions.* New Journal of Glass and Ceramics, 2014. **4**(02): p. 29.

129. Poh, P.E., et al., *Investigation on micro-bubble flotation and coagulation for the treatment of anaerobically treated palm oil mill effluent (POME).* Journal of Environmental Chemical Engineering, 2014. **2**(2): p. 1174-1181.

130. Niquette, P., et al., *Impacts of substituting aluminum-based coagulants in drinking water treatment.* Water Quality Research Journal, 2004. **39**(3): p. 303-310.

131. Afonso, M.D., J.O. Jaber, and M.S. Mohsen, *Brackish groundwater treatment by reverse osmosis in Jordan.* Desalination, 2004. **164**(2): p. 157-171.

132. Sang, Y., et al., *Heavy metal-contaminated groundwater treatment by a novel nanofiber membrane.* Desalination, 2008. **223**(1): p. 349-360.

133. Khor, C.M., et al., *Electrically Mediated Membrane Pore Gating via Grafted Polymer Brushes.* ACS Materials Letters, 2019. **1**(6): p. 647-654.

134. Belkacem, M., S. Bekhti, and K. Bensadok, *Groundwater treatment by reverse osmosis.* Desalination, 2007. **206**(1-3): p. 100-106.

135. Rao, U., et al., *Mineral scale prevention on electrically conducting membrane distillation membranes using induced electrophoretic mixing.* Environmental science & technology, 2020. **54**(6): p. 3678-3690.

136. Zhu, X., et al., *Field-induced redistribution of surfactants at the oil/water interface reduces membrane fouling on electrically conducting carbon nanotube UF membranes.* Environmental science & technology, 2018. **52**(20): p. 11591-11600.

137. Long, Y., et al., *Synergistic fouling behaviors and mechanisms of calcium ions and polyaluminum chloride associated with alginate solution in coagulation-ultrafiltration (UF) process.* Water Research, 2021. **189**: p. 116665.

138. Ohno, K., et al., *NF membrane fouling by aluminum and iron coagulant residuals after coagulation–MF pretreatment.* Desalination, 2010. **254**(1): p. 17-22.

139. Deka, B.J., et al., *Emerging investigator series: control of membrane fouling by dissolved algal organic matter using pre-oxidation with coagulation as seawater pretreatment.* Environmental Science: Water Research & Technology, 2020. **6**(4): p. 935-944.

140. Edzwald, J., *Coagulation in drinking water treatment: particles, organics and coagulants.* Water Science and Technology, 1993. **27**(11): p. 21-35.

141. Chen, S., T. Chang, and C. Lin, *Silica pretreatment for a RO brackish water source with high magnesium.* Water Science and Technology: Water Supply, 2006. **6**(4): p. 179-187.

142. Feng, L., et al., *Coagulation performance and membrane fouling of different aluminum species during coagulation/ultrafiltration combined process.* Chemical Engineering Journal, 2015. **262**: p. 1161-1167.

143. Amran, A.H., et al., *Effectiveness of natural coagulant in coagulation process: a review.* International Journal of Engineering & Technology, 2018. **7**(3.9): p. 34-37.

144. Song, Z., C.J. Williams, and R.G.J. Edyvean, *Treatment of tannery wastewater by chemical coagulation.* Desalination, 2004. **164**(3): p. 249-259.

145. Alexander, J.T., F.I. Hai, and T.M. Al-aboud, *Chemical coagulation-based processes for trace organic contaminant removal: Current state and future potential.* Journal of Environmental Management, 2012. **111**: p. 195-207.

146. Lacasa, E., et al., *Removal of nitrates from groundwater by electrocoagulation.* Chemical Engineering Journal, 2011. **171**(3): p. 1012-1017.

147. Ali, I., T.A. Khan, and M. Asim, *Removal of arsenate from groundwater by electrocoagulation method.* Environmental Science and Pollution Research, 2012. **19**(5): p. 1668-1676.

148. Iddya, A., et al., *Efficient ammonia recovery from wastewater using electrically conducting gas stripping membranes.* Environmental Science: Nano, 2020. **7**(6): p. 1759-1771.

149. Hamdan, S.S. and M.H. El-Naas, *Characterization of the removal of Chromium (VI) from groundwater by electrocoagulation.* Journal of Industrial and Engineering Chemistry, 2014. **20**(5): p. 2775-2781.

150. Moussavi, G., R. Khosravi, and M. Farzadkia, *Removal of petroleum hydrocarbons from contaminated groundwater using an electrocoagulation process: Batch and continuous experiments.* Desalination, 2011. **278**(1): p. 288-294.

151. FENG, Q.-y., et al., *Removal of humic acid from groundwater by electrocoagulation.* Journal of China University of Mining and Technology, 2007. **17**(4): p. 513-520.

152. Bao, J., et al., *Removal of perfluoroalkanesulfonic acids (PFSAs) from synthetic and natural groundwater by electrocoagulation.* Chemosphere, 2020. **248**: p. 125951.

153. Mahmad, M.K.N., et al., *Electrocoagulation Process by Using Aluminium and Stainless Steel Electrodes to Treat Total Chromium, Colour and Turbidity.* Procedia Chemistry, 2016. **19**: p. 681-686.

154. Dubrawski, K.L., M. Fauvel, and M. Mohseni, *Metal type and natural organic matter source for direct filtration electrocoagulation of drinking water.* Journal of Hazardous Materials, 2013. **244-245**: p. 135-141.

155. KALIVEL, P., V. MOSES, and J. PALANICHAMY, *OPTIMIZATION OF COLOR REMOVAL OF BLUE SI DYE SOLUTION WITH Al-Al, Cu-Cu ELECTRODES IN ELECTROCOAGULATION PROCESS USING STATISTICAL MODELLING.*

156. Millar, G.J., et al., *Evaluation of electrocoagulation for the pre-treatment of coal seam water.* Journal of Water Process Engineering, 2014. **4**: p. 166-178.

157. Khor, C.M., et al., *Performance, Energy and Cost of Produced Water Treatment by Chemical and Electrochemical Coagulation.* Water, 2020. **12**(12): p. 3426.

158. Demirbas, E. and M. Kobya, *Operating cost and treatment of metalworking fluid wastewater by chemical coagulation and electrocoagulation processes.* Process Safety and Environmental Protection, 2017. **105**: p. 79-90.

159. Hashim, K.S., et al., *Iron removal, energy consumption and operating cost of electrocoagulation of drinking water using a new flow column reactor.* Journal of Environmental Management, 2017. **189**: p. 98-108.

160. Tahreen, A., M.S. Jami, and F. Ali, *Role of electrocoagulation in wastewater treatment: A developmental review.* Journal of Water Process Engineering, 2020. **37**: p. 101440.

161. Vik, E.A., et al., *Electrocoagulation of potable water.* Water Research, 1984. **18**(11): p. 1355-1360.

162. Pyun, S.-I. and S.-M. Moon, *Corrosion mechanism of pure aluminium in aqueous alkaline solution.* Journal of Solid State Electrochemistry, 2000. **4**(5): p. 267-272.

163. Venkatasubramanian, G., S. Mideen, and A.K. Jha, *Effect of pH on the corrosion behavior of aluminium alloy welded plate in chloride solutions.* Research Journal of Chemical Sciences ____ ISSN, 2013. **2231**: p. 606X.

164. Zhang, J., M. Klasky, and B.C. Letellier, *The aluminum chemistry and corrosion in alkaline solutions.* Journal of Nuclear Materials, 2009. **384**(2): p. 175-189.

165. Vargel, C., *Corrosion of aluminium*. 2020: Elsevier.

166. Perrault, G., *The role of hydrides in the equilibrium of aluminum in aqueous solutions.* Journal of the Electrochemical Society, 1979. **126**(2): p. 199.

167. McMaster-Carr. *Polished Easy-to-Weld 5052 Aluminum*. 2021 [cited 2021 7/19]; Available from: https://www.mcmaster.com/8199K106/.

168. Donatus, U., et al., *Corrosion pathways in aluminium alloys.* Transactions of Nonferrous Metals Society of China, 2017. **27**(1): p. 55-62.

169. Tabrizi, M.R., et al., *The long-term corrosion of aluminium in alkaline media.* Corrosion Science, 1991. **32**(7): p. 733-742.

170. Armstrong, R. and V. Braham, *The mechanism of aluminium corrosion in alkaline solutions.* Corrosion Science, 1996. **38**(9): p. 1463-1471.

171. Reboul, M., et al., *A ten step mechanism for the pitting corrosion of aluminium alloys.* Corrosion Reviews, 1997. **15**(3-4): p. 471-496.

172. Mechelhoff, M., G.H. Kelsall, and N.J. Graham, *Electrochemical behaviour of aluminium in electrocoagulation processes.* Chemical Engineering Science, 2013. **95**: p. 301-312.

173. Xhanari, K. and M. Finšgar, *Organic corrosion inhibitors for aluminum and its alloys in chloride and alkaline solutions: A review.* Arabian Journal of Chemistry, 2019. **12**(8): p. 4646-4663.

174. MacLeod, I.D., *Stabilization of corroded aluminium.* Studies in Conservation, 1983. **28**(1): p. 1-7.

175. Mehta, S.K., A. Kalsotra, and M. Murat, *A new approach to phase transformations in gibbsite: the role of the crystallinity.* Thermochimica Acta, 1992. **205**: p. 191-203.

176. Wilsdorf, H., *Structure of amorphous aluminium oxide films.* Nature, 1951. **168**(4275): p. 600-601.

177. Cimpoeşu, N., et al., *Electrochemical Characterization of a New Biodegradable FeMnSi Alloy Coated with Hydroxyapatite-Zirconia by PLD Technique.* Journal of Chemistry, 2016. **2016**: p. 9520972.

178. Deepa, P. and R. Padmalatha, *Corrosion behaviour of 6063 aluminium alloy in acidic and in alkaline media.* Arabian Journal of chemistry, 2017. **10**: p. S2234-S2244.

179. Zelinsky, A. and B.Y. Pirogov, *Effective thickness of the diffusion layer during hydrogen ion reduction in aqueous hydrochloric acid solutions.* Russian Journal of Electrochemistry, 2008. **44**(5): p. 585-593.

180. Allen, J.B. and R.F. Larry, *Electrochemical methods fundamentals and applications*. 2001: John Wiley & Sons.

181. Harris, K.R. and L.A. Woolf, *Pressure and temperature dependence of the self diffusion coefficient of water and oxygen-18 water.* Journal of the Chemical Society, Faraday Transactions 1: Physical Chemistry in Condensed Phases, 1980. **76**: p. 377-385.

182. Ribeiro, A.C.F., et al., *Diffusion coefficients of aluminium chloride in aqueous solutions at 298.15, 303.15 and 315.15K.* Electrochimica Acta, 2007. **52**(23): p. 6450-6455.

183. Yuan, X.-Z., et al., *EIS equivalent circuits.* Electrochemical Impedance Spectroscopy in PEM Fuel Cells: Fundamentals and Applications, 2010: p. 139-192.

184. Gileadi, E. and E. Kirowa-Eisner, *Some observations concerning the Tafel equation and its relevance to charge transfer in corrosion.* Corrosion Science, 2005. **47**(12): p. 3068-3085.

185. Scott, K., *Electrochemical principles and characterization of bioelectrochemical systems*, in *Microbial Electrochemical and Fuel Cells*. 2016, Elsevier. p. 29-66.

186. Khan, S.U.M., R.C. Kainthla, and J.O.M. Bockris, *The redox potential and the Fermi level in solution.* The Journal of Physical Chemistry, 1987. **91**(23): p. 5974-5977.

187. Lee, K.P., T.C. Arnot, and D. Mattia, *A review of reverse osmosis membrane materials for desalination—Development to date and future potential.* Journal of Membrane Science, 2011. **370**(1): p. 1-22.

188. Spencer, P.S. and H.H. Schaumburg, *Organic solvent neurotoxicity: Facts and research needs.* Scandinavian journal of work, environment & health, 1985: p. 53-60.

189. Arlien-Soborg, P., *Solvent neurotoxicity*. 1991: CRC Press.

190. Kohlbrand, H.T., *Case history of a deflagration involving an organic solvent/oxygen system below its flash point.* Plant/Operations Progress, 1991. **10**(1): p. 52-54.

191. Liaw, H.J., *The maximum flammable content for binary aqueous–organic mixtures not to flash and their maximum flash points.* AIChE Journal, 2018. **64**(1): p. 263-271.

192. Baker, E.L., *Organic solvent neurotoxicity.* Annual review of public health, 1988. **9**(1): p. 223-232.

193. Huo, X., et al., *Study on flash-point measurement and reduced prediction model for ternary extraction system.* Process Safety and Environmental Protection, 2020. **138**: p. 99-107.

194. Lee, S., et al., *A case of acute organic solvent poisoning during epoxy coating.* aoem, 2019. **31**(1): p. 0-0.

195. Cherry, N., T. McArthy, and H. Waldron, *Solvent sniffing in industry.* Human toxicology, 1982. **1**(3): p. 289-292.

196. Scott, A. *Explosion in Leverkusen kills at least 2*. 2021 28 July 2021 [cited 2021 26 August 2021]; German accident traced to organic solvents in waste processing center]. Available from: https://cen.acs.org/safety/industrial-safety/Explosion-Leverkusen-kills-least-2/99/i28.

197. Seo, S. and J. Kim, *An aggravated return-to-work case of organic solvent induced chronic toxic encephalopathy.* Annals of occupational and environmental medicine, 2018. **30**(1): p. 1-6.

198. Panizza, M., C. Bocca, and G. Cerisola, *Electrochemical treatment of wastewater containing polyaromatic organic pollutants.* Water Research, 2000. **34**(9): p. 2601-2605.

199. Zhou, Z., et al., *Electropolymerization of robust conjugated microporous polymer membranes for rapid solvent transport and narrow molecular sieving.* Nature Communications, 2020. **11**(1): p. 5323.

200. Zhang, M., et al., *Electropolymerization of Molecular‐Sieving Polythiophene Membranes for H2 Separation.* Angewandte Chemie, 2019. **131**(26): p. 8860-8864.

201. Guerrieri, A., R. Ciriello, and D. Centonze, *Permselective and enzyme-entrapping behaviours of an electropolymerized, non-conducting, poly(o-aminophenol) thin film-modified electrode: A critical study.* Biosensors and Bioelectronics, 2009. **24**(6): p. 1550-1556.

202. Dudchenko, A.V., et al., *Organic fouling inhibition on electrically conducting carbon nanotube–polyvinyl alcohol composite ultrafiltration membranes.* Journal of Membrane Science, 2014. **468**: p. 1-10.

203. Zhu, X., et al., *Surfactant-stabilized oil separation from water using ultrafiltration and nanofiltration.* Journal of Membrane Science, 2017. **529**: p. 159-169.

204. Duan, W., et al., *Polyaniline-Coated Carbon Nanotube Ultrafiltration Membranes: Enhanced Anodic Stability for In Situ Cleaning and Electro-Oxidation Processes.* ACS Applied Materials & Interfaces, 2016. **8**(34): p. 22574-22584.

205. Nady, H., M.M. El-Rabiei, and G.M.A. El-Hafez, *Electrochemical oxidation behavior of some hazardous phenolic compounds in acidic solution.* Egyptian Journal of Petroleum, 2017. **26**(3): p. 669-678.

206. Kyeremateng, N.A., et al., *Electropolymerization of copolymer electrolyte into titania nanotube electrodes for high-performance 3D microbatteries.* Electrochemistry Communications, 2011. **13**(8): p. 894-897.

207. Hsieh, M.-T. and T.-J. Whang, *Mechanistic investigation on the electropolymerization of phenol red by cyclic voltammetry and the catalytic reactions toward acetaminophen and dopamine using poly(phenol red)-modified GCE.* Journal of Electroanalytical Chemistry, 2017. **795**: p. 130-140.

208. Gattrell, M. and D. Kirk, *A Fourier Transform Infrared Spectroscopy Study of the Passive Film Produced during Aqueous Acidic Phenol Electro -oxidation.* Journal of The Electrochemical Society, 1992. **139**(10): p. 2736.

209. Eddy, S., et al., *The modification of enzyme electrode properties with non-conducting electropolymerised films.* Biosensors and Bioelectronics, 1995. **10**(9-10): p. 831-839.

210. Filipović, M., et al., *QSAR of the free radical scavenging potency of selected hydroxybenzoic acids and simple phenolics.* Comptes Rendus Chimie, 2015. **18**(5): p. 492-498.

211. Thavasi, V., L.P. Leong, and R.P.A. Bettens, *Investigation of the influence of hydroxy groups on the radical scavenging ability of polyphenols.* The journal of physical chemistry A, 2006. **110**(14): p. 4918-4923.

212. Kobayashi, S. and H. Higashimura, *Oxidative polymerization of phenols revisited.* Progress in Polymer Science, 2003. **28**(6): p. 1015-1048.

213. Chevali, V. and E. Kandare, *13 - Rigid biofoam composites as eco-efficient construction materials*, in *Biopolymers and Biotech Admixtures for Eco-Efficient Construction Materials*, F. Pacheco-Torgal, et al., Editors. 2016, Woodhead Publishing. p. 275-304.

214. Yao, Y., et al., *High performance polyester reverse osmosis desalination membrane with chlorine resistance.* Nature Sustainability, 2020: p. 1-9.

215. Asmatulu, R. and W.S. Khan, *Chapter 13 - Characterization of electrospun nanofibers*, in *Synthesis and Applications of Electrospun Nanofibers*, R. Asmatulu and W.S. Khan, Editors. 2019, Elsevier. p. 257-281.

216. Joshi, R., T.K. Ghanty, and T. Mukherjee, *Substituent effect on ionization potential, O–H bond dissociation energy and intra-molecular hydrogen bonding in salicylic acid derivatives.* Journal of Molecular Structure: THEOCHEM, 2010. **948**(1): p. 47-54.

217. Strathmann, H., *Membrane separation processes: current relevance and future opportunities.* AIChE journal, 2001. **47**(5): p. 1077-1087.

218. Ravanchi, M.T., T. Kaghazchi, and A. Kargari, *Application of membrane separation processes in petrochemical industry: a review.* Desalination, 2009. **235**(1-3): p. 199-244.

219. Gracheva, M.E., J. Vidal, and J.-P. Leburton, *p−n Semiconductor Membrane for Electrically Tunable Ion Current Rectification and Filtering.* Nano Letters, 2007. **7**(6): p. 1717-1722.

220. Rao, U., et al., *Coupling hydrothermal liquefaction and membrane distillation to treat anaerobic digestate from food and dairy farm waste.* Bioresource Technology, 2018. **267**: p. 408-415.

221. Ronen, A., L. Walker Sharon, and D. Jassby, *Electroconductive and electroresponsive membranes for water treatment*, in *Reviews in Chemical Engineering*. 2016. p. 533.

222. Liu, Z., et al., *Stimuli-responsive smart gating membranes.* Chemical Society Reviews, 2016. **45**(3): p. 460-475.

223. Jassby, D., T.Y. Cath, and H. Buisson, *The role of nanotechnology in industrial water treatment.* Nature Nanotechnology, 2018. **13**(8): p. 670-672.

224. Cross, M.C., R.G. Toomey, and N.D. Gallant, *Protein-surface interactions on stimuli-responsive polymeric biomaterials.* Biomedical Materials, 2016. **11**(2): p. 022002.

225. Du, L., et al., *Electro-responsive carbon membranes with reversible superhydrophobicity/superhydrophilicity switch for efficient oil/water separation.* Separation and Purification Technology, 2019. **210**: p. 891-899.

226. Zhu, X. and D. Jassby, *Electroactive Membranes for Water Treatment: Enhanced Treatment Functionalities, Energy Considerations, and Future Challenges.* Accounts of Chemical Research, 2019. **52**(5): p. 1177-1186.

227. Wang, D., et al., *Stimuli-Responsive Fluorescent Poly(N-isopropylacrylamide) Microgels Labeled with Phenylboronic Acid Moieties as Multifunctional Ratiometric Probes for Glucose and Temperatures.* Macromolecules, 2011. **44**(7): p. 2282-2290.

228. Mura, S., J. Nicolas, and P. Couvreur, *Stimuli-responsive nanocarriers for drug delivery.* Nature Materials, 2013. **12**: p. 991.

229. Stuart, M.A.C., et al., *Emerging applications of stimuli-responsive polymer materials.* Nature Materials, 2010. **9**: p. 101.

230. Swift, T., et al., *The pH-responsive behaviour of poly (acrylic acid) in aqueous solution is dependent on molar mass.* Soft Matter, 2016. **12**(9): p. 2542-2549.

231. Roodenko, K., et al., *Ultrathin responsive polyelectrolyte brushes studied by infrared synchrotron mapping ellipsometry.* Applied Physics Letters, 2008. **92**: p. 103102-103102.

232. Bouckaert, S. and J.P. REMON, *In‐vitro Bioadhesion of a Buccal, Miconazole Slow‐release Tablet.* Journal of pharmacy and pharmacology, 1993. **45**(6): p. 504-507.

233. Tian, B., et al., *pH-responsive poly (acrylic acid)-gated mesoporous silica and its application in oral colon targeted drug delivery for doxorubicin.* Colloids and Surfaces B: Biointerfaces, 2017. **154**: p. 287-296.

234. Chu, L.-Y., et al., *Control of pore size and permeability of a glucose-responsive gating membrane for insulin delivery.* Journal of Controlled Release, 2004. **97**(1): p. 43-53.

235. Yamauchi, T., E. Kokufuta, and Y. Osada, *Electrically controlled protein permeation through a poly(vinyl alcohol)/poly(acrylic acid) composite membrane.* Polymer Gels and Networks, 1993. **1**(4): p. 247-255.

236. Chen, T., et al., *Stimulus-responsive polymer brushes on surfaces: Transduction mechanisms and applications.* Progress in Polymer Science, 2010. **35**(1-2): p. 94-112.

237. Zhang, J., et al., *Hydrophilic modification of ordered mesoporous carbons for supercapacitor via electrochemically induced surface-initiated atom-transfer radical polymerization.* Electrochemistry Communications, 2017. **74**: p. 19-23.

238. Sun, Y., et al., *Preparation of polyacrylamide via surface-initiated electrochemical-mediated atom transfer radical polymerization (SI-eATRP) for Pb2+ sensing.* Journal of Solid State Electrochemistry, 2016. **20**(1): p. 105-113.

239. Li, B., et al., *Electrochemically induced surface‐initiated atom‐transfer radical polymerization.* Angewandte Chemie International Edition, 2012. **51**(21): p. 5092-5095.

240. Zhao, B. and W.J. Brittain, *Polymer brushes: surface-immobilized macromolecules.* Progress in Polymer Science, 2000. **25**(5): p. 677-710.

241. Mori, H. and A.H.E. Müller, *New polymeric architectures with (meth)acrylic acid segments.* Progress in Polymer Science, 2003. **28**(10): p. 1403-1439.

242. Fantin, M., et al., *Understanding the Fundamentals of Aqueous ATRP and Defining Conditions for Better Control.* Macromolecules, 2015. **48**(19): p. 6862-6875.

243. Wang, W.C., et al., *Surface initiated ATRP of acrylic acid on dopamine‐functionalized AAO membranes.* Journal of applied polymer science, 2010. **117**(1): p. 534-541.

244. Dong, R., et al., *Patterned biofunctional poly (acrylic acid) brushes on silicon surfaces.* Biomacromolecules, 2007. **8**(10): p. 3082-3092.

245. Matrab, T., et al., *Grafting densely-packed poly(n-butyl methacrylate) chains from an iron substrate by aryl diazonium surface-initiated ATRP: XPS monitoring.* Surface Science, 2007. **601**(11): p. 2357-2366.

246. Nazari Pour, S., et al., *Controlled in situ formation of polyacrylamide hydrogel on PET surface via SI-ARGET-ATRP for wound dressings.* Applied Surface Science, 2015. **349**: p. 695-704.

247. Sun, Y., et al., *Preparation of protein imprinted polymers via protein-catalyzed eATRP on 3D gold nanodendrites and their application in biosensors.* RSC Advances, 2017. **7**(45): p. 28461-28468.

248. Mühlebach, A., S.G. Gaynor, and K. Matyjaszewski, *Synthesis of Amphiphilic Block Copolymers by Atom Transfer Radical Polymerization (ATRP).* Macromolecules, 1998. **31**(18): p. 6046-6052.

249. Wei, H., et al., *Stability of polydopamine and poly (DOPA) melanin-like films on the surface of polymer membranes under strongly acidic and alkaline conditions.* Colloids and Surfaces B: Biointerfaces, 2013. **110**: p. 22-28.

250. Gorman, C.B., R.J. Petrie, and J. Genzer, *Effect of Substrate Geometry on Polymer Molecular Weight and Polydispersity during Surface-Initiated Polymerization.* Macromolecules, 2008. **41**(13): p. 4856-4865.

251. Teodorescu, M. and K. Matyjaszewski*, *Controlled polymerization of (meth) acrylamides by atom transfer radical polymerization.* Macromolecular rapid communications, 2000. **21**(4): p. 190-194.

252. Kitayama, Y. and M. Okubo, *Synthetic Route to Ultra-High Molecular Weight Polystyrene (>106) with Narrow Molecular Weight Distribution by Emulsifier-Free, Emulsion Organotellurium-Mediated Living Radical Polymerization (Emulsion TERP).* Polym. Chem., 2016. **7**.

253. Matyjaszewski, K., *Atom transfer radical polymerization: from mechanisms to applications.* Israel Journal of Chemistry, 2012. **52**(3-4): p. 206-220.

254. Mochizuki, S. and A.L. Zydney, *Dextran transport through asymmetric ultrafiltration membranes: Comparison with hydrodynamic models.* Journal of Membrane Science, 1992. **68**(1): p. 21-41.

255. Susanto, H. and M. Ulbricht, *Influence of ultrafiltration membrane characteristics on adsorptive fouling with dextrans.* Journal of Membrane Science, 2005. **266**(1): p. 132-142.

256. Nobrega, R., et al., *Transfer of dextran through ultrafiltration membranes: a study of rejection data analysed by gel permeation chromatography.* Journal of membrane science, 1989. **45**(1-2): p. 17-36.

257. Susanto, H., S. Franzka, and M. Ulbricht, *Dextran fouling of polyethersulfone ultrafiltration membranes—Causes, extent and consequences.* Journal of Membrane Science, 2007. **296**(1): p. 147-155.

258. Wu, T., et al., *Behavior of Surface-Anchored Poly(acrylic acid) Brushes with Grafting Density Gradients on Solid Substrates: 1. Experiment.* Macromolecules, 2007. **40**(24): p. 8756-8764.

259. Briscoe, B., K. Sebastian, and M. Adams, *The effect of indenter geometry on the elastic response to indentation.* Journal of Physics D: Applied Physics, 1994. **27**(6): p. 1156.

260. Lee, H., et al., *Mussel-inspired surface chemistry for multifunctional coatings.* science, 2007. **318**(5849): p. 426-430.

261. Jiang, J., et al., *Improving antifouling ability and hemocompatibility of poly (vinylidene fluoride) membranes by polydopamine-mediated ATRP.* Journal of Materials Chemistry B, 2015. **3**(39): p. 7698-7706.

262. Liu, Y., et al., *Polymer Grafting via ATRP Initiated from Macroinitiator Synthesized on Surface.* Langmuir, 2004. **20**(16): p. 6710-6718.

263. Dangayach, K. and D. Bonner, *Solvent interactions with polysulfone.* Polymer Engineering & Science, 1980. **20**(1): p. 59-64.

264. Chmielarz, P., et al., *Electrochemically mediated atom transfer radical polymerization (eATRP).* Progress in Polymer Science, 2017. **69**: p. 47-78.

265. Mabbott, G.A., *An introduction to cyclic voltammetry.* Journal of Chemical Education, 1983. **60**(9): p. 697.

266. Hu, Y., et al., *Synthesis and characterization of chitosan–poly(acrylic acid) nanoparticles.* Biomaterials, 2002. **23**(15): p. 3193-3201.

267. Kirwan, L.J., P.D. Fawell, and W. van Bronswijk, *In Situ FTIR-ATR Examination of Poly(acrylic acid) Adsorbed onto Hematite at Low pH.* Langmuir, 2003. **19**(14): p. 5802-5807.

268. Ogata, Y.H., *Characterization of porous silicon by infrared spectroscopy.* Handbook of Porous Silicon, 2014: p. 473-480.